Quantum theory of moiré excitons in atomically thin semiconductors

Joakim Hagel

Department of Physics

CHALMERS UNIVERSITY OF TECHNOLOGY

Göteborg, Sweden 2024

Quantum theory of moiré excitons in atomically thin semiconductors
Joakim Hagel

Cover illustration: Schematic illustration of electron-hole pairs trapped in a moiré potential. Figure was made using Wolfram Mathematica and Inkscape.

Quantum theory of moiré excitons in atomically thin semiconductors
Joakim Hagel
Department of Physics
Chalmers University of Technology

Abstract

In recent years, atomically thin nanomaterials have garnered significant attention for their intriguing physics and potential applications in novel technological devices. Transition metal dichalcogenides (TMDs) stand out due to the reduced screening resulting in a remarkably strong Coulomb interaction and the formation of excitons, Coulomb-bound electron-hole pairs, which dominate the material's optical properties even at room temperature. By vertically stacking two TMD layers, long-lived interlayer excitons emerge, with electrons and holes spatially separated in different layers. The introduction of another layer introduces interlayer tunneling and layer polarization. These can be finely tuned by adjusting the relative twist angle between layers, forming a moiré pattern capable of spatially trapping excitons.

This thesis aims to explore the exciton energy landscape in vertically stacked TMDs using a material-specific, quantum mechanical approach. The study delves into the various coupling mechanisms and their impact on the exciton band structure, subsequently influencing the material's optical properties. Additionally, the thesis investigates electric fields and twist angle engineering as externally accessible tuning knobs. The role of interlayer tunneling in bilayer systems is emphasized, revealing strongly layer-hybridized excitons that often dominate the material's optical spectra. Atomic reconstruction in the small twist angle regime is also examined, demonstrating its significant impact on the exciton energy landscape and exciton wave function. Finally, the twist-angle-dependent in-plane charge-separation is investigated and its relation to the inter-site hopping of the moiré exciton. In summary, this research sheds light on the physics governing moiré excitons in this promising class of atomically thin nanomaterials.

List of appended publications
This thesis contains an introductory text based on the following papers:

I **Exciton landscape in van der Waals heterostructures**
J. Hagel, S. Brem, C. Linderälv, P. Erhart, E. Malic
Phys. Rev. Research. **3**, 043217 (2021)

II **Electrical tuning of moiré excitons in MoSe$_2$ bilayers**
J. Hagel, S. Brem, E. Malic
2D Materials **10** (1), 014013 (2023)

III **Twist-angle dependent dehybridization of momentum-indirect excitons in MoSe2/MoS2 heterostructures**
N. Sokolowski, S. Palai, M. Dyksik, K. Posmyk, M. Baranowski, A. Surruente, D. Maude, F. Carrascoso, O. Cakiroglu, E. Sanchez, A. Schubert, C. Munuera, T. Taniguchi, K. Watanabe, **J. Hagel**, S. Brem, A. Castellanos-Gomez, E. Malic, P. Plochocka
2D Materials **10**, 034003 (2023)

IV **Impact of atomic reconstruction on optical spectra of twisted TMD homobilayers**
J. Hagel, S. Brem, J. A. Pineiro, E. Malic
Phys. Rev. Materials. **8**, 034001 (2024)

V **Polarization and charge-separation of moiré excitons in van der Waals heterostructures**
J. Hagel, S. Brem, E. Malic
Submitted (2024)

My contributions to the appended papers
In paper I,II,IV I developed the microscopic theory, performed the numerical calculations for the exciton landscape and optical response, analyzed the results and wrote the papers with input from my main supervisor and co-authors. In paper III I developed the microscopic theory, performed the numerical calculations, analyzed the theoretical results and wrote the theory part of the paper. In paper V I generalized the microscopic theory, performed the numerical calculations, analyzed the results and wrote the paper with input from my main supervisor and co-authors.

Publications not appended in the thesis

VI **Electrical control of hybrid exciton transport in a van der Waals heterostructure**
F. Tagarelli, E. Lopriore, D. Erkensten, R. Perea-Causin, S. Brem, **J. Hagel**, Z. Sun, G. Pasquale, K. Watanabe, T. Taniguchi, E. Malic, A. Kis
Nature Photonics **17**, 615-621 (2023)

VII **Electrically tunable dipolar interactions between layer-hybridized excitons**
D. Erkensten, S. Brem, R. Perea-Causin, **J. Hagel**, F. Tagarelli, E. Lopriore, A. Kis, E. Malic
Nanoscale **15**, 11064-11071 (2023)

VIII **Interlayer exciton polaritons in homobilayers of transition metal dichalcogenides**
J. König, J. M. Fitzgerald, **J. Hagel**, D. Erkensten, E. Malic
2D Materials **10**, 025019 (2023)

IX **Anomalous Redshift in interlayer exciton Emission with Increasing Twist Angle in WSe2/MoSe2 Heterostructures**
C. Chandrakant Palekar, **J. Hagel**, B. Rosa, S. Brem, C. Shih, I. Limame, M. von Helversen, E. Malic, S. Reitzenstein
2D Materials **11**, 025034 (2024)

X **A room-temperature moiré interlayer exciton laser**
H. Fang, Q. Lin, Y. Liu, Yi. Zhang, M. Fischer, J. Li, **J. Hagel**, S. Brem, E. Malic, N, Stenger, Z. Sun, M. Wubs, S. Xiao
arXiv preprint arXiv:2302.01266

XI **Strain fingerprinting of exciton valley character**
A. Kumar, D. Yagodkin, R. Rosati, D. J. Bock, C. Schattauer, S. Tobisch, **J. Hagel**, B. Höfer, J. N. Kirchhof, P. Hernandez Lopez, K. Burfeindt, S. Heeg, C, Gahl, F. Libisch, E. Malic, K. I. Bolotin
arXiv preprint arXiv:2312.07332 (accepted in Nature Communications)

XII **Quadrupolar Excitons in MoSe$_2$ Bilayers**
J. Jasiński, **J. Hagel**, S. Brem, T. Taniguchi, K. Watanbe, A. Surrente,
M. Baranowski, D. K. Maude, E. Malic, P. Plochocka
Submitted (2024)

XIII **Probing P- and CP-violation in dark matter interactions**
R. Catena, **J. Hagel**, C. E. Yaguna
JCAP. **05**, 016 (2021)

My contributions to the non-appended publications
In paper VI and VII I derived the theoretical model for the field-dependent
exciton energy landscape and contributed with discussion regarding exciton
hybridization. In paper VIII I contributed with discussions regarding the
hybrid exciton landscape. In paper IX I derived the theoretical model, per-
formed the numerical calculations and wrote the theory part of the paper. In
paper X I contributed with discussion regarding moiré excitons and atomic
reconstruction. In paper XI I calculated the strain response of hybrid exci-
tons in bilayers. In paper XII I derived the theoretical model, performed the
numerical calculations and wrote the theoretical part of the paper. In paper
XIII I performed the numerical analysis as part of a master thesis project
later published during the PhD program and I provided the figures for the
manuscript.

Contents

CHAPTER 1

Introduction

In 1959, Nobel laureate Richard Feynman held a lecture titled "There is plenty of room at the bottom" where it was hypothesized that one could write the entire Encyclopedia Britannica on the head of a pin. Furthermore, it was envisioned that one could construct machines that in turn could construct smaller machines, all the way down to the atomic scale [1]. The introduction of these new concepts has often been refereed to as the birth of nanotechnology [1]. For the past decades, a growing demand to make electronic devices smaller has continuously motivated further studies in nanotechnologies where it has now grown into the its very own field of research. In 2004, nearly half a century after the birth of nanotechnology, a major breakthrough in the field of nanoscience occurred when Andre Geim and Konstantin Novoselov successfully isolated, and characterized a single sheet of graphene for the first time [2]. The successful isolation and characterization of a material with a single-atom thickness rewarded both researchers with the Nobel prize in physics in 2010 [3], and the materials intriguing properties later paved the way for a new field of nanoscience called two-dimensional materials [4, 5].
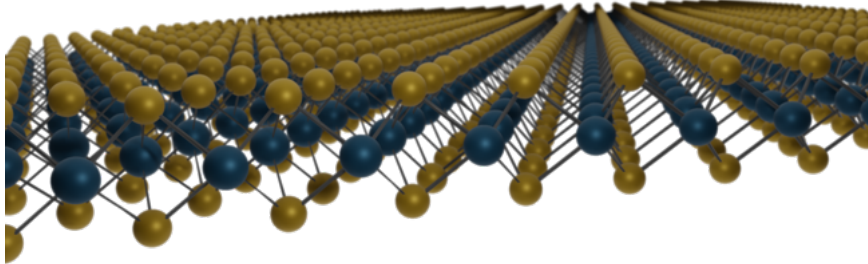
Figure 1.1: Illustration of a monolayer TMD. Larger dark blue spheres illustrates the metal atoms M and the smaller yellow spheres illustrate the chalcogen atoms X, which forms a TMD in the form MX_2. The metal atoms is usually considered to be either tungsten (W) or molybdenum (Mo) and the chalcogen atoms are usually considered to be either sulfur (S) or selenium (Se).

The emergence of two-dimensional (2D) materials revealed several new classes of atomically thin materials. One particular interesting subclass of 2D materials are the transition metal dichalcogenides (TMDs), illustrated in Figure 1.1 [6, 7]. These atomically thin semiconductors are of special interest due to their optical properties [8]. By shining a laser on the material, electrons will be excited from their resting position in the valence band up to the conduction band. By doing so, the previous occupied electron state is now instead an electron vacancy, known as a hole [7]. In a large system of electrons these holes acts as positively charged particles and can therefore strongly interact with the negatively charged electron via the Coulomb interaction. The two-dimensional nature of the material reduces the screening of this Coulomb interaction and in turn leads to a very strong attraction between electrons and holes, which allows for the formation of strongly bound electron-hole pairs, also known as excitons (see Figure 1.2.a for schematic illustration) [7]. In turn, excitons fundamentally changes the optical response of the material [9]. Consequently, understanding the physics of excitons in TMDs is key in order to understand the optical properties of the material. Other bound states such as trions [10–13] and biexcitons [14, 15] can also form. However, these lie outside the scope of this thesis.
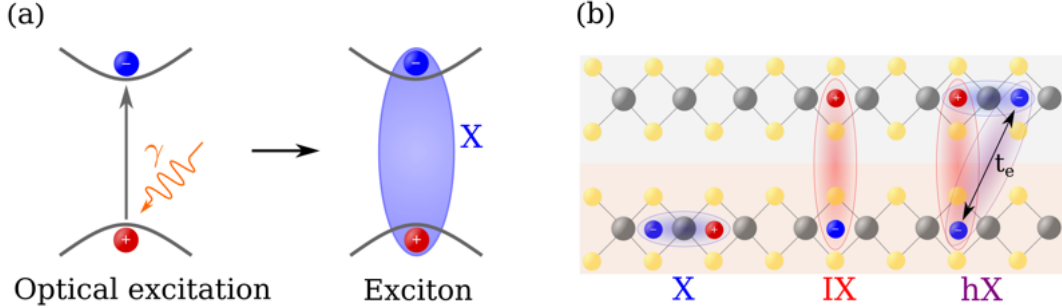
Figure 1.2: **(a)** Schematic illustration of an exciton formation. The most common optical excitation of an exciton is usually referred to as the A exciton resonance. **(b)** Schematic of different exciton species in a van der Waals heterostructure showing intralayer exciton X, interlayer exciton IX and hybrid exciton hX.

In addition to monolayer TMDs, we can also vertically stack two monolayers on top of each other to form van der Waals heterostructures [16]. Here, an electron in one layer can become strongly bound with a hole in the other layer, thus forming interlayer excitons, composed out of a spatially separated electron-hole pair as illustrated in Figure 1.2.b [17–23]. These long-lived excitons introduces a new species of excitons to study. Importantly for this work, they harbor a permanent out-of-plane dipole moment, allowing for direct external access via applied out-of-plane electric fields [24, 25]. Furthermore, the wave function of the electron or hole can have a significant overlap between the layers, allowing for efficient carrier tunneling between them. In turn, the electron or hole become strongly delocalized across the layers and consequently lead to the formation of hybrid excitons, consisting in a superposition between an intralayer exciton and an interlayer exciton (see hX in Figure 1.2.b) [26–28]. As a result, the introduction of an additional layer brings more degrees of freedom to the exciton species and fundamentally changes the exciton energy landscape. In addition to stacking TMDs vertically, it is also possible to stack them latterly, thus forming lateral heterostructures [29–32]. Furthermore, it is even possible for the formation of Janus TMD crystals where different chalcogen atoms are on the top and bottom of the crystal structure [33]. The focus of thesis however lies with vertically stacked TMDs.

Yet another degree of freedom can be introduced via the introduction of a relative twist angle between the layers. This induces another layer of peri-
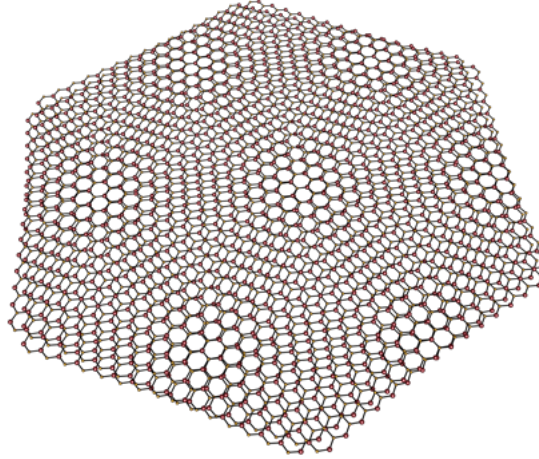
Figure 1.3: Illustration of moiré pattern with twisted TMDs.

odicity to the combined crystal structures in the form of a moiré pattern as illustrated in Figure 1.3. The varying stacking order throughout the super-lattice consequently give rise to a periodic potential within the moiré unit cell which fundamentally changes the band structure of the material. The introduction of this new degree of freedom has been shown to give rise to exotic phases in bilayer graphene such as unconventional superconductivity and Mott insulators [34]. In twisted bilayer TMDs, the moiré potential can instead trap the excitons in real space at specific high symmetry points in the superlattice and in turn give rise to a periodic arrangement of the excitons in the crystal [35–40]. Furthermore, the moiré potential has been shown to drastically impact the optical response of the material [41], resulting in multiple new peaks in optical absorption and photoluminescence measurements [42, 43]. Twist-angle-engineering has thus provided an additional way to externally tune the material properties, and it is therefore of great interest to fully study the excitonic response to the changing twist angle in order to gain a deeper insight to the prospects of tuning the optics in TMDs.

1.1 Outline

In this thesis we investigate the energy landscape of moiré excitons and its optical properties in TMD bilayer structures, where the focus lies on the interplay between the different components of the moiré potential. The thesis has been organized in the following way. We start by introducing the theoretical framework (chapter 2) used throughout this work, beginning with a brief introduction to second quantization and density matrix formalism, then continuing with the Hamiltonian representation of the many-particle processes that we are interested in and how excitons can be treated within this formalism. We also cover the modeling of optical absorption and photoluminescence here. Chapter 3 summarizes the different components of the moiré potential, including terms from both rigid and reconstructed lattices. The exciton energy landscape in bilayer TMDs, which is the result of paper I is then covered in chapter 4. Chapter 5 discusses the interplay between twist-angle-engineering and electrical field tuning, which concerns the main results from paper II. In chapter 6 we briefly cover the impact of twist-angle-dependent dehybridization and summarize the results from paper III. Furthermore, paper IV is summarized in chapter 7, discussing the impact on the optical properties from atomic reconstruction in homobilayers. Chapter 8 covers the results from paper V, where the moiré site hopping of in-plane charge-separated moiré excitons are discussed. We end with some concluding remarks and outlook in chapter 9.

1.2 Key outcomes

The thesis is partly based on the author's licentiate thesis (*Joakim Hagel, Moiré Exciton Landscape and its Optical Properties in Two-Dimensional Semiconductors (2022)* [44]) and on five papers. The key outcome of these are listed below.

Paper I In this work we investigate the exciton energy landscape in van der Waals heterostructures. We disentangle the different interlayer coupling contributions for different stackings and materials, revealing the

significant role of interlayer hybridization for the exciton band structure. We find that the exciton ground state in most materials consists of a strongly hybridized momentum-indirect exciton, which often resides far below the A exciton resonance in energy. By calculating the phonon-assisted photoluminescence spectra for each material and stacking, we map out the optical response of the exciton energy landscape in van der Waals heterostructures. The findings of this paper are summarized in chapter 4.

Paper II In this paper we study the interplay between twist-angle-engineering and electrical field tuning, and how it impacts the optical response of $MoSe_2$-$MoSe_2$ homobilayers. By including the interlayer hybridization we find that the excitons carry an effective dipole moment, depending on the degree of hybridization. Exploiting this, we then predict that one can tune the material from an indirect semi-conductor to a direct semi-conductor. Furthermore, we calculate the optical response of bright excitons in naturally stacked $MoSe_2$-$MoSe_2$, where we find that one can significantly tune the oscillator strength of the interlayer exciton via twist-angle-engineering and electrical field tuning. The findings of this paper are summarized in chapter 5.

Paper III In this joint theory-experiment collaboration, we investigate the twist-angle-dependent dehybrization of the low-lying momentum-dark excitons in $MoSe_2$-MoS_2. Here, we construct an effective model for the change in interlayer distance variation with twist angle, which can be directly associated with the tunneling strength. The local decrease in interlayer distance consequently decreases the tunneling strength significantly, in turn leading to massive blue shifts with increasing twist angle, allowing for significant tunability of the hybrid moiré exciton landscape. The findings of this paper are summarized in chapter 6.

Paper IV This work investigates the direct impact of atomic reconstruction on the optical response in twisted TMD homobilayers. We find that the strain induced potentials significantly add to the moiré potential depth. Furthermore, we identify that in naturally stacked homobilayers, the strain-induced potentials are the only significant contributions of the moiré potential for the bright A exciton resonance, accessible via optical absorption. Consequently, we predict an unambiguous optical signature

of atomic reconstruction in the optical response for naturally stacked homobilayers. The findings of this paper are summarized in chapter 7.

Paper V In this paper we study the interplay between atomic reconstruction and in-plane charge separation of moiré excitons, and its relation to the microscopic propagation. By deriving and solving a generalized two-particle Schrödringer equation for the electron and hole, we predict when the electron and hole will become separated in-plane as a function of twist angle. We find that the exciton can be divided in three different regimes, depending on the level of charge-separation. We then calculate the microscopic hopping where the charge-separated regime exhibits unexpected trapping at larger twist angles. Furthermore, we demonstrate that one can effectively tune the charge-separation and its impact on the hopping via substrate-controlled dielectric engineering. The findings of this paper are summarized in chapter 8.

CHAPTER 2

Theoretical framework

In this chapter we present the underlying theory used throughout the thesis and in the appended works. Starting with a brief introduction to the density matrix formalism and second quantization, then continuing with the many-particle Hamiltonian in TMDs. We then discuss the concept of excitons and how the Hamiltonian can be simplified by considering a transformation into exciton basis. Finally, we briefly cover the theoretical approach to both optical absorption and phonon-assisted photoluminescence.

2.1 Second quantization and density matrix formalism

Second quantization
In this work we make use of second quantization in order to model the fundamental statistical properties of the particles found in condensed matter

systems. Since the topic of second quantization can be found in most condensed matter physics textbooks, we will only briefly cover the essentials here.

In the many-particle systems we are interested in, we have a vast unknown number of identical quantum particles. This would in quantum mechanics be described by an N-particle wave function Ψ_N [45]. The construction and computation of this N-particle wave function is often too tedious or difficult to be practically feasible. In second quantization we instead capture the fundamental statistical properties with the introduction of creation $a^\dagger$ and annihilation operators a. Here, we can describe a many-particle state $|\phi_1\phi_2...\phi_N\rangle$ with the use of these operators acting upon a single state $a_1^\dagger a_2^\dagger...a_N^\dagger |0\rangle$ [45]. We can then interpret $a_i^\dagger$ as creating an additional particle in the single state $|\phi_i\rangle$. Since the annihilation operator a_i is the Hermitian adjoint of $a_i^\dagger$, this can be thought of as annihilating a particle in the single state $|\phi_i\rangle$.

The fundamental statistical properties of particles, stemming from the spin statistics theorem, is captured by two distinct particle descriptions. Either the particle has integer spin - boson - or it has half-integer spin - fermion -, where fermions obey the Pauli exclusion principle and bosons do not, i.e two fermions with the same spin can not occupy the same state. In our current framework this translates to whether the many-particle state $|\phi_1\phi_2...\phi_N\rangle$ is symmetric or anti-symmetric under Permutation (or exchange) $\widehat{\mathcal{P}}$ [45]. The many-particle state is symmetric for bosons

$$\widehat{\mathcal{P}}_{12} |\phi_1\phi_2...\phi_N\rangle = |\phi_2\phi_1...\phi_N\rangle, \tag{2.1}$$

and anti-symmetric for fermions

$$\widehat{\mathcal{P}}_{12} |\phi_1\phi_2...\phi_N\rangle = - |\phi_2\phi_1...\phi_N\rangle. \tag{2.2}$$

From this principle we can read of the essential commutators we need for a and $a^\dagger$, thus finding that bosons commute

$$[a_i^{(\dagger)}, a_j^{(\dagger)}] = a_i^{(\dagger)} a_j^{(\dagger)} - a_j^{(\dagger)} a_i^{(\dagger)} = 0, \quad [a_i, a_j^\dagger] = \delta_{ij}, \tag{2.3}$$

and fermions anti-commute

$$\{a_i^{(\dagger)}, a_j^{(\dagger)}\} = a_i^{(\dagger)} a_j^{(\dagger)} + a_j^{(\dagger)} a_i^{(\dagger)} = 0, \quad \{a_i, a_j^\dagger\} = \delta_{ij}. \tag{2.4}$$

With these simple commutation rules, the fundamental statistical properties of the many-particle state is captured, allowing us to efficiently model the different particles determining the physics in our nanomaterials.

Density matrix formalism
In combination with second quantization we use the density matrix formalism. Here, the density matrix ρ describes a statistical ensemble of many quantum states [45],

$$\rho = \sum_n p_n \left| \Psi_n \right\rangle \left\langle \Psi_n \right|, \qquad (2.5)$$

where p_n is the corresponding probability to find a particle in state $\left| \Psi_n \right\rangle$. Within this formalism we can associate the expectation value of a quantum mechanical observable $\langle \mathcal{O} \rangle$ to the trace of the density matrix [45],

$$\langle \mathcal{O} \rangle = \sum_n p_n \left\langle \Psi_n | \mathcal{O} | \Psi_n \right\rangle = \mathrm{Tr}(\rho \mathcal{O}), \qquad (2.6)$$

where $\mathrm{Tr}(\rho^2) = 1$ for pure states and $\mathrm{Tr}(\rho^2) < 1$ for mixed states. Using this definition of expectation values we can separate the temporal evolution of $\langle \mathcal{O} \rangle$ into two parts, one coherent part $\langle \mathcal{O} \rangle_{\mathrm{coh}}$ and one scattering $\langle \mathcal{O} \rangle_{\mathrm{sca}}$ part [46]. Importantly for this work, we can then recognize the coherent part as the particle occupation probability $\langle a_i^\dagger a_i \rangle$ and the scattering part as the microscopic polarization $\langle a_i^\dagger a_j \rangle$, where $i \neq j$.

2.2 Many particle Hamiltonian in TMDs

Now when the fundamental theoretical principles have been established we can set up a Hamiltonian for our interacting particles in the TMDs. For the processes covered in this work we mainly focus on three particles and their corresponding interactions; electrons, photons and phonons. Before looking closer at the various interactions that occurs, we will first establish the free kinetic part of the Hamiltonian.
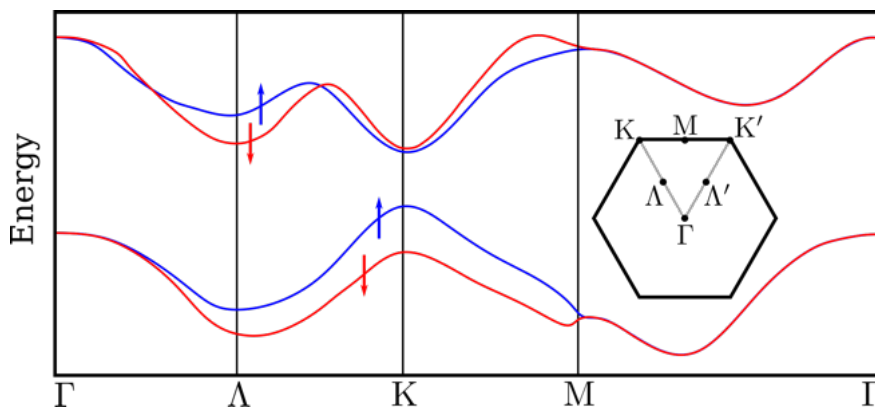
Figure 2.1: Schematic for a typical TMD band structure. The local minima for the conduction band and maxima for the valence band can be found along the high symmetry points. Arrows indicate the difference in spin configuration. The figure is adapted from Ref. [48].

Free Hamiltonian

The free Hamiltonian describing the kinetic energy for electrons or holes is in single particle picture given by

$$H_{\text{el},0} = \sum_{\boldsymbol{k}\lambda} \varepsilon_{\boldsymbol{k}}^{\lambda} \lambda_{\boldsymbol{k}}^{\dagger} \lambda_{\boldsymbol{k}}, \tag{2.7}$$

where $\lambda = (c,v)$ is describing either electrons in the conduction band c or in the valence band v, i.e v creates a hole in the valence band. Here $\boldsymbol{k}$ is the momentum in the Brillouin zone (BZ) and $\varepsilon_{\boldsymbol{k}}^{\lambda}$ is the associated kinetic energy. A schematic for a typical TMD band structure can bee seen in Fig 2.1. Here, the local conduction band minima and valence band maxima can be found around the high symmetry points in the Brillouin zone [1], which in general are the points of interest when considering excitons. Furthermore, the dispersion around these high symmetry points is well approximated by a parabolic dispersion. Thus, the electrons and holes can be considered as free particles with an effective mass.

---

[1]The Λ point is strictly speaking not a symmetry point, but rather the midpoint in a symmetry line [47]. This distinction is however not important for the purpose of this work.
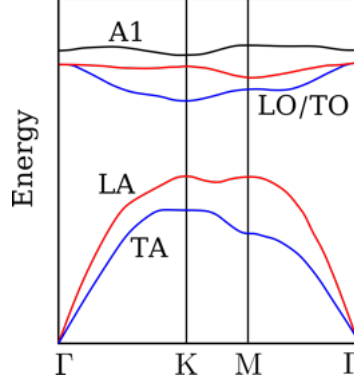
Figure 2.2: Schematic of a typical phonon band structure in TMDs with the relevant modes illustrated. A linear approximation is made for the acoustic modes close to the Γ point. In the vicinity of the remaining high symmetry points a constant approximation is made. Schematic adapted from Ref. [49].

The second part of the free Hamiltonian is given by the free phonon part

$$H_{\mathrm{ph},0} = \sum_{\boldsymbol{q}_{\mathrm{ph}}j} \hbar\Omega_{j\boldsymbol{q}_{\mathrm{ph}}} b^{\dagger}_{j\boldsymbol{q}_{\mathrm{ph}}} b_{j\boldsymbol{q}_{\mathrm{ph}}}, \qquad (2.8)$$

where $\boldsymbol{q}_{\mathrm{ph}}$ is the phonon momentum and $j = (\mathrm{TA,LA,LO,TO,A1})$ is the phonon mode index, which takes into account both the transverse (T) and longitudinal (L) part, in addition the the optical (O) branch and the acoustic (A) branch. Here, A1 is an out-of-plane optical mode. The phonon dispersion is given by $\Omega_{\boldsymbol{q}_{\mathrm{ph}}j}$, where a schematic of the relevant phonon modes in a typical TMD phonon band structure can be seen in Fig 2.2. From this figure we can see that most modes have an approximate flat dispersion around each high symmetry point, the exception being the long range acoustical modes (close to the Γ point) which can be approximated as linear. Thus we make use of the Debye approximation for long range acoustics phonons and the Einstein approximation (flat dispersion, i.e constant) for the rest.

The remaining part of the free Hamiltonian is the photon dispersion which is given by

$$H_{\mathrm{l},0} = \sum_{\boldsymbol{k}\sigma} \hbar\omega^{\sigma}_{\boldsymbol{k}} \tilde{c}^{\dagger}_{\boldsymbol{k}\sigma} \tilde{c}_{\boldsymbol{k}\sigma}, \qquad (2.9)$$

where σ is the polarization and $\hbar\omega^{\sigma}_{\boldsymbol{k}}$ is the photon energy.

Electron-electron Hamiltonian

The formation of excitons stems from the strong Coulomb interaction between electrons and holes, which in turn makes them a tightly bound electron-hole pair. The Hamiltonian governing this interaction, often referred to as the electron-electron Hamiltonian or simply the Coulomb interaction, is given by [50]

$$H_{\text{el}-\text{el}} = \frac{1}{2} \sum_{\substack{kk'q \\ \lambda\lambda'}} V_{\boldsymbol{q}} \lambda^{\dagger}_{\boldsymbol{k}+\boldsymbol{q}} \lambda'^{\dagger}_{\boldsymbol{k}'-\boldsymbol{q}} \lambda'_{\boldsymbol{k}'} \lambda_{\boldsymbol{k}}, \qquad (2.10)$$

where we now have restricted the Hamiltonian to only include intraband processes with small momentum transfers (compared to the Brillouin zone) [2]. Here, $\boldsymbol{q}$ is the transferred momentum and $V_{\boldsymbol{q}}$ is the Coulomb matrix element. When considering monolayers, the matrix element is derived from a modified form of the Rytova-Keldysh potential [51, 52], which can be obtained by solving the Poisson equation for charges in a thin film with thickness d encased in a dielectric environment. The obtained Coulomb potential then has the following expression [53]

$$V_{\boldsymbol{q}} = \frac{e^2}{2\epsilon_0 A \boldsymbol{q} \epsilon_{\text{scr}}(\boldsymbol{q})}, \qquad (2.11)$$

where A is the lattice area, e is the charge and ϵ_0 is the vacuum permittivity. The dielectric screening $\epsilon_{\text{scr}}(\boldsymbol{q})$ is given by

$$\epsilon_{\text{scr}}(\boldsymbol{q}) = \kappa_{\text{TMD}} \tanh(\frac{1}{2}[\alpha_{\text{TMD}} dq - \ln\left(\frac{\kappa_{\text{TMD}} - \kappa_{\text{sub}}}{\kappa_{\text{TMD}} + \kappa_{\text{sub}}}\right)]), \qquad (2.12)$$

where $\kappa = \sqrt{\epsilon^{\|}\epsilon^{\perp}}$ and $\alpha = \sqrt{\frac{\epsilon^{\|}}{\epsilon^{\perp}}}$. Here, $\epsilon^{\|}$ accounts for the in-plane component of the dielectric tensor and $\epsilon^{\perp}$ accounts for the out-of-plane component.

Electron-phonon Hamiltonian

An important process when describing the dynamics of excitons is their inter-

---

[2]In a more general expression, the matrix element would include form factors $F_{fi}(\boldsymbol{q}) = \langle f | e^{i\boldsymbol{q}\cdot\boldsymbol{r}} | i \rangle$, which can be approximated as $F_{fi}(\boldsymbol{q}) = \langle \boldsymbol{k}_f, \lambda_f | e^{i\boldsymbol{q}\cdot\boldsymbol{r}} | \boldsymbol{k}_i, \lambda_i \rangle \approx \delta_{\lambda_i\lambda_f} \delta_{\boldsymbol{q}, \boldsymbol{k}_f - \boldsymbol{k}_i} + i\boldsymbol{q}\cdot\boldsymbol{d}_{\lambda_f\lambda_i}$ via a Taylor expansion, where we only take into account the more dominant long-range interaction ($\boldsymbol{q} \ll \boldsymbol{G}$). Here, $\boldsymbol{d}_{\lambda_f\lambda_i} = \langle \boldsymbol{k}_f, \lambda_f | \boldsymbol{r} | \boldsymbol{k}_i, \lambda_i \rangle$ is the transition dipole matrix element. Consequently, this takes into account the long-range interaction of electron-hole exchange. Since this is small in comparison to the first term we will only consider the first term throughout this thesis.

action with phonons. For this purpose it is important to model the electron-phonon interaction, where an electron or hole can scatter with a phonon with some momentum transfer

$$H_{\text{el}-\text{ph}} = \sum_{\substack{\boldsymbol{k}\boldsymbol{q} \\ j\lambda}} G_{j\boldsymbol{q}}^{\lambda} \lambda_{\boldsymbol{k}+\boldsymbol{q}}^{\dagger} \lambda_{\boldsymbol{k}} (b_{j,-\boldsymbol{q}}^{\dagger} + b_{j,\boldsymbol{q}}), \tag{2.13}$$

where $G_{j\boldsymbol{q}}^{\lambda}$ is the electron-phonon matrix element given by [49, 50, 54],

$$G_{j\boldsymbol{q}}^{\lambda} = g_{j\boldsymbol{q}}^{\lambda} \sqrt{\frac{\hbar^2}{2\rho\mathcal{A}\hbar\Omega_{j\boldsymbol{q}}}}. \tag{2.14}$$

Here, ρ is the mass density and $\mathcal{A}$ is the area of the system. $\Omega_{j\boldsymbol{q}}$ indicate the phonon energies, which can be extrapolated from a band structure like Fig 2.2. The electron-phonon coupling is given by $g_{j\boldsymbol{q}}^{\lambda}$, which in a similar fashion as the energy is approximated as constant for all modes except for the long range acoustical modes that are approximated as linear in $\boldsymbol{q}$. The material and valley specific value of these couplings are obtained from first-principle calculations done in [49, 54].

Electron-light Hamiltonian
In this work we treat the electron-light interaction in two different approaches, depending on the process we wish to model [3]. In the case for optical excitation of an electron, we treat the electron-light interaction in the semi-classical way, i.e an electron interacting with an electromagnetic field. As long as we only consider optical absorption in the material, this is a sufficient approach. Here the electron-light Hamiltonian reads

$$H_{\text{el}-\text{l}} = -i\hbar\frac{e_0}{m_0} \sum_{\boldsymbol{k}\lambda\lambda'} \boldsymbol{M}_{\boldsymbol{k}}^{\lambda\lambda'} \cdot \boldsymbol{A}(t) \lambda_{\boldsymbol{k}}'^{\dagger} \lambda_{\boldsymbol{k}}, \tag{2.15}$$

where $\boldsymbol{M}_{\boldsymbol{k}}^{\lambda\lambda'} = \langle\lambda'\boldsymbol{k}|\nabla|\lambda\boldsymbol{k}\rangle$ is the optical matrix element, $\boldsymbol{A}(t)$ is the electromagnetic vector potential. Here e_0 and m_0 is the elementary charge and free electron mass respectively. Within the scope of this work, we are mainly interested in the interband transitions, that is $\lambda' = c$ and $\lambda = v$. This then describes the optical excitation of an electron which consequently can form an exciton.

---

[3]By placing the material in a cavity, the light-matter interaction can also lead to the formation of exciton-polaritons [55–57]. This is however outside the scope of this thesis.

If we instead want to consider the emission of light from the material this semi-classical description is not sufficient. Here, we instead have the emission of a photon after an electron has been optically excited. Since we are here dealing with the electron interacting with a single photon a more complete quantum mechanical framework is needed. For this purpose we have the electron-photon Hamiltonian which reads

$$H_{\text{el}-\text{photon}} = \sum_{\sigma \boldsymbol{q} \boldsymbol{k} \lambda \lambda'} \boldsymbol{M}_{\boldsymbol{k}\sigma}^{\lambda\lambda'} \lambda_{\boldsymbol{k}+\boldsymbol{q}\|}^{\dagger} \lambda'_{\boldsymbol{k}} \tilde{c}_{\boldsymbol{q}}^{\dagger} + h.c, \qquad (2.16)$$

where $\boldsymbol{M}_{\boldsymbol{k}\sigma}^{\lambda\lambda'}$ again is the optical matrix element and $\boldsymbol{q} \parallel$ is the momentum that is parallel to the monolayer. In this work we mainly focus on the relaxation of an electron from the conduction band to the valence band, i.e $v^{\dagger}c\tilde{c}^{\dagger}$. This is then the Hamiltonian of interest when considering a photoluminescence spectrum.

2.2.1 Equation of motion

By having complete access to the Hamiltonian that describes the system we can calculate the temporal evolution of some observable $\mathcal{O}$. This is done via Heisenberg's equation of motion [50][4].

$$i\hbar \frac{d}{dt} \langle \mathcal{O} \rangle = \left\langle [\mathcal{O}, H]_{-} \right\rangle. \qquad (2.17)$$

As mention in section 2.1 we can via the density matrix approach separate the particle occupation from the microscopic polarization and thus calculate the temporal evolution of these separately. This means when considering excitons it is sufficient to commute the polarization $\langle c^{\dagger}v \rangle$ with the Hamiltonian [5].

---

[4]This is not to be confused with the von Neuman equation. Although being similar, instead deals with the temporal evolution of the density matrix itself, not an operator.

[5]In this work we are mainly interested in the microscopic polarization, but importantly for exciton diffusion [58–60] one can also calculate the equation of motion of the particle occupation.

2.2.2 Cluster expansion approach

An often occurring problem in many-particle physics is higher order correlations and how to truncate them. If we for example want to calculate the temporal evolution for the microscopic polarization $\langle a_1^\dagger a_2 \rangle$ we will find that it couples to a two particle correlation $\langle a_i^\dagger a_j^\dagger a_k a_l \rangle$. This quantity does in turn couple to a three particle quantity which in turn couples to higher order correlations, leading to a system of differential equations which are not closed, a problem often referred to as the hierarchy problem. In order to solve this equation a scheme to factorize and truncate away the higher order correlations is needed. This can be done by expressing the N-particle quantity as single particle quantities, also known as singlets, and a higher order correction. A common cluster expansion and truncation scheme is the well known Hartree-Fock approximation [50]

$$\langle a_i^\dagger a_j^\dagger a_k a_l \rangle = \langle a_i^\dagger a_l \rangle \langle a_j^\dagger a_k \rangle - \langle a_i^\dagger a_k \rangle \langle a_j^\dagger a_l \rangle + \langle a_i^\dagger a_j^\dagger a_k a_l \rangle_{\mathrm{cor}}, \qquad (2.18)$$

where the two particle correlation has been factorized as singlets and a higher order correction. We can then neglect this higher order correction and successfully simplify the equation of motion to a single particle problem, which can be solved. This truncation is valid when considering undoped systems (same amount of electrons as holes) and if we have low exciton density. A low exciton density is determined by the criterion $n_{\mathrm{X}} \ll 1/a_{\mathrm{B}}^2$, where n_{X} is the exciton density and a_{B} is the exciton Bohr radius, which has an order of magnitude of 1 nm [61].

2.2.3 Markov approximation

The optical responses studied in this work often comes in the form of phonon-assisted photoluminescence. Here, the electron-phonon scattering is very important and in these cases the inclusion of higher order correlations will often be necessary. In these problems one will encounter the two particle correlation $S = \langle c^\dagger v b^\dagger \rangle$, which yields the following form for the equation of motion

$$\dot{S}(t) = (i\omega - \gamma)S(t) + P(t). \qquad (2.19)$$

Here, $P(t)$ is the source of the correlation S, which in the case of electron-phonon scattering would be the polarization $\langle c^\dagger v \rangle$. In order to solve this

equation we make use of the Markov approximation, where we take the standard analytical solution

$$S(t) = \int_0^\infty d\tau e^{i(\omega-\gamma)\tau} P(t-\tau), \tag{2.20}$$

and neglect the past values of $P(t)$, i.e $P(t-\tau) \approx P(t)e^{-i\omega_P\tau}$. Here P is now approximated at its current time with some temporal oscillation ω_P. With this approximation the integral can now be solved

$$S(t) = \frac{P(t)}{\gamma + i(\omega - \omega_P)}, \tag{2.21}$$

and by applying the Sokhotski–Plemelj theorem for $\gamma \to 0$ we have the following expression

$$S(t) = \pi P(t)\delta(\omega - \omega_P) - i\mathcal{P}\Big(\frac{P(t)}{\omega - \omega_P}\Big). \tag{2.22}$$

Here, the first term is usually contributing to the scattering rate, which is often the point of interest and $\mathcal{P}$ is instead the principal value which often contributes to an energy renormalization, something which can be neglected in most cases.

2.3 Excitons

In the previous section we presented the relevant Hamiltonian operators for the processes considered in this work. These Hamiltonians are, however, given in single particle picture for electrons and holes which can often become cumbersome and impractical to work with, especially when considering exciton dynamics. In order to reduce the number of operators we work with and thus the complexity, an additional framework is needed. In this section we go through how one can go from the electron-hole Hamiltonian to an exciton Hamiltonian and directly incorporate the Coulomb interaction into the free exciton part.

2.3.1 Wannier equation

An exciton becomes strongly bound due to the Coulomb interaction between electrons and holes. In order to calculate these binding energies we need to calculate the temporal evolution of the microscopic polarization $p_{\boldsymbol{k}\boldsymbol{k}'} = \langle c_{\boldsymbol{k}}^{\dagger} v_{\boldsymbol{k}'} \rangle$, which is done via Eq. 2.17. Importantly, by commuting this operator quantity with the Coulomb interaction (Eq. 2.10) and then applying the Hartree-Fock approximation (Eq. 2.18), the resulting expression is the well known semi-conductor Bloch equation [46],

$$i\hbar\dot{p}_{\boldsymbol{k}\boldsymbol{k}'} = (\varepsilon_{\boldsymbol{k}}^{v} - \varepsilon_{\boldsymbol{k}'}^{c})p_{\boldsymbol{k}\boldsymbol{k}'} + \sum_{\boldsymbol{q}} V_{\boldsymbol{q}} p_{\boldsymbol{k}+\boldsymbol{q},\boldsymbol{k}'+\boldsymbol{q}} + \tilde{\Omega}_{\boldsymbol{k}\boldsymbol{k}'}, \qquad (2.23)$$

where we have assumed a low excitation regime, i.e that the conduction band has a small occupation compared to the valence band. The first term in the equation is simply the band edge energy of the electron/hole pair and the second term takes into account the Coulomb attraction between the electron and hole. Furthermore, the last term $\tilde{\Omega}_{\boldsymbol{k}\boldsymbol{k}'} = i\hbar\frac{e_0}{m_0}\boldsymbol{M}_{\boldsymbol{k}}^{vc} \cdot \boldsymbol{A}(t)\delta_{\boldsymbol{k}\boldsymbol{k}'}$ is the Rabi frequency that accounts for optical polarization.

The above equation can be simplified by writing it in terms of center-of-mass (COM) coordinates $\boldsymbol{Q} = \boldsymbol{k}_e - \boldsymbol{k}_h$, $\boldsymbol{k} = \alpha\boldsymbol{k}_h + \beta\boldsymbol{k}_e$. Here, $\alpha = m_e/(m_e + m_h)$ and $\beta = m_h/(m_e + m_h)$. The effective masses of the electrons and holes can be approximated with a parabolic approximation around each high symmetry point from a band structure calculated with first-principle calculations (such as Fig 2.1) [48]. Eq. 2.23 then reads

$$i\hbar\dot{p}_{\boldsymbol{Q}\boldsymbol{k}} = -\varepsilon_{\boldsymbol{Q}\boldsymbol{k}} p_{\boldsymbol{Q}\boldsymbol{k}} + \sum_{\boldsymbol{q}} V_{\boldsymbol{q}} p_{\boldsymbol{Q},\boldsymbol{k}+\boldsymbol{q}} + \tilde{\Omega}_{\boldsymbol{0}}, \qquad (2.24)$$

where $\tilde{\Omega}_{\boldsymbol{0}}$ is constrained to $\boldsymbol{Q} = \boldsymbol{0}$ from the momentum selection rules and $\varepsilon_{\boldsymbol{Q}\boldsymbol{k}}$ is the kinetic energy of the electron(hole) which is given by

$$\varepsilon_{\boldsymbol{Q}\boldsymbol{k}} = E_{\text{gap}} + \frac{\hbar^2 \boldsymbol{Q}^2}{2M} + \frac{\hbar^2 \boldsymbol{k}^2}{2m_{\text{red}}}. \qquad (2.25)$$

Here the center-of-mass momentum $\boldsymbol{Q}$ is shifted by some valley coordinate $\boldsymbol{\xi} = (\xi_e, \xi_h)$ (i.e $\boldsymbol{Q}$ gives the momentum in relation to the valley momentum coordinates $\boldsymbol{\xi}_e - \boldsymbol{\xi}_h$, which means that $\boldsymbol{Q} = \boldsymbol{0}$ only describes a momentum

direct transition if $\xi_e = \xi_h$) and E_{gap} denotes the band gap energy. Furthermore, $M = m_e + m_h$ is the total mass and $m_{\text{red}} = m_e m_h/(m_e + m_h)$ is the reduced mass. We now introduce the basis change $p_{\boldsymbol{Q}\boldsymbol{k}} = \sum_\mu P_{\boldsymbol{Q}}^\mu \Psi^\mu(\boldsymbol{k})$, where μ is exciton quantum number (throughout this thesis when working with bilayers this is restricted to 1s) and $\Psi^\mu(\boldsymbol{k})$ is a complete set of orthogonal eigenvectors that satisfy the following eigenvalue problem

$$\frac{\hbar^2 \boldsymbol{k}^2}{2m_{\text{red}}} \Psi_{\boldsymbol{\xi}}^\mu(\boldsymbol{k}) - \sum_{\boldsymbol{q}} V_{\boldsymbol{q}} \Psi_{\boldsymbol{\xi}}^\mu(\boldsymbol{k} + \boldsymbol{q}) = E_{\boldsymbol{\xi}}^\mu \Psi_{\boldsymbol{\xi}}^\mu(\boldsymbol{k}). \tag{2.26}$$

Here, the eigenvalue problem has been written specifying the valley $\boldsymbol{\xi} = (\xi_e, \xi_h)$, where $\xi_{e(h)}$ denotes which valley the electron (hole) is sitting in. Consequently, we can drop the dependence on $\boldsymbol{Q}$. This equation is then similar to the Schrödinger equation and solves for the exciton bindings energies $E_{\boldsymbol{\xi}}^\mu$ and exciton wave functions $\Psi_{\boldsymbol{\xi}}^\mu(\boldsymbol{k})$.

By solving Eq. 2.26, which is known as the Wannier equation, we can then gain access to the exciton binding energies for a specific valley configuration. Most commonly we think of the electron and hole sitting around the same high symmetry point in the band structure. i.e the center-of-mass momentum $\boldsymbol{Q} = \boldsymbol{0}$ ($\xi_e = \xi_h$), but we can also have momentum indirect excitons ($\xi_e \neq \xi_h$), known as dark excitons (in contrast, an exciton where the electron and hole sits in the same valley is called bright) (cf. Fig 2.3) [62–64]. Here, the electron and hole are separated by some momentum in the Brillouin zone and can thus not be optically excited. As we will see later in this work however, these excitons will become very important when describing other optical features, especially in bilayers, thus it is important to take them into consideration.

Applying this basis change into Eq. 2.24 we then have the semi-conductor Bloch equation in exciton basis

$$i\hbar \dot{P}_{\boldsymbol{Q}}^\mu = -E_{\boldsymbol{Q}}^\mu P_{\boldsymbol{Q}}^\mu - \Omega_{\boldsymbol{0}}^\mu, \tag{2.27}$$

where

$$E_{\boldsymbol{Q}}^\mu = E_{\text{gap}} + \frac{\hbar^2 \boldsymbol{Q}^2}{2M} + E_{\boldsymbol{\xi}}^\mu, \quad \Omega_{\boldsymbol{0}}^\mu = \frac{e_0}{m_0} \sum_{\boldsymbol{k}} \Psi_{\boldsymbol{\xi}}^\mu(\boldsymbol{k})^* \boldsymbol{M}_{\boldsymbol{k}}^{vc} \cdot \boldsymbol{A}(t). \tag{2.28}$$
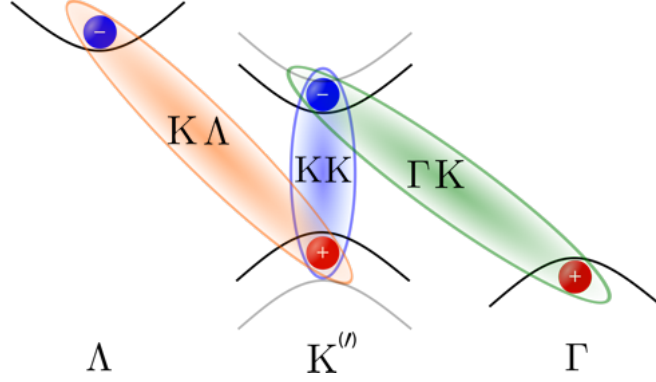
Figure 2.3: Schematic for different exciton valley configurations. Here we can see the bright KK exciton and the momentum dark KΛ/ΓK exciton. The shaded lines at the K indicate the K′ valley, which instead can form the spin-dark exciton KK′.

The solution to this equation can then be found by Fourier transforming the equation into frequency space, which then reads

$$P_{\boldsymbol{Q}}^{\mu}(\omega) = \frac{\Omega_{\boldsymbol{0}}^{\mu}(\omega)}{\hbar\omega - E_{\boldsymbol{0}}^{\mu} - i\gamma}, \tag{2.29}$$

where we have introduced the phenomenological damping γ.

2.3.2 Exciton basis

In the previous section we showed that one can transform the semi-conductor Bloch equation into exciton basis and thus incorporate the Coulomb interaction by solving the Wannier equation (Eq. 2.26). A similar approach is possible to apply directly to the Hamiltonian [65], thus further simplifying future calculations. First, we apply something called the pair operator expansion

$$P_{ij}^{\dagger} = c_i^{\dagger} v_j. \tag{2.30}$$

Here, $i(j)$ is a generic compound index. The commutator of this operator then reads

$$[P_{ij}, P_{kl}^{\dagger}] = \delta_{ik}^{jl} - \mathcal{O}_{\text{corr}}, \tag{2.31}$$

where $\mathcal{O}_{\text{corr}} = v_l^{\dagger} v_j \delta_{ik} + c_k^{\dagger} c_i \delta_{jl}$ is a correction term that accounts for the fact that excitons are composite quasiparticles from fermions. Since this
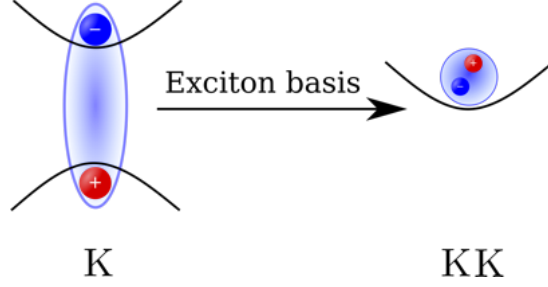
Figure 2.4: Schematic of transformation into exciton basis.

correction scales with the occupation, we can at low density approximate an exciton as a fully bosonic particle, i.e

$$[P_{ij}, P_{kl}^\dagger] \approx \delta_{ik}^{jl}. \tag{2.32}$$

This also translates into intraband transitions which would transform as

$$c_i^\dagger c_j \approx \sum_m P_{im}^\dagger P_{jm}$$
$$v_i^\dagger v_j \approx \delta_{ij} - \sum_m P_{mj}^\dagger P_{mi}. \tag{2.33}$$

The next step is to turn these pair operators into exciton operators. This is done in similar manner as in the previous section where we expand with the exciton wave functions

$$P_{\boldsymbol{k}\boldsymbol{k}'}^\dagger = \sum_\mu X_{\mu, \boldsymbol{k}-\boldsymbol{k}'}^\dagger \Psi^\mu(\alpha\boldsymbol{k}' + \beta\boldsymbol{k}), \tag{2.34}$$

where $X^\dagger$ is the exciton creation operator and $\Psi^\mu(\boldsymbol{k})$ are the exciton wave functions. Here, μ is compound index taking into account both valley and exciton quantum number. With this transformation we can write a diagonal form of the free electronic Hamiltonian and the Coulomb interaction

$$H_{\text{el},0} + H_{\text{el}-\text{el}} \to H_0 = \sum_{\boldsymbol{Q}\mu} E_{\boldsymbol{Q}}^\mu X_{\mu\boldsymbol{Q}}^\dagger X_{\mu\boldsymbol{Q}}. \tag{2.35}$$

By solving the Wannier equation to obtain $E_{\boldsymbol{Q}}^\mu$ (Eq. 2.26) we can then turn a problem involving the interaction between two particles into a free one particle Hamiltonian as illustrated in Fig 2.4. This transformation can then be applied to all other Hamiltonians and thus moving the entire framework to exciton basis instead.

2.4   Optical response

Now when the theoretical framework for calculating the exciton energies has been established, we want to investigate how to model the optical observables. In this part we breifly go through the approach for both optical absorption and phonon-assisted photoluminescence.

2.4.1   Absorption spectra

In order to gain access to the optical response of the material we study the linear response from an electric field $\boldsymbol{E}$

$$P(\omega) = \epsilon_0 \chi(\omega) E(\omega), \tag{2.36}$$

where $P(\omega)$ is the polarization induced from the electric field and $\chi(\omega)$ is the optical susceptibility. This equation can then be rewritten

$$\chi(\omega) = \frac{j(\omega)}{\varepsilon \omega^2 A(\omega)}. \tag{2.37}$$

Here, the relationship between the electric field and the vector potential is used $E = \dot{A}(\omega)$, in combination with the relation between the polarization and the macroscopic current $j(\omega) = \dot{P}(\omega)$.

In order to connect this macroscopic response to our microscopic model we can for this purpose interpret j is the probability current, which in second quantization reads

$$j(t) = \frac{e_0 \hbar}{A m_0} \sum_{\boldsymbol{k}} \mathrm{Im}\{M_{\boldsymbol{k}} p_{\boldsymbol{k}\boldsymbol{k}}\}, \tag{2.38}$$

where we now have neglected the intraband current due to its limiting impact in the sub-THZ regime. Here, we also only focus on the imaginary part since this describes the optical absorption. We can now combine the expression together with the solution to the Bloch equation in exciton basis (Eq. 2.29) and plug the results into Eq. 2.37 to get the formula for optical absorption

$$\alpha(\omega) \propto \frac{1}{\omega} \sum_{\mu} \frac{|M^{\mu}|^2}{(\hbar\omega - E_{\boldsymbol{0}}^{\mu})^2 + \gamma^2}. \tag{2.39}$$

This equation which is known as the Elliot formula can then be used to calculate the optical response of the material taking into account the exciton features of said material [66].

2.4.2 Phonon-assisted photoluminescence

In 2.2 it was shown that excitons could both be direct and indirect in momentum space, i.e center-of-mass is either in or outside the light cone. If the latter is the case, the exciton can not directly recombine with a photon. Instead, the optical observable comes in the form of phonon-assisted photoluminescence (PL) [67, 68]. That is, the exciton scatters to a virtual state within the light cone and then emits a photon. This higher order process can be microscopically modeled by taking the temporal evolution of the photon density $n_{\boldsymbol{k}} = \langle \tilde{c}_{\boldsymbol{k}}^{\dagger} \tilde{c}_{\boldsymbol{k}} \rangle$.

Following the approach laid out in Ref.[68] one can find the coupled differential equations for the photon density, the polarization $\mathcal{S}_{\boldsymbol{k}}^{\mu} = \langle \tilde{c}_{\boldsymbol{k}}^{\dagger} X_{\mu\boldsymbol{k}} \rangle$, the phonon-assisted polarization $\mathcal{U}_{\boldsymbol{kq}}^{\mu,\pm} = \langle \tilde{c}_{\boldsymbol{k}}^{\dagger} b_{\pm\boldsymbol{q}}^{(\dagger)} X_{\mu-\boldsymbol{q}} \rangle$, the exciton phonon correlation $\mathcal{C}_{\boldsymbol{Qq}}^{\mu,\pm} = \langle X_{\mu\boldsymbol{Q}}^{\dagger} X_{\mu\boldsymbol{Q}-\boldsymbol{q}} b_{\pm\boldsymbol{q}}^{(\dagger)} \rangle$ and the exciton density $N_{\boldsymbol{Q}}^{\mu} = \langle X_{\mu\boldsymbol{Q}}^{\dagger} X_{\mu\boldsymbol{Q}} \rangle$. By factorizing with the cluster-expansion scheme and then truncating higher order correlations with the Born-Markov approximation one can derive the formula for phonon-assisted PL $I_{\sigma}(\omega) \propto \frac{d}{dt} n_{\boldsymbol{k}}$ [68]

$$I_{\sigma}(\omega) \propto \sum_{\mu\xi} \frac{|M_{\sigma}^{\xi\mu}|^2}{(\mathcal{E}_{\mu 0}^{\xi} - \hbar\omega)^2 + (\gamma_{\mu}^{\xi} + \Gamma_{\mu}^{\xi'})^2} \Big(\gamma_{\mu}^{\xi} N_{\mu 0}^{\xi} + \sum_{\substack{\xi'\mu' \\ \boldsymbol{q}j\pm}} |D_{\xi\mu j\boldsymbol{0}}^{\xi'\mu'\boldsymbol{q}}|^2 N_{\mu'\boldsymbol{q}}^{\xi'} \tilde{n}_{\boldsymbol{q}j}^{\pm} L(\mathcal{E}_{\mu'\boldsymbol{q}}^{\xi'} \pm \Omega_{\boldsymbol{q}j} - \hbar\omega, \Gamma_{\mu'}^{\xi'}) \Big),$$

(2.40)

where $\mu(\mu')$ is the exciton quantum number, σ the polarization of the photon, $\xi(\xi')$ the valley index, $\boldsymbol{q}$ the involved phonon momentum, j the phonon mode index and $\pm$ denotes phonon absorption $(+)$ and emission $(-)$. The first part of the equation describes the direct recombination of bright excitons within the light cone. Here, $M_{\sigma}^{\xi\mu}$ is the exciton-photon matrix element determining the oscillator strength of the excitons. Furthermore, $\mathcal{E}_{\mu\boldsymbol{Q}}^{\xi}$ is the exciton energy as calculated by the Wannier equation (Eq. 2.26) and L is a Cauchy–Lorentz

distribution. The radiative and non-radiative broadening are described by γ_μ^ξ and $\Gamma_\mu^{\xi'}$, respectively. Throughout this thesis we mostly focus on the spectral position of the peaks, thus we account for these phenomenologically [43, 69]. At low exciton densities, the exciton occupation can be approximated according to the Boltzmann distribution $N_{\mu q}^\xi$. Furthermore, Ω_{qj} denotes the phonon energy and $\tilde{n}_{qj}^\pm = 1/2 \mp 1/2 + n_B(\Omega_{qj})$ the phonon occupation, which is given by the Bose-Einstein distribution $n_B(\Omega_{qj})$.

The exciton-phonon matrix element $D_{\xi\eta j\mathbf{0}}^{\xi'\mu'\mathbf{q}}$ is given by

$$D_{\xi\mu j\mathbf{0}}^{\xi'\mu'\mathbf{q}} = \mathcal{G}_{\xi,\xi'}^{cj}(\mathbf{q} - \Delta\boldsymbol{\xi})\delta_{\xi_h\xi_h'} - \mathcal{G}_{\xi,\xi'}^{vj}(\mathbf{q} - \Delta\boldsymbol{\xi})\delta_{\xi_e\xi_e'}, \qquad (2.41)$$

where $\Delta\boldsymbol{\xi} = (\xi_e' - \xi_h' - \xi_e + \xi_h)$ is the transferred valley momentum which ensures the correct transformation between the globally defined phonon momentum and the exciton/electron momenta defined in valley local coordinates. Here, $\mathcal{G}_{\xi,\xi'}^{c(v)vj}(\mathbf{q})$ is given by

$$
\begin{aligned}
\mathcal{G}_{\xi,\xi'}^{cj}(\mathbf{q}) &= G_{\xi_e\xi_e'}^{cj}(\mathbf{q})\mathcal{F}^{\xi\xi'}(\beta^{\xi\xi'}\mathbf{q}) \\
\mathcal{G}_{\xi,\xi'}^{vj}(\mathbf{q}) &= G_{\xi_h\xi_h'}^{vj}(\mathbf{q})\mathcal{F}^{\xi\xi'}(-\alpha^{\xi\xi'}\mathbf{q}),
\end{aligned}
\qquad (2.42)
$$

where $G_{\xi_\lambda\xi_\lambda'}^{\lambda j}$ is the carrier-phonon matrix element as shown in Eq. 2.14 (note that we have also included the specific valley index ξ here). Finally, the exciton form factors $\mathcal{F}^{\xi\xi'}(\mathbf{q})$ are given by

$$\mathcal{F}^{\xi\xi'}(\mathbf{q}) = \sum_{\mathbf{k}} \Psi_\xi^*(\mathbf{k})\Psi_\xi'(\mathbf{k} + \mathbf{q}). \qquad (2.43)$$

Here, $\Psi_\xi(\mathbf{k})$ are the exciton wave functions as obtained from the Wannier equation (Eq. 2.26).

CHAPTER 3

Moiré potential

At the core of this thesis lies the different couplings that emerges between two monolayers when vertically stacking them on top of each other, and how they are impacted by a change in relative twist angle. In this chapter we will go through the different interlayer couplings, how they are derived and how they evolve with twist angle. However, first we will generalize the theoretical framework laid out in section 2.3 to also include interlayer excitons, i.e an exciton where the electron and hole are spatially separated between the layers.

3.1   Interlayer excitons

So far we have only dealt with excitons in a monolayer, where the electron and hole always sit in the same layer. If we now instead consider a bilayer system, the electron and hole can become spatially separated by residing in different layers. For this purpose we will introduce an additional index to

the carrier operators, namely the layer index $l = (0,1)$, where $l = 0$ denotes the bottom layer and $l = 1$ denotes the top layer. Carrying the layer index with us through the same derivation done in subsection 2.3.1, it will act as an additional quantum index (similar to the valley index in Eq. 2.26) for the exciton state and we can consequently generalize the Wannier equation to include interlayer excitons as well

$$\frac{\hbar^2 \boldsymbol{k}^2}{2m_{L,\text{red}}}\Psi^\mu_{L,\boldsymbol{\xi}}(\boldsymbol{k}) - \sum_{\boldsymbol{q}} V_{L,\boldsymbol{q}}\Psi^\mu_{L,\boldsymbol{\xi}}(\boldsymbol{k}+\boldsymbol{q}) = E^\mu_{L,\boldsymbol{\xi}}\Psi^\mu_{L,\boldsymbol{\xi}}(\boldsymbol{k}), \tag{3.1}$$

where $L = (l_e, l_h)$ is a compound layer index taking into account the layer positioning of both the hole and electron. In turn, for each unique set of valley configuration $\boldsymbol{\xi} = (\xi_e, \xi_h)$ we have four unique excitons in terms of layer configuration. Two excitons where the electron and hole sits in the same layer ($L = (0,0)$ and $L = (1,1)$), known as intralayer excitons, also two excitons where the electron and hole sits in different layers ($L = (0,1)$ and $L = (1,0)$), which constitutes the interlayer excitons [17, 19, 24, 70–74].

Important for the exciton energies, the Coulomb matrix element now also carries the layer index

$$V_{L,\boldsymbol{q}} = \frac{e^2}{2\epsilon_0 A q \epsilon^{l_e l_h}_{\text{scr}}(\boldsymbol{q})}, \tag{3.2}$$

where the screening $\epsilon^{l_e l_h}_{\text{scr}}(\boldsymbol{q})$ is now dependent on the layer configuration. Consequently, we have to adjust the screening when solving the generalized Wannier equation. This general Keldysh screening can be derived from the Poisson equation by solving for the boundary conditions of two dielectric slabs [75, 76]. This was done in Ref. [76] and reads

$$\epsilon^{ll'}_{\text{scr}}(\boldsymbol{q}) = \begin{cases} \epsilon_{\text{inter}}(\boldsymbol{q}), & l \neq l' \\ \epsilon^l_{\text{intra}}(\boldsymbol{q}), & l = l' \end{cases},$$

$$\epsilon_{\text{inter}}(\boldsymbol{q}) = \kappa_{\text{sub}}g^0_{\boldsymbol{q}}g^1_{\boldsymbol{q}}f_{\boldsymbol{q}}, \quad \epsilon^l_{\text{intra}}(\boldsymbol{q}) = \frac{\kappa_{\text{sub}}g^{1-l}_{\boldsymbol{q}}f_{\boldsymbol{q}}}{\cosh(\delta_{1-l}\boldsymbol{q}/2)h^l_{\boldsymbol{q}}}. \tag{3.3}$$

28

Here, we use the abbreviations

$$
\begin{aligned}
f_{\boldsymbol{q}} &= 1 + \frac{1}{2}\Big[(\frac{\kappa_0}{\kappa_{\text{sub}}} + \frac{\kappa_{\text{sub}}}{\kappa_0})\tanh(\delta_0\boldsymbol{q}) + (\frac{\kappa_1}{\kappa_{\text{sub}}} + \frac{\kappa_{\text{sub}}}{\kappa_1})\tanh(\delta_1\boldsymbol{q}) \\
&\quad + (\frac{\kappa_0}{\kappa_1} + \frac{\kappa_1}{\kappa_0})\tanh(d_0\boldsymbol{q})\tanh(\delta_1\boldsymbol{q})\Big], \\
h_{\boldsymbol{q}}^l &= 1 + \frac{\kappa_{\text{sub}}}{\kappa_l}\tanh(\delta_l\boldsymbol{q}) + \frac{\kappa_{\text{sub}}}{\kappa_{1-l}}\tanh(\delta_{1-l}\boldsymbol{q}/2) \\
&\quad + \frac{\kappa_l}{\kappa_{1-l}}\tanh(\delta_l\boldsymbol{q})\tanh(\delta_{1-l}\boldsymbol{q}/2), \\
g_{\boldsymbol{q}}^l &= \frac{\cosh(\delta_l\boldsymbol{q})}{\cosh(\delta_{1-l}\boldsymbol{q}/2)[1 + \frac{\kappa_{\text{sub}}}{\kappa_l}\tanh(\delta_l\boldsymbol{q}/2)]},
\end{aligned} \tag{3.4}
$$

where κ_{sub} is the dielectric components of the substrate as the defined in Eq. 2.12 and κ_l is instead for the TMD layer l. Here, $\delta_l = \alpha_l d_l$, where d_l is the layer thickness of the TMD and α_l also is defined in Eq. 2.12. The dielectric components and the layer thicknesses are obtained from Ref. [77, 78]. The decoupled bilayer exciton energies then reads

$$
E_{L,\boldsymbol{Q}}^{\mu\boldsymbol{\xi}} = E_{L,\text{gap}} + \frac{\hbar^2\boldsymbol{Q}^2}{2M_L} + E_{L,\boldsymbol{\xi}}^{\mu}. \tag{3.5}
$$

Here, $E_{L,\boldsymbol{\xi}}^{\mu}$ are the energies obtained from the generalized Wannier equation.

3.2 Polarization-induced alignment shift

The first interlayer coupling to be covered is the polarization-induced alignment shift, or simply alignment shift. This component of the moiré potential acts as band edge renormalization due to a charge-transfer induced polarization between the layers, which depends on the local atomic alignment (hence shortened as alignment shift) [79]. In order to understand this potential it is then natural to start with an untwisted structure and study the impact this potential has on different stacking configurations.

Bilayer TMDs are usually divided up into two distinctly different stackings; R-type stacking and H-type stacking. Both of these stacking in turn hosts three distinctly different high symmetry stackings as can be seen in Fig 3.1.
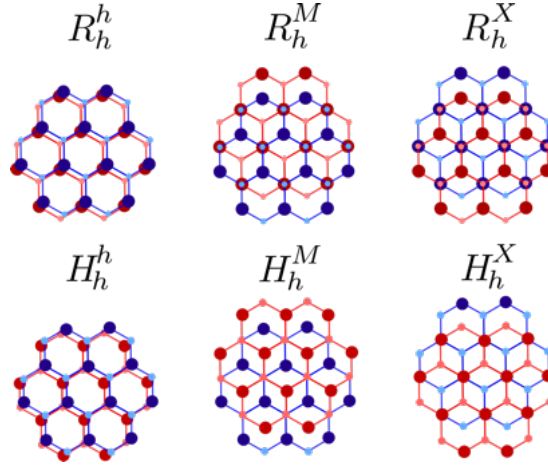
Figure 3.1: Schematic for the different high symmetry stackings found in bilayer TMDs.

Here we have R_h^h, where the metal atoms of layer 1 is on top the metal atoms of layer 2, and the chalcogen atoms of layer 1 is on top of chalcogen atoms of layer 2. From this position the layers can be shifted with respect to each other such that the metal atom of layer one sits on top of the hole of layer 2 (i.e empty space between atoms) and the metal atoms of layer 2 sits on top of the chalcogen atoms of layer 1. This would then constitute the R_h^M-stacking. Shifting the layers in the opposite direction gives the inverse of the configuration and thus constitutes R_h^X, i.e chalcogen atoms of layer 1 sits on top of hole in layer 2 and metal atoms of layer 1 sits on top of the chalcogen atoms of layer 2. Note that in a homobilayer (both layers being the same material), R_h^M and R_h^X are identical and can not be differentiated.

In H-type (cf. Fig 3.1), we instead start from a different position. Here, one of the layers are rotated with 180° with respect to the other such that metal atoms of layer 1 is on top of chalcogen atoms of layer 2, and metal atoms of layer 2 are on top of chalcogen atoms of layer 1. This high symmetry stacking then constitutes H_h^h, but is also commonly referred to as naturally stacked TMDs due to it being to most energy efficient stacking [80]. Again shifting the layers with respect to each other leads to the two other high symmetry stackings, which are known as H_h^X and H_h^M.

The induced band edge renormalization can then be computed for each high symmetry stacking described above via *ab inito* calculations, where the ma-

30

trix element governing this shift is given by [73]

$$\Delta\varepsilon_l^{\alpha\mathbf{k}} = \int d\mathbf{r}\, n_{l,\alpha\mathbf{k}}(\mathbf{r})\delta V_{\text{pol}}(\mathbf{r}).\qquad(3.6)$$

where $n_{l,\alpha\mathbf{k}}$ is the orbital density of state $|\alpha\mathbf{k}\rangle$ of monolayer l. Here, $\alpha = (\lambda,\xi)$ is a compound index, where $\lambda = (c,v)$ is the band index and ξ is the valley index. Furthermore, δV_{pol} is the solution to the Poisson equation for the electron density difference δn ($\nabla^2 \delta V_{\text{pol}} - \delta n = 0$) with $\delta n = n_{1,2} - n_1 - n_2$, with the subscript indicating which monolayer and $n_{1,2}$ being the bilayer. The material specific values of these induced shifts were computed with density functional theory by Christopher Linderälv in paper I.

In future uses of this potential we can drop the valley index from Eq. 3.6 since the induced shifts are a rigid shift of the entire band structure. Furthermore, since microscopic origin of these shifts stem from a spontaneous charge-transfer-induced polarization between the layers, it requires that the material system lacks inversion symmetry [79], i.e it must be more energetically favorable for the electrons to sit in one layer rather than the other in order to induce a polarization between the layers. As a consequence, a homobilayer with H-type stacking will not exhibit this potential at all since it is inversion symmetric [1].

After calculating the alignment shift for each high symmetry stacking we can investigate how it would manifest with the introduction of a marginal twist angle between the layers. When introducing a twist angle, each of the three high symmetry stackings will be present (R_h^h, R_h^M, R_h^X if twisted from $0°$ and H_h^h, H_h^X, H_h^M if twisted from $60°$) throughout the superlattice with varying local stacking alignment between them, thus inducing a C_3 symmetric moiré pattern as shown in Fig 3.1. Considering only small twist angles, we can treat this variation in the local stacking alignment as continuous and consequently map the alignment shift as a smooth periodic function [42]. Assuming this form of the alignment shift allows us to interpolate between the calculated values for each high symmetry stacking, thus obtaining the full twist-angle-

---

[1]In H-type stacked heterostructures, this potential is also heavily suppressed due to the only thing breaking the inversion symmetry is the small differences between the materials and not the stacking configuration itself [73].
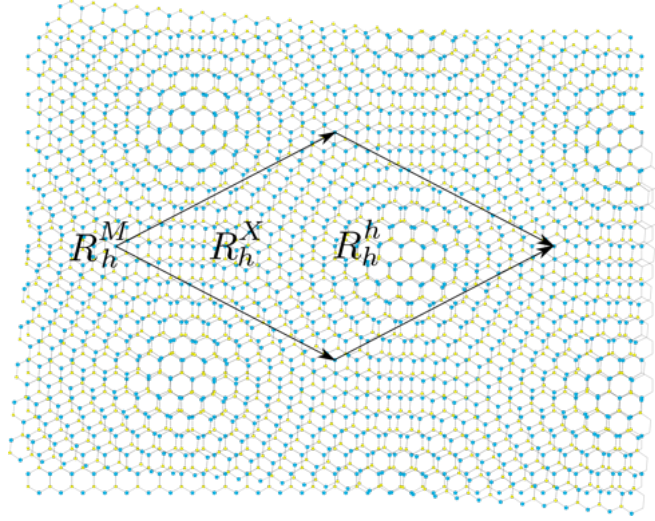
Figure 3.2: Schematic of a twisted bilayer TMD superlattice.

dependent alignment shift which is given by

$$U_{nn}^\lambda(\boldsymbol{r}) = \mathrm{Re}\left[v_n^\lambda + (\mathcal{A}_n^\lambda + \mathcal{B}_n^\lambda e^{i2\pi/3}) \sum_{h=0}^{2} e^{i\boldsymbol{g}_h \cdot \boldsymbol{r}}\right]. \tag{3.7}$$

Here, $\boldsymbol{g}_0 = \boldsymbol{G}_1 - \boldsymbol{G}_2$ is the first shell reciprocal moiré lattice vector defined as the difference between the reciprocal vector of layer 1 and layer 2, where $\boldsymbol{g}_0/\boldsymbol{g}_1/\boldsymbol{g}_2$ are connected via the 120° rotation operator C_3 as $C_3\boldsymbol{g}_0 = \boldsymbol{g}_1$ ($C_3\boldsymbol{g}_1 = \boldsymbol{g}_2$). The real space coordinate of the moiré is denoted by $\boldsymbol{r}$, which is periodic with moiré lattice vectors $\boldsymbol{a}_M$. Moreover, v_l^λ, $\mathcal{A}_l^\lambda$ and $\mathcal{B}_l^\lambda$ are the parameters obtained through the interpolation process and $U_{nn}^\lambda(\boldsymbol{r})$ is the real space representation of the spatially periodic alignment shift. Finally, n is here a generic index also containing the layer index l. With access to the full twist-angle-dependent alignment shift we can now set it up as a Hamiltonian so it can be incorporated into our theoretical frame work for excitons down the line

$$H_U = \sum_{n\lambda\boldsymbol{r}} U_{nn}^\lambda(\boldsymbol{r})\Psi_n^{\lambda\dagger}(\boldsymbol{r})\Psi_n^\lambda(\boldsymbol{r}), \tag{3.8}$$

where $\Psi_n^{(\dagger)\lambda}(\boldsymbol{r})$ are the real space annihilation (creation) operators for the conduction/valence band.

3.3 Interlayer tunneling

The second component to the moiré potential is the interlayer tunneling of charge carriers [26, 27, 43, 73, 81, 82]. In bilayer TMDs, the wave function overlap between the layers leads to efficient tunneling between the layers for the electrons and holes, which in turn forms a layer-hybridized state, where the electron/hole is delocalized across the layers. Consequently, an intralayer exciton can mix with an interlayer exciton and lead to a layer-hybridized exciton state, which would be in a superposition between these two states $\mathcal{C}_{00} \ket{l = 0, l' = 0} + \mathcal{C}_{01} \ket{l = 0, l' = 1}$, where $\mathcal{C}$ is the relative mixing between these states. The exciton hybridization will in turn also impact the final exciton energy, which means if the tunneling strength itself is periodic in the twist-angle-induced superlattice, we have a periodic modification to the exciton energies and thus another component to the moiré potential.

In order to model the tunneling correctly and then map it to the superlattice we will take a similar approach as in section 3.2, and calculate the tunneling strength for each high symmetry point and then interpolate between them. In contrast to the alignment shift, the tunneling strength is very much dependent on the orbital composition of the local valley [28, 83], which in turn means that we need to calculate the tunneling strength for each valley as well.

First we will consider the tunneling around the K (K$'$) point in the Brillouin zone. Here, at the edges of the BZ, a special case emerges due to the angular symmetry of the d-orbitals that it is mostly composed out of [28, 83]. Approximating that the only contribution to the orbitals around the K-point stems from these d-orbitals around the metal atom (d-orbital contribution is $\sim 80\%$), one can exploit this in a tight binding framework and model the tunneling as [28, 43]

$$T_{ll'}^{\lambda}(S) = \sum_{n=0}^{2} t_{ll'}^{\lambda}(S) \, e^{i\tau(\mathrm{C}_3^{(n)} \boldsymbol{K} - \boldsymbol{K}) \cdot \boldsymbol{D}(S)} \phi_{l'}(S), \qquad (3.9)$$

where we now have exploited the C$_3$ symmetry of the d-orbitals. Here, $\boldsymbol{K}$ is the vector that translates to the K point, $\boldsymbol{D}(S)$ is the atomic displacement vector, which changes with the stacking S. Furthermore, τ is equal to 1 for the K point and -1 for the K$'$ point. Furthermore, $\phi_{l'}(S) = e^{i\Delta l'(S)2\pi/3}$, where

$\Delta l'(S) = (-1)^{l'}$ for the valence band in H-type and 0 otherwise [43]. This stems from the difference in the rotational quantum numbers where $m = -$ for the valence band and $m = 0$ for the conduction band [28]. Finally, $t^\lambda_{ll'}(S)$ is the stacking dependent tunneling strength for either electrons or holes and $T^\lambda_{ll'}(S)$ is the matrix element for said tunneling.

Importantly, we can now read off how the tunneling around the K-point will behave at each high symmetry stacking. Applying the corresponding atomic displacement for each stacking we find that both R^M_h and R^X_h become 0, and are thus symmetry forbidden. In the case of R^h_h, we instead have $T^\lambda_{ll'}(S) = 3t^\lambda_{ll'}(S)$ (for simplicity we will just incorporate the factor 3 inside of $t^\lambda_{ll'}(S)$ for future uses), which means that the tunneling matrix element is either 0 or directly proportional to the tunneling strength. Similarly, in H-type we find that the only symmetry allowed tunneling for holes are at H^h_h and for electrons at H^X_h. For other valleys such as Γ and $\Lambda^{(\prime)}$, the tunneling for each stacking will simply be proportional to the tunneling strength, which means that all non-zero tunneling matrix elements can be written as $T^\lambda_{ll'}(S) = t^\lambda_{ll'}(S)$.

The tunneling strength can be obtained by considering a two-band model for the conduction/valence band, i.e one band in each layer where the charge-carrier will tunnel between. The Hamiltonian then reads

$$H = \sum_{\alpha l \boldsymbol{k}} \tilde{E}^\alpha_{l\boldsymbol{k}}(S)\, a^\dagger_{\alpha l \boldsymbol{k}} a_{\alpha l \boldsymbol{k}} + \sum_{\substack{\alpha \boldsymbol{k} \\ l \neq l'}} t^\alpha_{ll'}(S)\, a^\dagger_{\alpha l \boldsymbol{k}} a_{\alpha l' \boldsymbol{k}}, \qquad (3.10)$$

where $\alpha = (\lambda, \xi)$ is a compound index for the band and valley. Here, $\tilde{E}^\alpha_{l\boldsymbol{k}}(S) = E^\alpha_{l\boldsymbol{k}} + \Delta\varepsilon^\lambda_l(S)$, where $E^\alpha_{l\boldsymbol{k}}$ are the decoupled monolayer band edge energies and $\Delta\varepsilon^\lambda_l(S)$ is the alignment shift discussed in 3.2. Analytically diagonalizing this Hamiltonian with respect to the layer index yields the avoided crossing formula

$$\mathcal{E}^\alpha_{\pm,\boldsymbol{k}}(S) = \frac{1}{2} \sum^2_{l=1} \widetilde{E}^\alpha_{l\boldsymbol{k}}(S) \pm \frac{1}{2}\sqrt{\widetilde{\Delta}^\alpha_{\boldsymbol{k}}(S)^2 + 4|t^\alpha(S)|^2}. \qquad (3.11)$$

Here, $\widetilde{\Delta}^\alpha_{\boldsymbol{k}}(S) = \widetilde{E}^\alpha_{1\boldsymbol{k}}(S) - \widetilde{E}^\alpha_{2\boldsymbol{k}}(S)$ and $\mathcal{E}^\alpha_{\pm,\boldsymbol{k}}(S)$ is the final hybrid energies. Solving for the tunneling strength we then obtain

$$|t^\alpha(S)| = \frac{1}{2}\sqrt{(\Delta\mathcal{E}^\alpha_{\boldsymbol{k}}(S))^2 - \widetilde{\Delta}(S)^2}, \qquad (3.12)$$

where $\Delta\mathcal{E}_{\boldsymbol{k}}^{\alpha}(S) = \mathcal{E}_{+,\boldsymbol{k}}^{\alpha}(S) - \mathcal{E}_{-,\boldsymbol{k}}^{\alpha}(S)$ is the difference between the layer hybridized electronic states. Thus, with access to the alignment shift (section 3.2), the monolayer band edges and the bilayer band edges, we can extract the tunneling strength under the assumption of a two-band model. The monolayer band energies and bilayer band energies were calculated using DFT by Christopher Linderälv in paper I.

The extracted tunneling strength for each material and valley (see appendix for paper I) differs vastly depending on the valley. Around the K (K′) point the tunneling strength is much weaker than around the the Γ or Λ point. This stems from the orbital composition of the valley. As discussed previously, the K (K′) point has its dominating contribution from the d-orbitals around the metal atom, whereas the Γ/Λ point also has a significant contribution from the chalcogen atoms, which results in a much greater wave function overlap between the layers due to the atoms being closer to each other than the metal atoms. The tunneling strength also varies with stacking. Each stacking has a different optimal interlayer distance, which directly translates into the tunneling strength, i.e longer interlayer distance gives smaller tunneling strength due to reduced wave function overlap. Since each high symmetry stacking has a different optimal interlayer distance, a twisted structure will have a varying interlayer distance throughout its supercell, which in turn means that the tunneling strength varies in the supercell. Following the same approach for the tunneling strength as for the alignment shift, we now use Eq. 3.7 to smoothly interpolate between the high symmetry stackings and consequently map out the tunneling strength in the entire supercell. In turn we can formulate the twist angle dependent Hamiltonian for the tunneling in real space as

$$H_T = \sum_{\substack{n \neq m \\ \lambda \boldsymbol{r}}} T_{nm}^{\lambda}(\boldsymbol{r})\Psi_n^{\lambda\dagger}(\boldsymbol{r})\Psi_m^{\lambda}(\boldsymbol{r}),$$

(3.13)

where $T_{nm}^{\lambda}(\boldsymbol{r})$ is the calculated map of the carrier tunneling.

3.4   Atomically reconstructed moiré potential

So far we have only discussed the potentials that emerge in a rigid lattice. However, when the relative twist angle between the layers is small, the lat-

tice does no longer remain rigid. Here, the atoms undergoes a relaxation process known as atomic reconstruction where the more energetically favorable stackings grow in size to form large domains, separated by a thin domain wall [84–92]. In R-type stacking, we have two high symmetry stackings that are optimal in terms of stacking energy R_h^M and R_h^X, thus the resulting domain formation is triangular [80, 93, 94]. In H-type, the situation is qualitatively different. Here, H_h^h is the single most optimal stacking, in turn resulting in hexagonal domain formation, also known as a kagome pattern [80, 93, 94]. The domain formation occurs due to atomic displacement, either in the form of atomic dilation (also refereed to as scalar strain within this thesis), or atomic rotation, which connects to shear strain [86]. The emerging strain fields in a reconstructed lattice consequently impacts the electronic band structure and will thus become an additional component of the moiré potential.

Assuming only small displacements, we can in the small twist-angle-regime model the strain in continuum mechanics via the linear strain tensor

$$\varepsilon_{ij} = \frac{1}{2}(u_{i,j} + u_{j,i}) \tag{3.14}$$

where ε_{ij} is the linear strain tensor and $i(j) = (x,y)$ is an index denoting the x or y-coordinate. Here, $u_{i,j}$ is the derivative $u_{i,j} = \frac{1}{2}(\partial_i u_j + \partial_j u_i)$ of the displacement vector determining the local displacement of one coordinate $\boldsymbol{r}$ with some distance $\boldsymbol{u}(\boldsymbol{r})$. In order to gain access to the strain fields in the atomically reconstructed lattice, it is thus essential to obtain the displacement vectors $\boldsymbol{u}(\boldsymbol{r})$. For this purpose we to set up an energy integral for the twisted bilayer system which depends on the displacement vectors $\boldsymbol{u}(\boldsymbol{r})$ and then minimize it in terms of stacking energy. This is done by first considering the total elastic energy. Following the theory of elasticity, the total elastic energy per unit volume can be written as [95]

$$\mathcal{U}^l = \frac{\lambda}{2}(u_{i,i}^l)^2 + \mu u_{i,j}^l u_{j,i}^l, \tag{3.15}$$

where λ and μ are the material specific Lamé parameters.

With the total elastic energy taken into account, we also need to take into account the stacking energy, also known as the adhesion energy [80], between the layers. Following the method laid out in Ref.[80], this is taken into

account via a parameterized form of the adhesion energy which is then fitted to data from DFT. The expression for the adhesion energy then reads

$$W_{R/H}(\mathbf{r}_0) = -\kappa \mathcal{Z}_{R/H}^2(\mathbf{r}_0)$$
$$+ \sum_{n=0}^{2} \Big[a_1 \cos(\mathbf{G}_n \mathbf{r}_0) + a_2 \sin(\mathbf{G}_n \mathbf{r}_0 + \gamma_{R/H}) \Big], \tag{3.16}$$

where R/H denotes R-type and H-type stacking respectively, and the phase is given by $\gamma_R = \pi/2 (\gamma_H = 0)$. Here, $\mathbf{r}_0 = \theta \hat{z} \times \mathbf{r} + \mathbf{u}^t(\mathbf{r}) - \mathbf{u}^b(\mathbf{r})$, which means that $\mathbf{G}_n \mathbf{r}_0 \approx \mathbf{g}_n \mathbf{r} + \mathbf{G}_n \Delta \mathbf{u}(\mathbf{r})$, where $\Delta \mathbf{u}(\mathbf{r}) = \mathbf{u}^t(\mathbf{r}) - \mathbf{u}^b(\mathbf{r})$ and $\mathbf{g}_n$ is the reciprocal vector of the mini-Brillouin zone (mBZ). Furthermore, $\mathcal{Z}_{R/H}(\mathbf{r}_0)$ is the deviation of the interlayer distance from d_0 nm [96], given by

$$Z_{R/H}(\mathbf{r}_0) = \frac{1}{2\kappa} \sum_{n=0}^{2} \Big[a_1 A \cos(\mathbf{G}_n \mathbf{r}_0)$$
$$+ a_2 |\mathbf{G}_n| \sin(\mathbf{G}_n \mathbf{r}_0 + \gamma_{R/H}) \Big]. \tag{3.17}$$

The parameters κ, a_1, a_2 and A are all fitted from DFT simulations and are obtained from [96]. The total stacking energy can then by described with the following integral [93, 96]

$$\mathcal{E} = \int_{\mathcal{A}_{\mathrm{M}}} d^2 \mathbf{r} \Big[\sum_l \mathcal{U}^l + W_{R/H}(\mathbf{r}_0) \Big], \tag{3.18}$$

where $\mathcal{A}_{\mathrm{M}}$ is the moiré unit cell area and $\mathbf{r}$ is the real space coordinate in the moiré lattice. To find the relevant displacement vectors $\mathbf{u}^l(\mathbf{r})$, we expand them as a Fourier series $\mathbf{u}^l(\mathbf{r}) = \sum_n \mathbf{u}_n^l e^{i\mathbf{g}_n \mathbf{r}}$ and turn the problem into an optimization problem, which can then be solved numerically for the Fourier coefficients [93, 94, 96]. The numerical implementation of the optimization problem was done by Johannes Abelardo Pineiro in paper IV using the python library GEKKO optimization suite [97].

With access to the displacement fields we can write out the linear strain tensor in its entirety[2]

$$\varepsilon_{ij}^l = \begin{pmatrix} u_{x,x}^l & \frac{1}{2}(u_{x,y}^l + u_{y,x}^l) \\ \frac{1}{2}(u_{y,x}^l + u_{x,y}^l) & u_{y,y}^l \end{pmatrix}, \tag{3.19}$$

---

[2]Note that with access to the numerically obtained Fourier coefficients for the displacement vectors, all of the entries in the linear strain tensor can be solved analytically since the real-space derivative now only acts on the exponential in the Fourier series.

which is a second-rank tensor belonging to the D3h symmetry group. Consequently, in 2D $u_{i,j}^l$ transforms according to scalar component $u_{x,x}^l + u_{y,y}^l$ ($\mathrm{Tr}(\varepsilon_{ij}^l)$) and a vector component $(u_{x,x}^l - u_{y,y}^l, -2u_{x,y}^l)$ [98–100]. Since we are interested in the effect reconstruction has on the exciton energy landscape, we are mainly interested in what impact the strain has on electronic bands. For this purpose, we can associate the scalar component as uniaxial strain in each direction and the vector component as a vector gauge potential [101], also known as piezo potential [80, 102].

Here, one component directly scales with the trace of the linear strain tensor, whereas the second component scales with the shear strain as well. It is therefore of interest to investigate how the trace and shear strain manifests themselves in the superlattice and how they evolve with the twist angle. One common way of measuring the shear strain is via the maximum shear strain value $\gamma_{\max} = u_{\max} - u_{\min}$ [86], where $u_{\max,\min}$ is given by

$$u_{\max,\min} = \frac{\mathrm{Tr}(\varepsilon_{ij})}{2} \pm \sqrt{\frac{(\varepsilon_{11} - \varepsilon_{22})^2}{2} + \varepsilon_{12}\varepsilon_{21}}. \tag{3.20}$$

In Fig 3.3.a-b we have calculated this for the example material WSe$_2$-WSe$_2$ using H-type stacking. Here we can see that the shear strain is accumulated along the domain walls for small angles (see $\theta = 0.6°$) and when the angle is increased the domains become less pronounced, which reduces the strain (see $\theta = 1.8°$). The same holds for the scalar strain which is shown in Fig 3.3.c-f. Here, we also see concentrated strain along the domain walls. Notably, the strain has the reversed sign in the top layer compared to the bottom. This stems from the relaxation process where the optimal stacking will emerge by one layer having compressive strain where the other has tensile strain.

3.4.1 Scalar strain

The potential associated with the scalar strain can be directly determined from the linear dependence on the uni/biaxial strain [103]. We can thus write the scalar strain potential as

$$S_{\xi\lambda}^l(\mathbf{r}) = \sum_i u_{i,i}^l(\mathbf{r})g_{\xi\lambda}^l = \mathrm{Tr}(\varepsilon_{ij}^l)g_{\xi\lambda}^l, \tag{3.21}$$
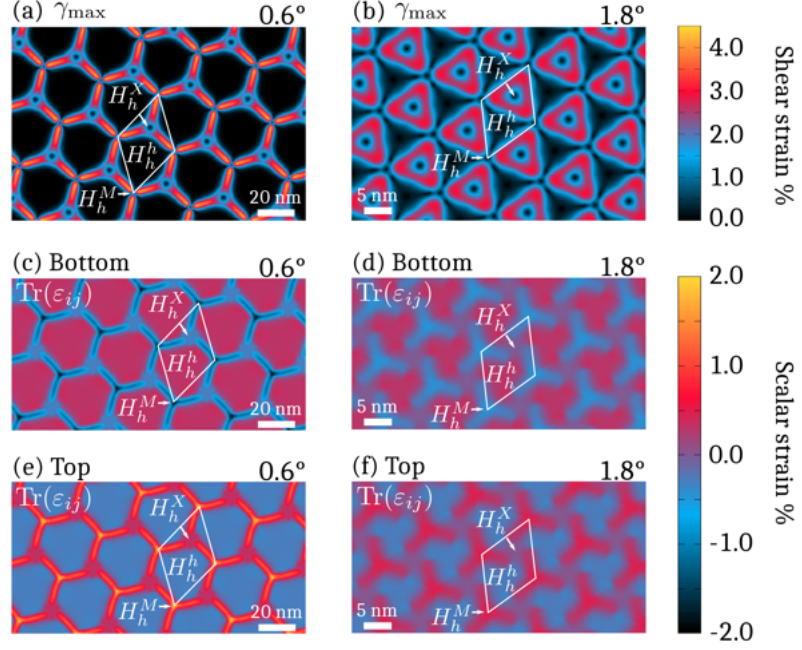
Figure 3.3: Calculated strain fields for the example material WSe$_2$ homobilayer. The shear strain profile is shown at **(a)** $\theta = 0.6°$ and **(b)** $\theta = 1.8°$. **(c-f)** Scalar strain profile for both top and bottom layer at $\theta = 0.6°$ and $\theta = 1.8°$.

where $g_{\xi\lambda}^l$ the valley-specific gauge factor obtained from the DFT calculations performed in Ref.[103]. The scalar strain potential Hamiltonian then reads

$$H_S = \sum_{n\lambda\boldsymbol{r}} S_{n\lambda}(\boldsymbol{r})\Psi_n^{\lambda\dagger}(\boldsymbol{r})\Psi_n^\lambda(\boldsymbol{r}), \qquad (3.22)$$

where n again is a generic index, now containing both the valley and layer index.

3.4.2 Piezo potential

In order to obtain the potential associated with the shear strain we will first consider the relationship between the polarization $\mathcal{P}_i^l$ and the linear strain tensor [104]

$$\mathcal{P}_i^l = \sum_{jk} u_{j,k}^l e_{ijk}^l, \qquad (3.23)$$

39

where e^l_{ijk} is the piezoelectric tensor component. Similarly to the strain tensor, the piezoelectric tensor belongs to D3h and will thus only have certain components contributing. These are [105]

$$e^l_{11} = e^l_{111} = -e^l_{122} = -e^l_{212} = -e^l_{221}, \tag{3.24}$$

where we have dropped the third index and only use e^l_{11} as the piezo coefficient from now on. The resulting polarization is the vector component of the linear strain tensor established previously multiplied by the piezo coefficient

$$\mathcal{P}^l(\mathbf{r}) = e^l_{11}(u^l_{x,x} - u^l_{y,y}, -2u^l_{x,y}). \tag{3.25}$$

By aligning the y-axis of the polarization with the vector from the metal atom to the chalcogen atom we have $e^0_{11} = -e^1_{11} > 0$ for H-type configuration and $e^0_{11} = e^1_{11}$ for R-type configuration [80]. The value of the piezo coefficients are obtained from Ref.[106]. Note that there is no polarization in uniformly strained lattices without a shear component. Via Gauss law one can write the charge distribution with respect to the polarization

$$\rho^l_{\text{piezo}}(\mathbf{r}) = -\nabla_{\mathbf{r}} \cdot \mathcal{P}^l(\mathbf{r}). \tag{3.26}$$

By including the out-of-plane direction it reads

$$\rho^l_{\text{piezo}} = -e^l_{11}\Big[2\partial_x u^l_{x,y} + \partial_y(u^l_{x,x} - u^l_{y,y})\Big]\delta(z - z_l). \tag{3.27}$$

In addition to the piezo charge density, there is also the screening-induced charge density given by the Poisson equation

$$\frac{\rho_{\text{ind}}}{\alpha^l_{\parallel}} = \delta(z - z^l)\nabla^2_{\mathbf{r}}\phi(\mathbf{r}, z), \tag{3.28}$$

where $\phi(\mathbf{r}, z)$ is the electrostatic potential produced by the piezo charges and $\alpha^l_{\parallel} = d_0\epsilon_0(1 - \epsilon^l_{\parallel})$ is the in-plane polarizability [80]. Here, $\epsilon^l_{\parallel}$ is the in-plane dielectric screening obtained from Ref.[77]. The total charge density $\rho_{\text{tot}} = \rho_{\text{ind}} + \rho_{\text{piezo}}$ and the piezoelectric potential can then be found by solving the full Poisson equation, which is done by expanding the piezo potential as a Fourier expansion $\phi(\mathbf{r}, z) = \sum_n \tilde{\phi}_n(z)e^{i\mathbf{g}_n \cdot \mathbf{r}}$ and solving for matching boundary conditions of the two dielectric slabs [80]

$$[\partial^2_{zz} + \nabla^2_{\mathbf{r}}]\phi(\mathbf{r}, z) = (\rho^{l=0}_{\text{tot}} + \rho^{l=1}_{\text{tot}})/\epsilon_0. \tag{3.29}$$

The piezo-induced energy shifts of a charge carrier $P_l^\lambda(\mathbf{r})$ is then directly obtained from the piezo potential for each layer $\phi_l(\mathbf{r})$, i.e $P_l^\lambda(\mathbf{r}) = e_0 \phi_l(\mathbf{r})$. The corresponding Hamiltonian then reads

$$H_P = \sum_{n\lambda\boldsymbol{r}} P_{n\lambda}(\boldsymbol{r}) \Psi_n^{\lambda\dagger}(\boldsymbol{r}) \Psi_n^\lambda(\boldsymbol{r}), \tag{3.30}$$

where similarly to previous potentials n is a generic index contain the layer index l.

3.4.3 Deformation of the rigid lattice potentials

The last thing to take into account in the reconstructed moiré potential is the deformation of the potentials already existing in the rigid lattice. This is simply done by considering the coordinate to be $\boldsymbol{r}_0$ instead of $\boldsymbol{r}$, i.e we transform the coordinate system in Eq. 3.7 to be $\boldsymbol{g}_n \boldsymbol{r} \rightarrow \boldsymbol{g}_n \boldsymbol{r} + \boldsymbol{G}_n \Delta \mathbf{u}^l(\mathbf{r})$. The resulting expression then reads

$$U_{nn}^\lambda(\mathbf{r}) = \mathrm{Re}\left[v_n^\lambda + (\mathcal{A}_n^\lambda + \mathcal{B}_n^\lambda e^{i2\pi/3}) \sum_{h=0}^2 e^{i(\mathbf{g}_h \cdot \mathbf{r} + \mathbf{G}_h \cdot \Delta \mathbf{u}^l(\mathbf{r}))} \right]. \tag{3.31}$$

Here, we have deformed the otherwise smooth potential with the displacement $\Delta \mathbf{u}^l(\mathbf{r})$ and thus allowed it to follow the domain formation. The same can then be done for the interlayer tunneling (3.3).

Combining all the different component, the total moiré potential Hamiltonian reads

$$\begin{aligned} H_M = &\sum_{n\lambda\mathbf{r}} S_{nn}^\lambda(\mathbf{r}) \Psi_n^{\lambda\dagger}(\mathbf{r}) \Psi_n^\lambda(\mathbf{r}) + \sum_{n\lambda\mathbf{r}} P_{nn}^\lambda(\mathbf{r}) \Psi_n^{\lambda\dagger}(\mathbf{r}) \Psi_n^\lambda(\mathbf{r}) \\ &+ \sum_{n\lambda\mathbf{r}} U_{nn}^\lambda(\mathbf{r}) \Psi_n^{\lambda\dagger}(\mathbf{r}) \Psi_n^\lambda(\mathbf{r}) + \sum_{\substack{n\neq m \\ \lambda\mathbf{r}}} T_{nm}^\lambda(\mathbf{r}) \Psi_n^{\lambda\dagger}(\mathbf{r}) \Psi_m^\lambda(\mathbf{r}), \end{aligned} \tag{3.32}$$

where we have taken into account the scalar strain $S_{nn}^\lambda(\mathbf{r})$, the piezo potential $P_{nn}^\lambda(\mathbf{r})$, the alignment shift $U_{nn}^\lambda(\mathbf{r})$ and the interlayer tunneling $T_{nm}^\lambda(\mathbf{r})$. Since the scalar strain, piezo potential and alignment shift all acts as a renormal-

ization of the band edges, we can merge them to one expression

$$H_M = \sum_{n\lambda\mathbf{r}} V_{nn}^\lambda(\mathbf{r})\Psi_n^{\lambda\dagger}(\mathbf{r})\Psi_n^\lambda(\mathbf{r}) + \sum_{\substack{n\neq m \\ \lambda\mathbf{r}}} T_{nm}^\lambda(\mathbf{r})\Psi_n^{\lambda\dagger}(\mathbf{r})\Psi_m^\lambda(\mathbf{r}). \qquad (3.33)$$

Here, $V_{nn}^\lambda(\mathbf{r}) = S_{nn}^\lambda(\mathbf{r}) + P_{nn}^\lambda(\mathbf{r}) + U_{nn}^\lambda(\mathbf{r})$.

Key message: Stacking two layers on top of each other allows for interlayer excitons, which can be taken into account by generalizing the the screening in the Wannier equation. The presence of another layer induces multiple interlayer couplings which become periodic with the introduction of a twist angle. The couplings can be summarized as the polarization-induced alignment shift, interlayer tunneling, scalar strain potential and piezo potential, which all are components to the total moiré potential.

CHAPTER 4

Exciton Landscape

In the previous chapter we covered the different interlayer coupling mechanisms that emerges when stacking two TMDs on top of each other. In this chapter we will generalize our picture for the exciton energies from the decoupled monolayer (i.e using the screening discussed in section 3.1) to also include these couplings and then summarize the resulting impact on the exciton energy landscape from these effects (paper I). For this purpose we start in the decoupled monolayer basis (i.e using the screening discussed in section 3.1) and then add the relevant interlayer couplings on top of that as modifications to these energies. For a bilayer without any moiré effects, these couplings would be the polarization-induced alignment shift (section 3.2) and the interlayer tunneling (section 3.3). After obtaining the exciton energy landscape, we also briefly cover the optical observables from said landscape in the form of phonon-assisted PL. This chapter summarizes the results from paper I, which includes results for different material configurations. However, in this chapter will only cover the results for the heterostructure MoS_2-WS_2, but the approach and general conclusions drawn can be extended to the other material configurations as well.

4.1 Energetic landscape

In order to calculate the exciton energies in TMD bilayers, we first transform the Hamiltonian in Eq. 3.10 to exciton basis via the approach laid out in subsection 2.3.2

$$H = \sum_{\substack{\xi \boldsymbol{Q} \\ LL'}} (E_{L\boldsymbol{Q}}^{\xi}(S) X_{L\boldsymbol{Q}}^{\xi\dagger} X_{L\boldsymbol{Q}}^{\xi} \delta_{LL'} + T_{LL'}^{\xi}(S) X_{L\boldsymbol{Q}}^{\xi\dagger} X_{L',\boldsymbol{Q}}^{\xi}), \tag{4.1}$$

where $E_{L\boldsymbol{Q}}^{\xi}(S)$ are the exciton binding energies solved from the general Wannier equation in Eq. 3.1 in combination with the stacking (S) dependent alignment shift discussed in section 3.2, which for an untwisted structure is just a valley-independent renormalization. The exciton tunneling matrix element now reads

$$T_{LL'}^{\xi}(S) = \mathcal{F}_{LL'}^{\xi}(t_{l_e l'_e}^{c\xi_e}(S)\delta_{l_e,l'_e-1}\delta_{l_h,l'_h} \\ -t_{l_h l'_h}^{v\xi_h}(S)\delta_{l_h,l'_h-1}\delta_{l_e,l'_e}), \tag{4.2}$$

where the deltas ensure single carrier tunneling processes and $t_{l_\lambda l'_\lambda}^{\lambda\xi_\lambda}(S)$ are the stacking dependent tunneling strength discussed in section 3.3. Here, $\mathcal{F}_{LL'}^{\xi}$ are the exciton formfactors which reads

$$\mathcal{F}_{LL'}^{\xi} = \sum_{\boldsymbol{k}} \Psi_{\xi L}^{*}(\boldsymbol{k})\Psi_{\xi L'}(\boldsymbol{k}), \tag{4.3}$$

where $\Psi_{\xi L}(\boldsymbol{k})$ are the exciton wavefunctions as obtained from the generalized Wannier equation (Eq. 3.1 and Eq. 3.3). An illustration of the hybridization process that then occur for excitons, taking into account both the alignment shift and interlayer tunneling, can be seen in Fig 4.1.c. Here, the decoupled monolayer energies of the interlayer and intralayer exciton are shifted by the alignment shift $\Delta\varepsilon(S)$ which is then split into two hybrid exciton states. It is important to note here that the tunneling channel for which intralayer excitons and interlayer exciton couple to each other change drastically with stacking. If we consider a homobilayer at R_h^h stacking (here there is no polarization-induced alignment shift) we will have two degenerate (note that including spin indices will add another level of degeneracy to the system, but can in this context of the exciton landscape be neglected [1]) intralayer excitons

---

[1]If we consider electron-hole exchange processes, the inclusion of the spin might however bring some smaller quantitative changes [107].
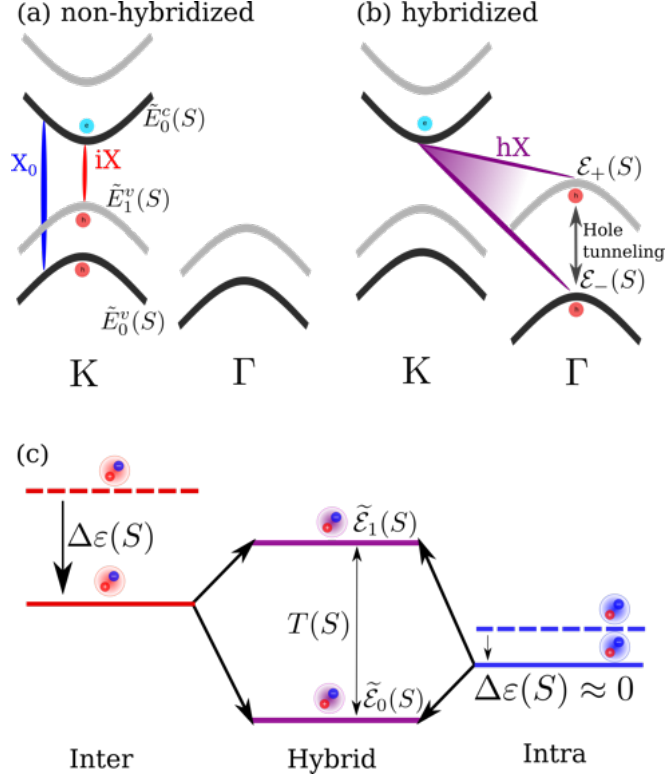
Figure 4.1: **(a)** Schematic of the electronic band structure in MoS_2(black)-WS_2(gray) heterostructure (a) before and (b) after hybridization. The intralayer (X_0) and interlayer (iX) excitons are marked in blue and red, respectively. The strong tunneling of holes around the Γ point results in a pronounced hybrid exciton state (hX, purple line). **(c)** Schematic for the formation of hybrid excitons. The dashed lines are the unperturbed exciton energies that become shifted by $\Delta\varepsilon(S)$ due to the layer polarization. Interlayer hybridization results in hybrid exciton states denoted by $\widetilde{\mathcal{E}}_\eta(S)$.

(one for each layer) and two degenerate interlayer excitons ($l_e = 0, l_h = 1$ and $l_e = 1, l_h = 0$) that couple to each other via carrier tunneling (cf. Fig 4.2.a).

Normally we only think of the KK exciton, also known as the A exciton, but we also have the B exciton (K'K'). Due to the large spin-orbit coupling in TMDs these excitons are very far up in energy and can thus be neglected usually, which is the case in R-type structures (see X_B and IX' in Fig 4.2.a). However, in H-type structures one layer has the reversed spin-orbit coupling, which fundamentally changes interlayer tunneling channels allowed. In this
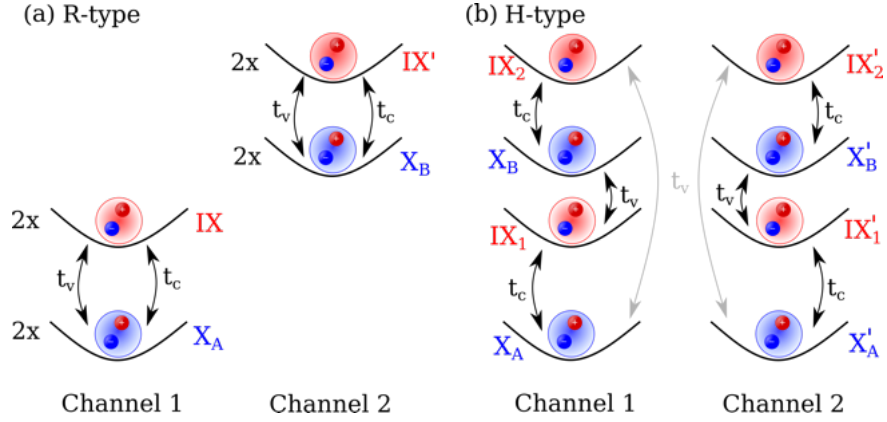
Figure 4.2: Schematic for the different tunneling channels in R-type structures **(a)** and H-type structures **(b)**. Here, 2x notes that the exciton state is two-fold degenerate. In H-type structures K′ is on top of K thus creating fundamentally different tunneling channels. This allows for the lowest lying interlayer exciton to hybridize with the B exciton.

stacking, the degeneracy of the excitons with respect to the tunneling channel is now broken, and now the A exciton couples to the B exciton. Consequently, we have a new set of interlayer excitons that in turn can hybridize with the B exciton (cf. Fig 4.2.b).

Having formulated a Hamiltonian for the exciton energies in exciton basis in Eq. 4.1, we now wish to diagonalize it. For this purpose we expand the exciton operator into a hybrid exciton basis [42, 43]

$$Y^{\dagger}_{\boldsymbol{\xi}\eta\boldsymbol{Q}} = \sum_L \mathcal{C}^{\boldsymbol{\xi}\eta*}_L(\boldsymbol{Q}) X^{\xi\dagger}_{L\boldsymbol{Q}}, \qquad (4.4)$$

where η is the new hybrid exciton quantum number, $Y^{\dagger}_{\boldsymbol{\xi}\eta\boldsymbol{Q}}$ are the hybrid exciton operators and $\mathcal{C}^{\boldsymbol{\xi}\eta}_L(\boldsymbol{Q})$ are the mixing coefficients revealing the relative contribution between intra/interlayer exciton states. Since the mixing coefficients are eigenvectors to the Hamiltonian they fulfill the following requirements

$$\sum_L \mathcal{C}^{\boldsymbol{\xi}\eta_1*}_L(\boldsymbol{Q}) \mathcal{C}^{\boldsymbol{\xi}\eta_2}_L(\boldsymbol{Q}) = \delta_{\eta_1\eta_2}$$
$$\sum_\eta \mathcal{C}^{\boldsymbol{\xi}\eta*}_L(\boldsymbol{Q}) \mathcal{C}^{\boldsymbol{\xi}\eta}_{L'}(\boldsymbol{Q}) = \delta_{LL'}. \qquad (4.5)$$
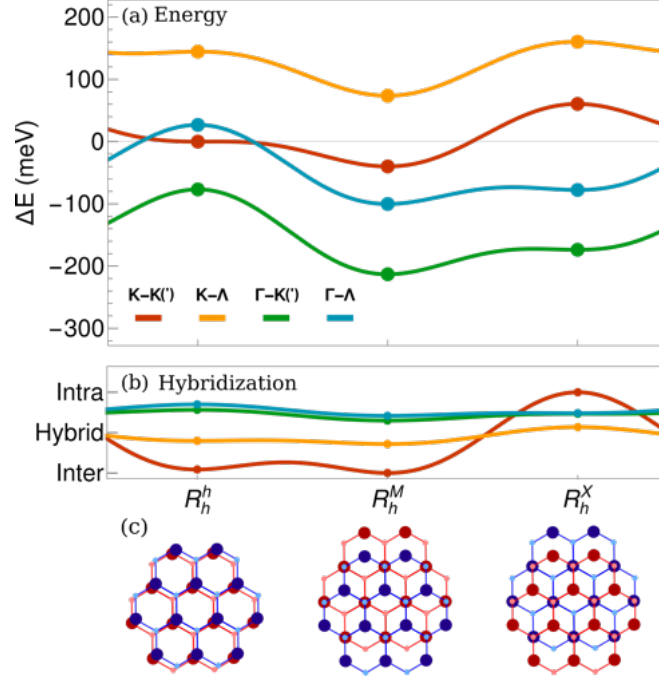
Figure 4.3: (**a**) Lowest lying exciton state for each exciton valley configuration as a function of stacking for the MoS$_2$-WS$_2$ heterostructures on a SiO$_2$ substrate. All energies are expressed in relation to the bright K-K exciton at R_h^h. Note that K-K and K-K′ as well as Γ-K and Γ-K′ are almost degenerate. (**b**) Degree of hybridization for each exciton valley as a function of stacking. (**c**) Schematic for R-type stacking configurations, where blue indicates the WS$_2$ and red the MoS$_2$ layer.

Applying the following transformation to the exciton Hamiltonian gives us the hybrid exciton eigenvalue equation

$$E_{L\boldsymbol{Q}}^{\xi}(S)\mathcal{C}_{L\boldsymbol{Q}}^{\xi\eta} + \sum_{L'} T_{LL'}^{\xi}(S)\mathcal{C}_{L'\boldsymbol{Q}}^{\xi\eta} = \mathcal{E}_{\eta\boldsymbol{Q}}^{\xi}(S)\mathcal{C}_{L\boldsymbol{Q}}^{\xi\eta}. \tag{4.6}$$

Here, $\mathcal{E}_{\eta\boldsymbol{Q}}^{\xi}(S)$ are the final hybrid exciton energies. Solving this numerically, which is the equivalent of diagonalizing a 4×4 matrix, we obtain the diagonal form of the interaction free bilayer exciton Hamiltonian.

$$H_0 = \sum_{\boldsymbol{Q}\boldsymbol{\xi}\eta} \mathcal{E}_{\eta\boldsymbol{Q}}^{\boldsymbol{\xi}}(S)Y_{\boldsymbol{\xi}\eta\boldsymbol{Q}}^{\dagger}Y_{\boldsymbol{\xi}\eta\boldsymbol{Q}}. \tag{4.7}$$

47

This was done for the van der Waals heterostructure MoS$_2$-WS$_2$ in paper I for different R-type stackings and valleys. The resulting exciton band structure is shown in Fig 4.3.a, where the lowest lying exciton for each valley is shown as a function of stacking (cf. Fig 4.3.c). Here we can see the strong impact of the carrier tunneling, consequently making the ΓK exciton the lowest lying one. The variation in energy between different stackings can mainly be explained by the varying interlayer distance, which in turn heavily impacts the tunneling strength. In Fig 4.3.b we see how the degree of hybridization changes with stacking, revealing a very small change for the momentum dark excitons. Interestingly, we find that the intralayer KK exciton no longer is the lowest lying one when going between R_h^M to R_h^X. Here, the alignment shift blueshifts this exciton sufficiently for the low lying interlayer exciton to become the lowest lying one.

4.2 Optical response

Now when we have access to the hybrid exciton energy landscape we wish to know what the corresponding optical response is. In the example material used here (MoS$_2$-WS$_2$), the momentum dark excitons are by far the lowest. Consequently, this exciton energy landscape is not directly accessible via optical absorption or via direct emission of a photon. Instead, the exciton will first need to scatter with a phonon to virtual bright state and then emit a photon. This phonon-assisted recombination of said exciton will then result in multiple phonon sidebands emerging from the scattering process, in turn giving us the optical response of the material via the photoluminescence (PL) spectra. This phonon-assisted PL formula discussed in subsection 2.4.2 was first derived by Samuel Brem et al. in Ref. [68] and then later generalized to bilayers in Ref. [43].

The phonon-assisted PL was calculated in Fig 4.4.a for R_h^h stacking, corresponding to the hybrid exciton band structure shown in Fig 4.3. Here, one can see the clear dominance of the phonon-assisted PL peaks at low temperatures and at higher temperatures the KK exciton will again dominate the spectrum. This is due to the Boltzmann nature of the exciton distri-
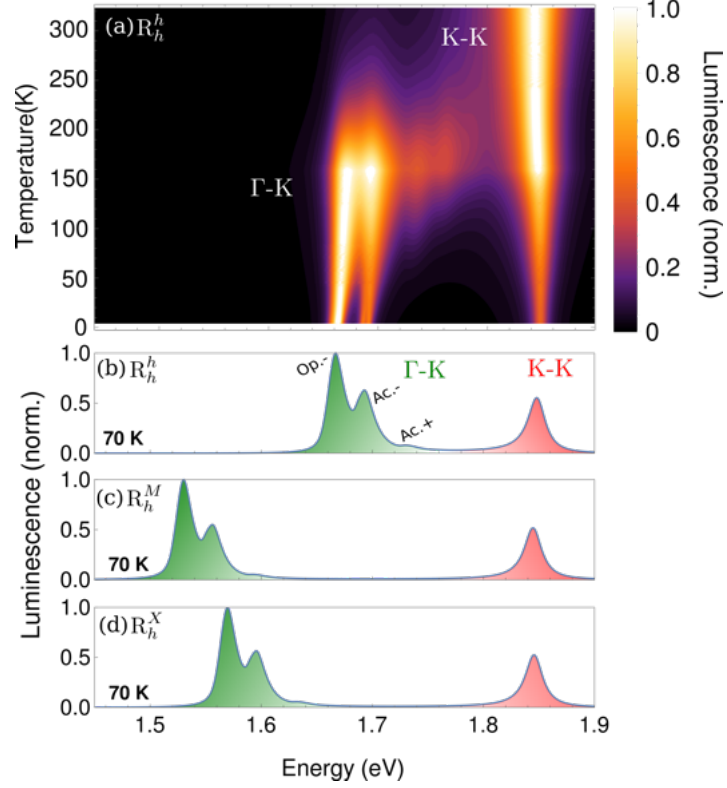
Figure 4.4: **(a)** Normalized photoluminescence spectra as a function of temperature and energy for R_h^h-stacking in the MoS$_2$-WS$_2$ heterostructure. PL spectra at 70 K for **(b)** R_h^h, **(c)** R_h^M and **(d)** R_h^X stacking. The green and the red shaded areas indicate the phonon sidebands of the Γ-K exciton and the K-K intralayer exciton, respectively. Phonon sidebands stemming from emission (−) and absorption (+) of optical (Op) and acoustical (Ac) phonons are labeled accordingly.

bution[2], where the direct emission, which corresponds to the leading order term, will gain a larger occupation. This in turn will affect the PL intensity for said peaks. At the lower temperatures the process of emitting a phonon is the dominating one. This is due to the number of phonons scaling with temperature. In the intermediate temperature range, we can see phonon absorption appearing as well. Furthermore, we can see the clear splitting between the optical and acoustic phonon modes since these will not have the same phonon energies [49, 54]. The hybrid exciton energies have then been

---

[2]The exciton distribution will in reality follow a Bose-Einstein distribution, but can be well approximated as a Boltzmann distribution at low densities [43, 68].
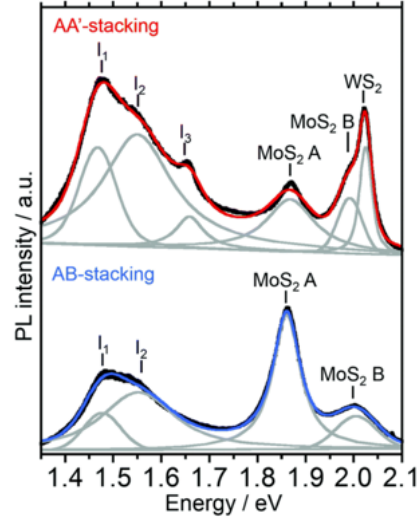
Figure 4.5: Experimental PL measurement of MoS_2-WS_2. Figure taken from Ref.[111].

redshifted(blueshifted) with these phonon energies, which then determines the relative position to A exciton (KK) peak[3]. This peak is in turn fitted to experimental observations since calculating the absolute PL peak position would require reliable first principle calculations concerning the band gap. For the purpose of this PL calculation, the linewidth has been phenomenologically modeled in accordance with Ref. [69].

Looking at Fig 4.4.a to Fig 4.4.c we see the how this optical response varies with stacking, again reflecting the strong variation of tunneling strength due to the changing interlayer distance. The above calculated results are in good agreement with experimental findings, where two predicted phonon sidebands have been observed about 300 meV below the bright K-K exciton in MoS_2-WS_2 [111] (compare AB stacking in Figure 4.5 with calculated PL spectrum in Figure 4.4.c). This corresponds well to the calculated PL at R_h^M- and R_h^X-stacking, which is the energetically most favorable R-type stackings.

Key message: In bilayer TMDs, the interlayer tunneling can drastically change the exciton energy landscape. Strongly hybridized momentum-dark

---

[3]Additional energy renormalizations will appear due to exciton-exciton interactions, but since these only become significant at higher densities they have been neglected here [108–110].

excitons will often become the new exciton ground state. These can be optically accessed via phonon-assisted PL.

CHAPTER 5

Electrical tuning of moiré excitons

In the previous chapter we summarized the results from paper I where the hybrid exciton landscape was modeled, taking into account the untwisted bilayer modifications to the monolayer exciton energies. In this chapter we will generalize this approach to include a twist angle. Furthermore, we will investigate how one can exploit the insights made in chapter 4 in order to externally tune the optical response of the material. We do this by studying the interplay between twist angle engineering of a rigid lattice and an applied electric field. This chapter consequently summarizes the theory and results from paper II. Here, the material investigated is the homobilayer $MoSe_2$, which was chosen due to the close proximity between momentum indirect and momentum direct excitons, thus making it an interesting material to study when changing both the twist angle and an applied electric field. The approach is however general can be applied to any material configuration.

5.1 Moiré exciton Hamiltonian

The first thing we need to do is generalize our exciton Hamiltonian for the inclusion of twist angles. As discussed in chapter 3, both the alignment shift and the interlayer tunneling is dependent on the atomic configuration, and will thus be periodic in real space, i.e both are components of the moiré potential. Our aim is then to generalize the model so that it will incorporate these periodic features over the whole superlattice.

We start by considering a Hamiltonian for the rigid lattice moiré potential. In real space, this is simply the sum of the two Hamiltonians given in chapter 3 by Eq. 3.8 and Eq. 3.13.

$$H_M = \sum_{i\lambda\boldsymbol{r}} V_{ii}^\lambda(\boldsymbol{r})\Psi_i^{\lambda\dagger}(\boldsymbol{r})\Psi_i^\lambda(\boldsymbol{r}) + \sum_{\substack{i\neq j \\ \lambda\boldsymbol{r}}} T_{ij}^\lambda(\boldsymbol{r})\Psi_i^{\lambda\dagger}(\boldsymbol{r})\Psi_j^\lambda(\boldsymbol{r}) + h.c. \qquad (5.1)$$

Here, $i(j) = (l,\xi)$ is a compound index, $\boldsymbol{r}$ is the real space coordinate in the superlattice and $\Psi^{(\dagger)}$ are annihilation (creation) operators. The first term accounts for the periodic alignment shift (section 3.2) and the second term accounts for the interlayer tunneling (section 3.3).

We can approximate the wave functions in the vicinity of high symmetry points as plane waves $\Psi_i^{\lambda\dagger}(\boldsymbol{r}) = \sum_{\boldsymbol{k}} e^{i\boldsymbol{k}\cdot\boldsymbol{r}}\lambda_{i,\boldsymbol{k}}^\dagger$ due to the effective mass approximation made in section 2.2. This is analogous to Fourier transforming the Hamiltonian to momentum space

$$H_M = \sum_{\substack{i\lambda \\ \boldsymbol{k}\boldsymbol{g}}} v_{ii}^\lambda(\boldsymbol{g})\lambda_{i,\boldsymbol{k}+\boldsymbol{g}}^\dagger\lambda_{i,\boldsymbol{k}} + \sum_{\substack{i\neq j\lambda \\ \boldsymbol{g}\boldsymbol{k}\boldsymbol{q}}} t_{ij}^\lambda(\boldsymbol{g})\lambda_{i,\boldsymbol{k}+\boldsymbol{g}}^\dagger\lambda_{j,\boldsymbol{k}} + h.c, \qquad (5.2)$$

where $\boldsymbol{g}$ are the reciprocal lattice vectors of the mini Brillouin zone (mBZ) that emerges due to the real space superlattice (cf. Fig 5.1). This vector is consequently defined as $\boldsymbol{g} = \boldsymbol{G}_1 - \boldsymbol{G}_2$, where $\boldsymbol{G}_l$ are the reciprocal lattice vector of layer l. The above equation is obtained by expanding the periodic moiré potential as a Fourier series

$$V_{ii}^\lambda(\boldsymbol{r}) = \sum_{\boldsymbol{g}} v_{ii}^\lambda(\boldsymbol{g})e^{i\boldsymbol{g}\cdot\boldsymbol{r}}. \qquad (5.3)$$

Here, the mBZ lattice vectors $\boldsymbol{g}$ are the eigenmodes of this expansion. Consequently, the matrix elements in Eq. 5.2 are simply the Fourier coefficients
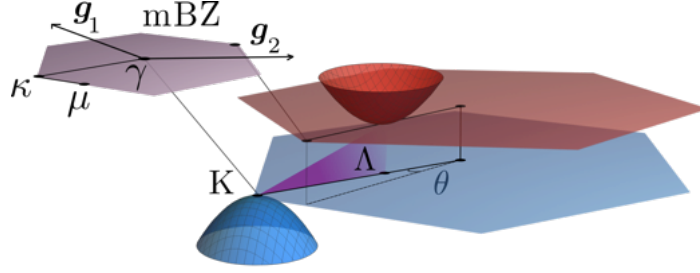
Figure 5.1: Schematic of the mini-Brillouin zone that emerges due to the emergence of a real space superlattice and a schematic interpretation of the hybrid moiré excitons that will be heavily affected by the twist angle.

of this expansion and can be obtained by solving the following integral

$$v_{ii}^{\lambda}(\boldsymbol{g}) = \frac{1}{\mathcal{A}_{\mathrm{M}}} \int_{\mathcal{A}_{\mathrm{M}}} d\boldsymbol{r} e^{-i\boldsymbol{g}\cdot\boldsymbol{r}} V_{ii}^{\lambda}(\boldsymbol{r}), \tag{5.4}$$

where $\mathcal{A}_{\mathrm{M}}$ is the unit area of the superlattice. Here, the polarization-induced alignment shift is used an example, but the same approach is done for the tunneling as well.

Applying the exciton transformation from section 2.3 we can now write down the complete interaction-free exciton Hamiltonian

$$\begin{aligned} H_0 &= \sum_{LQ\boldsymbol{\xi}} E_{LQ}^{\boldsymbol{\xi}} X_{L,Q}^{\boldsymbol{\xi}\dagger} X_{L,Q}^{\boldsymbol{\xi}} + \sum_{\substack{LQ\boldsymbol{\xi} \\ \boldsymbol{g}}} V_L^{\boldsymbol{\xi}}(\boldsymbol{g}) X_{L,Q+\boldsymbol{g}}^{\boldsymbol{\xi}\dagger} X_{L,Q}^{\boldsymbol{\xi}} \\ &+ \sum_{\substack{LL' \\ Q\boldsymbol{\xi}\boldsymbol{g}}} T_{LL'}^{\boldsymbol{\xi}}(\boldsymbol{g}) X_{L,Q+\boldsymbol{g}}^{\boldsymbol{\xi}\dagger} X_{L',Q}^{\boldsymbol{\xi}} + h.c, \end{aligned} \tag{5.5}$$

Here, the first term accounts for the dispersion

$$E_{LQ}^{\boldsymbol{\xi}} = \hbar^2 \frac{(\boldsymbol{Q} - [\xi_e - \xi_h])^2}{2[m_e + m_h]} + \varepsilon_{\xi_e 0}^c - \varepsilon_{\xi_h 0}^v + E_{\boldsymbol{\xi}}^{\mathrm{b}}, \tag{5.6}$$

where $E_{\boldsymbol{\xi}}^{\mathrm{b}}$ are the exciton binding energies and $\varepsilon_{\boldsymbol{\xi}_\lambda}^{\lambda}$ is the valley splitting (Ref. [48]).

The matrix element of the polarization-induced alignment shift is given by

$$V_L^{\boldsymbol{\xi}}(\boldsymbol{g}) = v_{l_e}^c(\boldsymbol{g}) \mathcal{F}_{LL}^{\boldsymbol{\xi}}(\beta_{LL}\boldsymbol{g}) - v_{l_h}^v(\boldsymbol{g}) \mathcal{F}_{LL}^{\boldsymbol{\xi}*}(-\alpha_{LL}\boldsymbol{g}), \tag{5.7}$$

where $v_{l_\lambda}^\lambda(\boldsymbol{g})$ are the Fourier coefficients as obtained from Eq. 5.4 and $\mathcal{F}_{LL'}^{\boldsymbol{\xi}}(\boldsymbol{q})$ are the form factors given by

$$\mathcal{F}_{LL'}^{\boldsymbol{\xi}}(\boldsymbol{q}) = \sum_{\boldsymbol{k}} \Psi_L^{\boldsymbol{\xi}*}(\boldsymbol{k})\Psi_{L'}^{\boldsymbol{\xi}}(\boldsymbol{k}+\boldsymbol{q}). \tag{5.8}$$

The tunneling matrix element is similarly given by

$$\begin{aligned}
T_{LL'}^{\boldsymbol{\xi}}(\boldsymbol{g}) = \Big[& \delta_{l_h,l_h'}(1-\delta_{l_e,l_e'})t_{l_e l_e'}^{c\boldsymbol{\xi}_e}(\boldsymbol{g})\mathcal{F}_{LL'}^{\boldsymbol{\xi}}(\beta_{LL'}\boldsymbol{g}) \\
& -\delta_{l_e,l_e'}(1-\delta_{l_h,l_h'})t_{l_h l_h'}^{v\boldsymbol{\xi}_h}(\boldsymbol{g})\mathcal{F}_{LL'}^{*\boldsymbol{\xi}}(-\alpha_{LL'}\boldsymbol{g}) \Big],
\end{aligned} \tag{5.9}$$

where the delta functions ensure that only one electron or hole can tunnel at the same time and $t_{l_\lambda l_{\lambda'}}^{\lambda\boldsymbol{\xi}_\lambda}(\boldsymbol{g})$ are the Fourier coefficients of the real space tunneling landscape, in analogy to Eq. 5.4.

In a similar fashion as in chapter 4 we want to find a diagonal form for the Hamiltonian in Eq. 5.5. Before we can to this we must first deal with the additional periodicity of the superlattice. This is done by considering the zone-folding scheme. Here, we restrict our summation over the center-of-mass momentum $\boldsymbol{Q}$ to the mBZ and then fold the dispersion back in again with the mBZ lattice vectors $\boldsymbol{g}$ [42, 43].

$$\begin{aligned}
H_0 = & \sum_{\substack{LQ\boldsymbol{\xi} \\ \boldsymbol{g}}} E_{LQ}^{\boldsymbol{\xi}}(\boldsymbol{g})X_{L,\boldsymbol{Q}+\boldsymbol{g}}^{\boldsymbol{\xi}\dagger}X_{L,\boldsymbol{Q}+\boldsymbol{g}}^{\boldsymbol{\xi}} + \sum_{\substack{LQ\boldsymbol{\xi} \\ \boldsymbol{g}\boldsymbol{g}'}} V_L^{\boldsymbol{\xi}}(\boldsymbol{g}')X_{L,\boldsymbol{Q}+\boldsymbol{g}+\boldsymbol{g}'}^{\boldsymbol{\xi}\dagger}X_{L,\boldsymbol{Q}+\boldsymbol{g}}^{\boldsymbol{\xi}} \\
& + \sum_{\substack{LL'Q \\ \boldsymbol{\xi}\boldsymbol{g}\boldsymbol{g}'}} T_{LL'}^{\boldsymbol{\xi}}(\boldsymbol{g}')X_{L',\boldsymbol{Q}+\boldsymbol{g}+\boldsymbol{g}'}^{\boldsymbol{\xi}\dagger}X_{L,\boldsymbol{Q}+\boldsymbol{g}}^{\boldsymbol{\xi}} + h.c,
\end{aligned} \tag{5.10}$$

where $E_{LQ}^{\boldsymbol{\xi}}(\boldsymbol{g}) = E_{LQ+\boldsymbol{g}}^{\boldsymbol{\xi}}$ and the summation over $\boldsymbol{Q} \in$ mBZ. We simplify the above expression by introducing the zone-folding operators $F_{LQ\boldsymbol{g}}^{\boldsymbol{\xi}} = X_{L,\boldsymbol{Q}+\boldsymbol{g}}^{\boldsymbol{\xi}}$ and apply them to the Hamiltonian

$$\begin{aligned}
H_0 = & \sum_{\substack{LQ\boldsymbol{\xi} \\ \boldsymbol{g}}} E_{LQ}^{\boldsymbol{\xi}}(\boldsymbol{g})F_{LQ\boldsymbol{g}}^{\boldsymbol{\xi}\dagger}F_{LQ\boldsymbol{g}}^{\boldsymbol{\xi}} + \sum_{\substack{LQ\boldsymbol{\xi} \\ \boldsymbol{g}\boldsymbol{g}'}} V_L^{\boldsymbol{\xi}}(\boldsymbol{g},\boldsymbol{g}')F_{LQ\boldsymbol{g}'}^{\boldsymbol{\xi}\dagger}F_{LQ\boldsymbol{g}}^{\boldsymbol{\xi}} \\
& + \sum_{\substack{LL'Q \\ \boldsymbol{\xi}\boldsymbol{g}\boldsymbol{g}'}} T_{LL'}^{\boldsymbol{\xi}}(\boldsymbol{g},\boldsymbol{g}')F_{LQ\boldsymbol{g}'}^{\boldsymbol{\xi}\dagger}F_{LQ\boldsymbol{g}}^{\boldsymbol{\xi}} + h.c.
\end{aligned} \tag{5.11}$$

Here, $T_{LL'}^{\boldsymbol{\xi}}(\boldsymbol{g},\boldsymbol{g'}) = T_{LL'}^{\boldsymbol{\xi}}(\boldsymbol{g'} - \boldsymbol{g})$ is used as an abbreviation.

In order diagonalize this Hamiltonian we introduce a similar basis change as in chapter 4, but with the additional mBZ lattice vector as an index $Y_{\boldsymbol{\xi}\eta\boldsymbol{Q}}^{\dagger} = \sum_{\boldsymbol{g}L} \mathcal{C}_{L\boldsymbol{g}}^{\boldsymbol{\xi}\eta*}(\boldsymbol{Q}) F_{L\boldsymbol{Q}\boldsymbol{g}}^{\boldsymbol{\xi}\dagger}$. Here, $\mathcal{C}_{L\boldsymbol{g}}^{\boldsymbol{\xi}\eta*}(\boldsymbol{Q})$ not only gives us the relative contribution between intra/interlayer excitons, but also the relative contribution between the different sub-bands that emerge due to the zone-folding. These coefficients then fulfill

$$
\begin{aligned}
\sum_{L\boldsymbol{g}} \mathcal{C}_{L\boldsymbol{g}}^{\boldsymbol{\xi}\eta_1*}(\boldsymbol{Q}) \mathcal{C}_{L\boldsymbol{g}}^{\boldsymbol{\xi}\eta_2}(\boldsymbol{Q}) &= \delta_{\eta_1\eta_2} \\
\sum_{\eta} \mathcal{C}_{L\boldsymbol{g}}^{\boldsymbol{\xi}\eta*}(\boldsymbol{Q}) \mathcal{C}_{L'\boldsymbol{g'}}^{\boldsymbol{\xi}\eta}(\boldsymbol{Q}) &= \delta_{LL'} \delta_{\boldsymbol{g}\boldsymbol{g'}}.
\end{aligned}
\tag{5.12}
$$

Expanding the Hamiltonian with the mixing coefficients and summing over the quantum index η gives us the moiré eigenvalue equation

$$
\boxed{
\begin{aligned}
&E_{L\boldsymbol{Q}}^{\boldsymbol{\xi}}(\boldsymbol{g}) \mathcal{C}_{L\boldsymbol{g}}^{\boldsymbol{\xi}\eta}(\boldsymbol{Q}) + \sum_{\boldsymbol{g'}} V_L^{\boldsymbol{\xi}}(\boldsymbol{g},\boldsymbol{g'}) \mathcal{C}_{L\boldsymbol{g'}}^{\boldsymbol{\xi}\eta}(\boldsymbol{Q}) \\
&+ \sum_{L'\boldsymbol{g'}} T_{LL'}^{\boldsymbol{\xi}}(\boldsymbol{g},\boldsymbol{g'}) \mathcal{C}_{L'\boldsymbol{g'}}^{\boldsymbol{\xi}\eta}(\boldsymbol{Q}) = \mathcal{E}_{\eta\boldsymbol{Q}}^{\boldsymbol{\xi}} \mathcal{C}_{L\boldsymbol{g}}^{\boldsymbol{\xi}\eta}(\boldsymbol{Q}).
\end{aligned}
}
\tag{5.13}
$$

Solving this eigenvalue problem numerically will then yield us the energies for the diagonal form of the interaction-free hybrid moiré Hamiltonian

$$
H_0 = \sum_{\boldsymbol{Q}\boldsymbol{\xi}\eta} \mathcal{E}_{\eta\boldsymbol{Q}}^{\boldsymbol{\xi}} Y_{\boldsymbol{\xi}\eta\boldsymbol{Q}}^{\dagger} Y_{\boldsymbol{\xi}\eta\boldsymbol{Q}}.
\tag{5.14}
$$

5.2 Electrical and twist angle tuning of moiré excitons

We have now generalized the interaction-free Hamiltonian to include twist angles, thus allowing for one method of external tuning of the excitons landscape. We are also interested in the effects of applying on out-of-plane electric field. The addition of an external electric field is straight forward and the

Hamiltonian in electron-hole basis can to leading order be approximated as

$$H_{\text{field}} = -\sum_{\substack{\boldsymbol{k}l \\ \lambda}} e_0 z_l^\lambda E_z \lambda_{\boldsymbol{k}l}^\dagger \lambda_{\boldsymbol{k}l}, \tag{5.15}$$

where e_0 is the elementary charge and z_l^λ is the real space position in z-direction of electrons (holes) in layer l. Here, E_z is the electric field strength in out-of-plane direction. By transforming this Hamiltonian into exciton basis (subsection 2.3.2), we have the following expression

$$H_{\text{X}-l} = -\sum_{\boldsymbol{\xi}\boldsymbol{Q}L} d_L E_z X_{\boldsymbol{Q},L}^{\boldsymbol{\xi}\dagger} X_{\boldsymbol{Q},L}^{\boldsymbol{\xi}}, \tag{5.16}$$

where $d_L = e_0 u_L$ is the dipole moment and $u_L = z_l^c - z_l^v$ the dipole length. This is intuitively understood as the potential energy of a dipole within an electrical field, sometimes referred to as the Stark shift of an exciton [112, 113]. This equation can then easily be incorporated into Eq. 5.6 and consequently be taken into account when solving Eq. 5.13.

In paper II we investigated the interplay between the two presented methods for external tuning by solving Eq. 5.13. This was done for hBN encapsulated MoSe$_2$ for both R-type stacking and H-type stacking. Here, in the top row of Fig 5.2 we see the exciton band structure for the KK exciton and the strongly hybridized KΛ exciton in a twisted R-type structure. Both the KK interlayer exciton and the KΛ exciton are heavily affected by the periodic moiré potential and will thus exhibit a flat bandstructure. The interlayer nature of these excitons are shown via the color gradient on the right where we can clearly see the strong hybrid nature of the KΛ exciton.

By applying an electric field we will then redshift (blueshift) the excitons that exhibit an out-of-plane dipole moment. Since the hybrid KΛ exciton only partially carries an interlayer component it will have a weighted shift proportional to this component $|\mathcal{C}_{\text{IX}}|^2$. We see from the bottom row of Fig 5.2 that by applying an electric field we can shift the KΛ exciton to become the lowest lying one instead of the intralayer KK, demonstrating the possibility to tune which exciton state will dominate the optical response of this material.

In Fig 5.3, the optical response for the material is calculated in the form of PL spectra (subsection 2.4.2). Here we sweep over the electrical field strength,
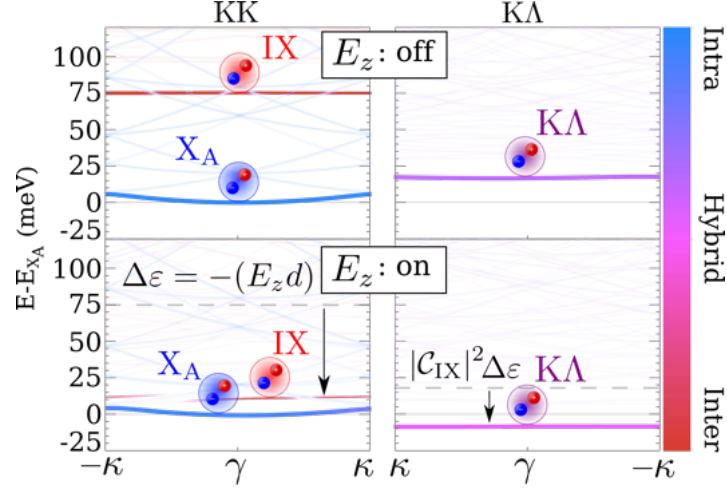
Figure 5.2: Exciton band structure for R-type stacked MoSe$_2$ homobilayer for the bright KK (left) and dark KΛ excitons (right). Multiple moiré subbands are shown in faded colors. Only the interlayer and the hybrid exciton exhibiting a dipole moment become red-shifted in presence of an electrical field (lower panel). Dashed lines indicate the original position of the corresponding excitons without an electrical field. The calculation is performed for a twist angle of $\theta = 2°$ and an electrical field of $E_z = 0.1$ V/nm.

consequently shifting both the KΛ exciton and the KK interlayer exciton downwards in the band structure. This results in three distinct optical regions in the spectra. By first looking at the untwisted case (cf. Fig 5.3.a) we see that the A exciton (KK intralayer) dominates at very small electric field strengths. Then rapidly the spectra changes to show phonon sidebands of the KΛ exciton. This is due to the KΛ exciton being redshifted sufficiently to gain enough occupation to dominate the optical response. By increasing the field strength even further the KK interlayer exciton IX is now dominating instead. Since the pure KK interlayer exciton is very weakly hybridized it carries a larger dipole moment and will thus have a steeper slope with respect to the electric field, guaranteeing a crossing between the KΛ exciton and IX at some point.

Furthermore, by introducing a twist angle (cf. Fig 5.3.b and Fig 5.3.c) we can tune the energy of the excitons that are heavily affected by the moiré potential. With the larger momentum transfer $\boldsymbol{g}$ that comes with an increased twist angle, the effects that redshifts these exciton will be suppressed, conse-
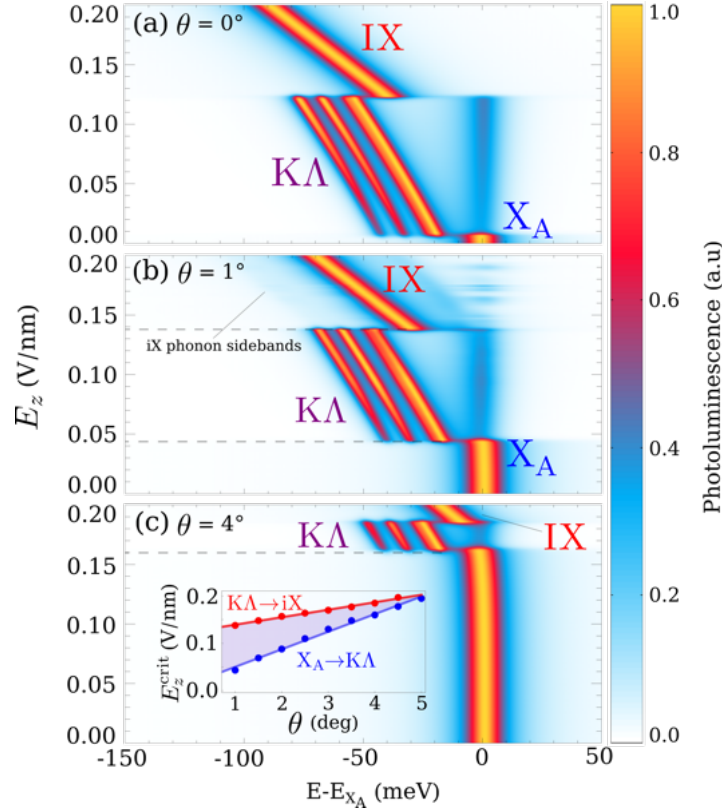
Figure 5.3: Photoluminescence spectra as a function of electrical field strength at the twist angles of **(a)** $\theta = 0°$, **(b)** $\theta = 1°$ and **(c)** $\theta = 4°$ at 4 K. We observe three distinct energy regions, which are dominated by the A exciton X_A, the phonon sidebands of the dark $K\Lambda$ exciton and the interlayer exciton IX, respectively. The inset in (c) shows the critical electrical field strength E_z^{crit} as a function of the twist angle for the transition between different spectral regions (X_A to $K\Lambda$ and X_A to IX-dominated region). The shaded area indicates the range, where the dark $K\Lambda$ excitons dominate the PL.

quently shifting the IX and $K\Lambda$ exciton upwards in the band structre. This allows us to calculate the critical fields necessary for a given twist angle when the $K\Lambda$ exciton dominates the spectra. In turn we predict when the material is transformed from a direct semiconductor (KK) to an indirect semiconductor ($K\Lambda$). Moreover, by looking at smaller twist angles (cf. Fig 5.3.b) we can see additional features due to the multiple subbands that emerge in this regime. Here, the rotation of the Brillouin zone puts the energetic minimum of the interlayer exciton IX outside of the light cone, allowing for very weak

phonon sidebands. The apparent oscillations that appear around the position of the A exciton is also due to the small twist angle. Here, the higher lying subbands of IX will be redshifted and hybridize with the A exciton when on top of it, consequently affecting the oscillator strength of the A exciton.

Key message: The moiré exciton landscape can be modeled by diagonalizing a zone-folded Hamiltonian for the exciton energies in a periodic potential. The dipolar response of an interlayer exciton can be taken into account via the linear stark effect. Hybridizing an exciton will impact the response the exciton has to the electric field by reducing/increasing its interlayer component. Twist-angle-engineering and electrical field control allows for external tuning between different exciton states. In turn going from a direct to an indirect semiconductor.

CHAPTER 6

Dehybridization of moiré excitons

In this chapter we will briefly cover the results from the theory-experiment collaboration done in paper III. In the previous chapter we discussed the important role the twist angle plays for the interlayer tunneling. However, so far we have assumed that the variation of the interlayer distance remains constant when the twist angle changes, i.e the difference between the minimum interlayer distance and the maximum does not change. This approximation holds in the small twist angle regime, but when the twist angle is increased the variation between the smallest interlayer distance in the supercell and the largest decreases [114], which in turn directly impacts the tunneling strength throughout the moiré lattice [73, 115]. This change in interlayer distance ultimately results in very large and experimentally observed blueshifts for the hybrid excitons due to the reduced tunneling strength [116]. In order to model this feature of the interlayer tunneling we construct an effective tunneling Hamiltonian, which allows for the tunneling strength variation to change with the twist angle.

In the material studied ($MoSe_2$-MoS_2), the lowest lying exciton state is a
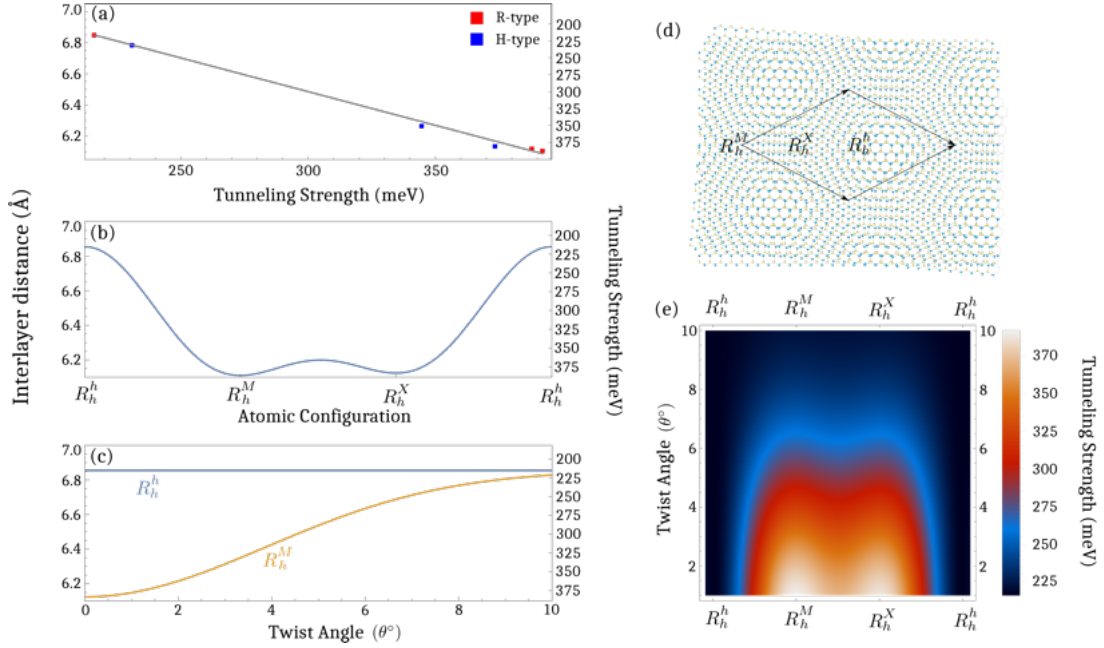
Figure 6.1: **(a)** Tunneling strength around the Γ valley as a function of interlayer distance. **(b)** Interlayer distance (left axis) and tunneling strength around the Γ valley (right axis) in different parts of the superlattice **(d)**. **(c)** Gaussian increase of interlayer distance as a function of twist angle. Here, we allow the R_h^M configuration to approach the interlayer distance of R_h^h. **(e)** Evolution of tunneling strength around the Γ valley for different sites in the superlattice when increasing twist angle.

ΓK exciton [117]. The tunneling of interest to model is therefore around the Γ valley. By plotting out the the different tunneling strengths for each high symmetry stacking as a function of its respective interlayer distance (cf. Figure 6.1.a) we can see that the tunneling strength around the Γ valley is approximately linear with the changing interlayer distance within this range. This allows us to directly translate the variation of the interlayer distance in the supercell to the tunneling strength as shown in Figure 6.1.b.

Importantly, in Ref. [114, 115] it is shown that the variation of the interlayer distance in the supercell becomes less pronounced with increased twist angle. This decrease in the interlayer distance variation is approximately Gaussian and will effectively suppress the periodic modulation of the tunneling strength (cf. Figure 6.1.c) [115]. Due to the linearity between interlayer

distance and tunneling, we can directly model the tunneling strength, where its periodic modulation is suppressed at higher twist angles. Here we do this by considering the approach laid out in the previous chapters, where we smoothly interpolate between the different high symmetry points

$$t = t_0 + \left[\alpha + \beta e^{i2\pi/3}\right] \sum_{n=0}^{2} e^{i\boldsymbol{g}_n \cdot \boldsymbol{r}}. \tag{6.1}$$

Here, the parameters t_0, α and β are fitted to meet the condition at the high symmetry stackings. We now let the periodic variation of the tunneling strength decay with twist angle as a Gaussian and converge towards some specific value

$$t_{l_\lambda l'_\lambda}^{\lambda \xi_\lambda}(\boldsymbol{r}) = t^\lambda(d_{\max}) + e^{-\theta^2/\theta_0^2}\left(t_0^{\lambda \xi_\lambda} + \left[\alpha^{\lambda \xi_\lambda} + \beta^{\lambda \xi_\lambda} e^{i2\pi/3}\right] \sum_{n=0}^{2} e^{i\boldsymbol{g}_n \cdot \boldsymbol{r}}\right), \tag{6.2}$$

where $t^\lambda(d_{\max})$ is the tunneling strength that is present when the periodic modulation has disappeared at large twist angles. In paper III, this is taken to be were the interlayer distance is the largest, which corresponds to the tunneling strength at R_h^h stacking. Furthermore, $t_0^{\lambda \xi_\lambda}$ is chosen so that for small θ, the maximum tunneling strength corresponds to the value in the untwisted case. The exponential $e^{-\theta^2/\theta_0^2}$ takes into account the approximate Gaussian increase of the interlayer distance that occurs throughout the supercell. With this effective model for tunneling strength around the Γ valley we have a clear twist angle dependence for the tunneling as can be seen in Figure 6.1.c. The evolution of the tunneling strength through the superlattice can be seen in Figure 6.1.e, where we see the tunneling strength converging towards the same value $t^\lambda(d_{\max})$.

Once the real space map of the the tunneling strength has been obtained (Figure 6.1.e), we can follow the same approach as in chapter 5 and decompose the the tunneling as a Fourier series

$$t_{l_\lambda l'_\lambda}^{\lambda \xi_\lambda}(\boldsymbol{r}) = \sum_{\boldsymbol{g}} t_{l_\lambda l'_\lambda}^{\lambda \xi_\lambda}(\boldsymbol{g}) e^{i\boldsymbol{g} \cdot \boldsymbol{r}}, \tag{6.3}$$

where $t_{l_\lambda l'_\lambda}^{\lambda \xi_\lambda}(\boldsymbol{g})$ can be calculated by solving the integral Fourier coefficients

$$t_{l_\lambda l'_\lambda}^{\lambda \xi_\lambda}(\boldsymbol{g}) = \frac{1}{\mathcal{A}_M} \int_{\mathcal{A}_M} d\boldsymbol{r} e^{-i\boldsymbol{g} \cdot \boldsymbol{r}} t_{l_\lambda l'_\lambda}^{\lambda \xi_\lambda}(\boldsymbol{r}). \tag{6.4}$$
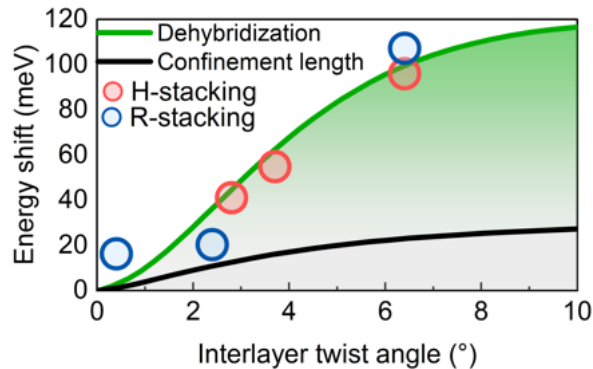
Figure 6.2: Comparison between the calculated ΓK exciton energies and the experimentally observed peak shifts as a function of twist angle. Here, the solid line black line is the calculated shift without taking into account the effects of increasing interlayer distance and the solid green line is with the effects taken into account. The experimental data points are given by the red/blue dots.

This allows us, to incorporate the twist-angle-dependent tunneling strength into the moiré exciton Hamiltonian in Eq. 5.5 and then diagonalize as done in chapter 5.

Comparing the twist-angle-dependence of the ΓK energies with the experimental measurements we find qualitatively good agreement, where both the observed PL peaks and the energies are drastically blue shifted due to the reduced tunneling strength as can be seen in Fig 6.2. Here, the experiments are given by the red/blue dots and were carried out by the group of Paulina Plochocka at LNCMI in Toulouse. The calculated exciton energies are given by the solid green line and as a comparison the expected blue shift when not taken into account the increase in interlayer distance is shown in black. In this case, the blue shift mainly stems from the change in confinement length instead.

Key message: At larger twist angles, the variation in the interlayer distance changes. This directly translates into the tunneling strength and effectively reduces the value of the tunneling strength due to the increased interlayer distance at some stackings. For the Γ valley this can be effectively be modeled by allowing the periodic part of the tunneling strength to decay to a certain value. The resulting exciton energies will consequently experience large blue shift when increasing the twist angle.

CHAPTER 7

Moiré excitons in a reconstructed lattice

So far we have only considered moiré excitons in a rigid lattice. While this approximation holds for larger twist angles, it is not sufficient to describe the moiré potential and the resulting exciton energies at smaller angles. Here, the lattice undergoes a relaxation process known as atomic reconstruction where the atoms are strained in order minimize the local stacking energy [80, 93, 118]. In this chapter we calculate the moiré exciton energies and their optical response, taking into account the emerging strain potentials from an atomically reconstructed lattice. Consequently, we summarize the results of paper IV by including the theory covered in section 3.4 in our framework. Here, we primarily study naturally stacked WSe_2-WSe_2, but the approach holds for all material configurations and the results are expected to be similar for all naturally stacked homobilayers.

Following the approach laid out in section 3.4 we optimize the total adhesion energy of the system, thus obtaining the Fourier coefficients for the expanded displacement vectors $\mathbf{u}^l(\mathbf{r}) = \sum_n \mathbf{u}_n^l e^{i\mathbf{g}_n \mathbf{r}}$. After obtaining the displacement vectors we can visualize how they change the geometry of the superlattice by

looking at a map of the interlayer distance. In Fig 7.1.a-b we have done this for H-type stacked WSe$_2$ homobilayer at $\theta = 0.6°$. Here, we can see that the rigid lattice (cf. Fig 7.1.b) has a smooth change in the interlayer distance, reflecting the smooth change in stacking configuration. For the reconstructed case, we instead see large hexagonal domains forming (cf. Fig 7.1.a) in good agreement with experimental observations [84, 86]. In H-type, this pattern emerges due to there only being one optimal stacking, whereas in R-type a triangular pattern would instead emerge due to R_h^M and R_h^X both being optimal stackings.

With access to the displacement fields, we now want to calculate the band edge variations. Taking into account the total moiré potential (Eq. 3.33), including both scalar strain and piezo potential described in section 3.4, we can map out the band edge variations for both the conduction and valence band. This is done in Fig 7.1.c-f for both the top and bottom layer. Here, we see that the strain has accumulated close to the domain walls, in turn making it the potential minimum for both the conduction and valence band. Note the difference in potential depth for the conduction and valence band. This stems from the scalar strain potential which directly scales with the valley gauge factor, which is different for the conduction and valence band, thus resulting in a band gap renormalization. The effective exciton potential is then given in Fig 7.1.g, where we can see that the potential depth increases by a lot when the twist angle is reduced. We can also note that the effective exciton potential is different for the KK exciton and the KΛ exciton, which again can be attributed to the scalar strain potential. Here, the difference in orbital overlap between K and Λ results in different gauge factors, and thus a different effective exciton potential depth [119].

Following the approach laid out in previous chapters, we can Fourier expand the total moiré potential (treating the layer-diagonal terms as one component and the layer-off-diagonal terms as another)

$$V_{hh}^\lambda(\mathbf{r}) = \sum_{\mathbf{g}} m_{hh}^\lambda(\mathbf{g}) e^{i\mathbf{g}\cdot\mathbf{r}}, \qquad (7.1)$$

where, $m_{hh}^\lambda(\mathbf{g})$ are the Fourier coefficients for the total layer-diagonal moiré potential (i.e no tunneling included), which are obtained by solving the in-
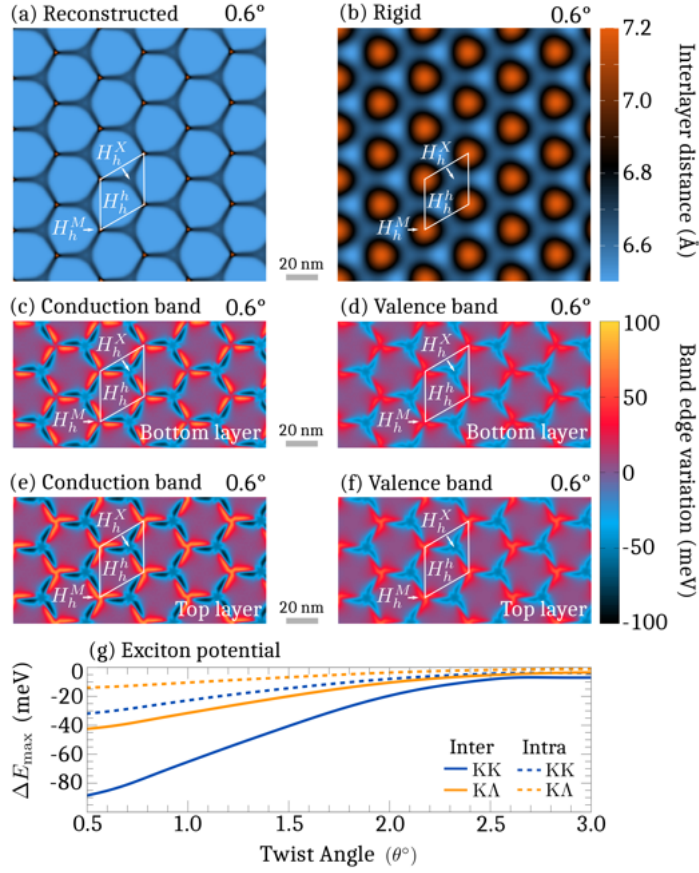
Figure 7.1: Spatial map of the interlayer distance in **(a)** a reconstructed lattice and **(b)** a rigid lattice at $\theta = 0.6°$ for H-type stacked WSe$_2$ homobilayers. The band edge variation for the conduction band in **(c)** the bottom layer and **(e)** the top layer at the K-point, and the valence band edge variation in **(d)** the bottom layer and **(f)** the top layer at the K-point. The shape of the potential stems from the linear combination of the scalar strain potential and the piezo potential. **(g)** Maximum exciton potential depth ΔE_{max} in the supercell is shown as a function of twist angle for both intralayer excitons (dashed) and interlayer excitons (solid).

tegral for the Fourier coefficients

$$m_{hh}^{\lambda}(\mathbf{g}) = \frac{1}{\mathcal{A}_{M}} \int_{\mathcal{A}_{M}} d\mathbf{r} e^{-i\mathbf{g}\cdot\mathbf{r}} V_{hh}^{\lambda}(\mathbf{r}). \qquad (7.2)$$

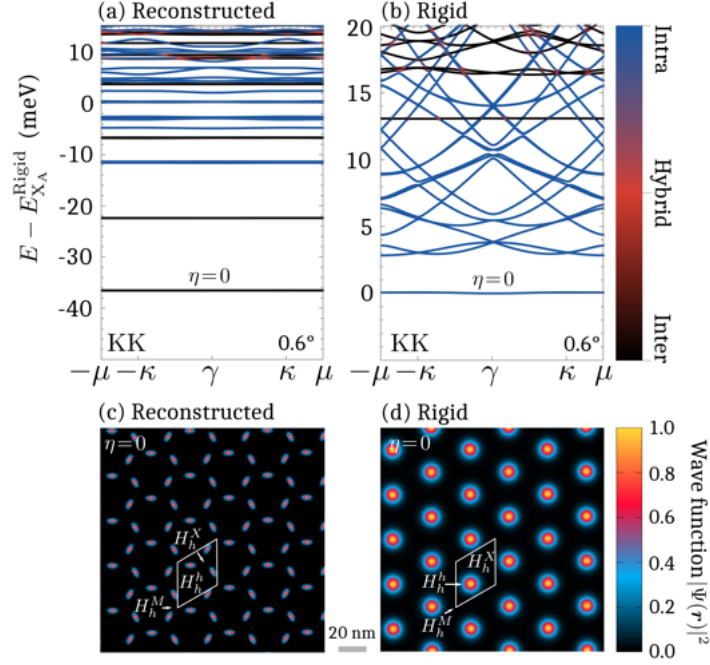With access to new moiré potential matrix elements we can formulate a

69

Figure 7.2: Band structure and wave function of the bright KK exciton in H-type stacked WSe$_2$ bilayer at $\theta = 0.6°$ in (a,c) the reconstructed lattice and (b,d) the rigid lattice. Energies are normalized to the lowest-lying KK exciton in the rigid lattice. The band index $\eta = 0$ indicates which wave function is shown.

Hamiltonian in exciton basis the same way as done in chapter 5.

$$H_0 = \sum_{L\mathbf{Q}\xi} E_{L\mathbf{Q}}^\xi X_{L,\mathbf{Q}}^{\xi\dagger} X_{L,\mathbf{Q}}^\xi + \sum_{L\mathbf{Q}\xi\mathbf{g}} M_{L\mathbf{g}}^\xi X_{L,\mathbf{Q}+\mathbf{g}}^{\xi\dagger} X_{L,\mathbf{Q}}^\xi$$
$$+ \sum_{LL'\mathbf{Q}\xi\mathbf{g}} T_{LL'\mathbf{g}}^\xi X_{L,\mathbf{Q}+\mathbf{g}}^{\xi\dagger} X_{L',\mathbf{Q}}^\xi + h.c. \tag{7.3}$$

Here, the matrix elements are given by

$$M_L^\xi(\mathbf{g}) = m_{l_e}^c(\mathbf{g})\mathcal{F}_{LL}^\xi(\beta_{LL}\mathbf{g}) - m_{l_h}^v(\mathbf{g})\mathcal{F}_{LL}^{\xi*}(-\alpha_{LL}\mathbf{g}),$$
$$T_{LL'}^\xi(\mathbf{g}) = \Big[\delta_{l_h,l'_h}(1 - \delta_{l_e,l'_e})t_{l_e l'_e}^{c\xi_e}(\mathbf{g})\mathcal{F}_{LL'}^\xi(\beta_{LL'}\mathbf{g}) \tag{7.4}$$
$$- \delta_{l_e,l'_e}(1 - \delta_{l_h,l'_h})t_{l_h l'_h}^{v\xi_h}(\mathbf{g})\mathcal{F}_{LL'}^{*\xi}(-\alpha_{LL'}\mathbf{g})\Big],$$

where $\mathcal{F}_{LL'}^\xi(\boldsymbol{q})$ are the exciton form factors. Diagonalizing the exciton Hamiltonian with the same scheme laid out in chapter 5 we can then obtain the final exciton energies and exciton wave functions in a reconstructed lattice.

7.1 Excitons in a reconstructed lattice

In paper IV we calculated the moiré exciton energies and wave functions for H-type stacked WSe$_2$ homobilayer as shown in Fig 7.2. The exciton band structure for the bright KK exciton is given for both the reconstructed case Fig 7.2.a and the rigid lattice Fig 7.2.b. The first thing to notice is that the reconstructed lattice exhibits far more flat bands than the rigid lattice. This is a direct consequence of the induced strain potentials in the reconstructed lattice. Furthermore, we can note that in the reconstruceted lattice, the interlayer (black lines) exciton has been pushed down below the intralayer excitons (blue lines). This stems from the difference in the sign between the layers in the scalar strain potential, in turn leading to a much more efficent moiré potential for the interlayer excitons.

The calculated wave function shown in Fig 7.2.c for the reconstructed lattice and Fig 7.2.d for the rigid lattice reveal that the exciton wave function drastically changes when including the effects of atomic reconstruction. Here, the exciton gets trapped close to the domain walls, reflecting the deep strain potential pockets formed. In the rigid lattice, the exciton is instead trapped at the H_h^h site. This is however a very inefficient trapping as can be seen from the energetic distance to the nearest non-flat band in the dispersion (cf. Fig 7.2.b). This very weak trapping in the rigid lattice stems from the hole tunneling around H_h^h, which in turn pins the exciton to the H_h^h sites. Overall, the trapping in the reconstructed lattice is far more efficient and in a naturally stacked homobilayer the exciton goes from nearly being free, to being very efficiently trapped.

7.2 Optical signatures of atomic reconstruction

When we have access to the moiré exciton energies in an atomically reconstructed lattice, we can calculate the optical response of this exciton landscape. Since we are here looking at bright KK excitons, we will do this in the form of optical absorption (see subsection 2.4.1). This is done in Fig 7.3 for a H-type stacked WSe$_2$ homobilayer as a function of twist angle. The first
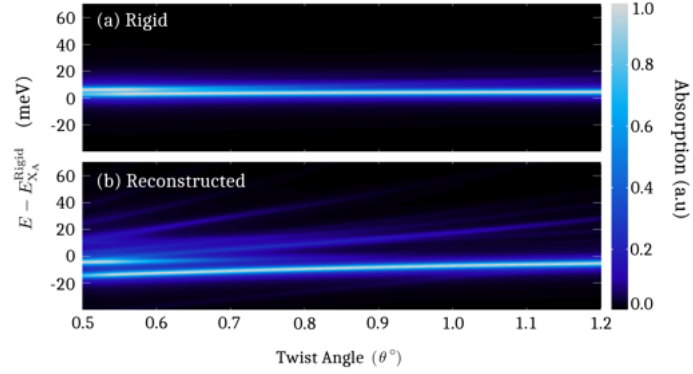
Figure 7.3: Twist-angle dependence of the normalized absorption in H-type WSe$_2$ bilayers for **(a)** the rigid lattice and **(b)** the reconstructed lattice. The emergence of multiple peaks in the latter is due to the strain-induced intralayer potential and is an unambiguous signature of lattice reconstruction.

thing to notice is the stark difference in the multi-peak-structure between the rigid lattice and the reconstructed lattice. In the rigid lattice Fig 7.3.a, we only have one peak that does no change with twist angle. Some weak splitting can be observed at small twist angles due to the limited tunneling. In contrast, the reconstructed lattice has multiple new peaks emerging when the twist angle is below 1°. Here, the induced strain potentials efficiently trap the excitons, giving rise to multiple flat-bands, together with a characteristic multi-peak optical response. Note that the interlayer excitons that become the lowest lying exciton is not visible in the absorption spectra due to its weak oscillator strength. Since the emerging sub-band peaks is not present in the rigid lattice and only emerges in the reconstructed lattice, this can be exploited as an unambiguous optical signature of atomic reconstructed in naturally stacked homobilayers.

Key message: The deformation of the lattice via atomic reconstruction can be calculated by minimizing the stacking energy. The strain potentials can then be incorporated into the total moiré potential. The exciton energies can be solved as usual by diagonalizing the moiré exciton Hamiltonian. In naturally stacked homobilayers, the induced strain potentials drastically change the exciton energy landscape for the bright KK excitons, including new trapping sites and induced flat-bands. The multi-peak structure that emerges in optical absorption can be exploited as a signature of atomic reconstruction.

CHAPTER 8

Polarization and charge-separation of moiré excitons

Throughout this thesis we have so far focused on excitons were the electron and hole sits on top of each other within the 2D-plane. This has allowed us to obtain the exciton binding energies via the Wannier equation (Equation 3.1), which in most circumstances so far has worked well. However, in some twisted heterostructures, the moiré potential will act as driving force to separate the electron and hole within the 2D-plane, which consequently allows for the formation of intralayer charge-transfer excitons [87, 120]. Here, we will generalize our approach for excitons by solving a general two-particle problem instead, which in turn will allow for charge-separation. Taking into account the total moiré potential, we then calculate the moiré site hopping within the Hubbard model [94, 121]. This chapter consequently summarizes the results from paper V. Here, we study the heterostructure $MoSe_2$-WSe_2, which is a type-II band alignment semiconductor with the lowest lying exciton state being a KK interlayer exciton [42]. Consequently, the interlayer tunneling is very weak here and can thus be neglected. In turn, this makes the material a good choice to study the impact atomic reconstruction has on the charge-separation without considering further complications regarding

exciton hybridization.

8.1 Generalized moiré exciton eigenvalue equation

In order to calculate the the exciton wave function and energy with charge separation we first formulate a Hamiltonian in single-particle picture. Here, we are only studying one type of interlayer exciton, where the electron always will be in the molebdenum layer and the hole always will be in the tungsten layer. Conseqently, we can drop the dependence on the layer index in the Hamiltonian.

$$H = \sum_{\boldsymbol{k}\lambda} \varepsilon_{\boldsymbol{k}}^{\lambda} \lambda_{\boldsymbol{k}}^{\dagger} \lambda_{\boldsymbol{k}} + \sum_{\boldsymbol{k}\boldsymbol{q}\lambda} M_{\boldsymbol{q}}^{\lambda} \lambda_{\boldsymbol{k}+\boldsymbol{q}}^{\dagger} \lambda_{\boldsymbol{k}} + \sum_{\boldsymbol{k}\boldsymbol{k}'\boldsymbol{q}} V_{\boldsymbol{q}}^{cv} c_{\boldsymbol{k}+\boldsymbol{q}}^{\dagger} v_{\boldsymbol{k}'-\boldsymbol{q}}^{\dagger} v_{\boldsymbol{k}'} c_{\boldsymbol{k}}, \qquad (8.1)$$

where $\varepsilon_{\boldsymbol{k}}^{\lambda}$ is the dispersion of the conduction/valence band and $M_{\boldsymbol{q}}^{\lambda}$ is the Fourier transformed total moiré potential from Equation 3.33 (excluding the tunneling). The calculated total moiré potential is shown as a function of twist angle for the electron, hole and exciton in Fig 8.1. Furthermore, $V_{\boldsymbol{q}}^{cv}$ (Equation 3.2) is the Coulomb matrix element responsible for the attraction between electrons and holes.

With the single-particle Hamiltonian introduced, we now introduce the general exciton two-particle state

$$|X\rangle = \sum_{\boldsymbol{k}\boldsymbol{k}'} \Psi_{\boldsymbol{k}\boldsymbol{k}'} c_{\boldsymbol{k}}^{\dagger} v_{\boldsymbol{k}'} |0\rangle = X^{\dagger} |0\rangle, \qquad (8.2)$$

where $\Psi_{\boldsymbol{k}\boldsymbol{k}'}$ is the general two-particle wave function and $X^{(\dagger)}$ the exciton annihilation (creation) operator. By letting the Hamiltonian (Equation 8.1) act upon the general exciton state we can derive an eigenvalue problem $H|X\rangle = E|X\rangle$, which then reads

$$(\varepsilon_{\boldsymbol{k}}^{c} - \varepsilon_{\boldsymbol{k}'}^{v})\Psi_{\boldsymbol{k}\boldsymbol{k}'} + \sum_{\boldsymbol{q}} \left(M_{\boldsymbol{q}}^{c}\Psi_{\boldsymbol{k}-\boldsymbol{q},\boldsymbol{k}'} - M_{\boldsymbol{q}}^{v}\Psi_{\boldsymbol{k},\boldsymbol{k}'+\boldsymbol{q}} \right)$$
$$- \sum_{\boldsymbol{q}} V_{\boldsymbol{q}}^{cv}\Psi_{\boldsymbol{k}-\boldsymbol{q},\boldsymbol{k}'-\boldsymbol{q}} = E\Psi_{\boldsymbol{k}\boldsymbol{k}'}. \qquad (8.3)$$
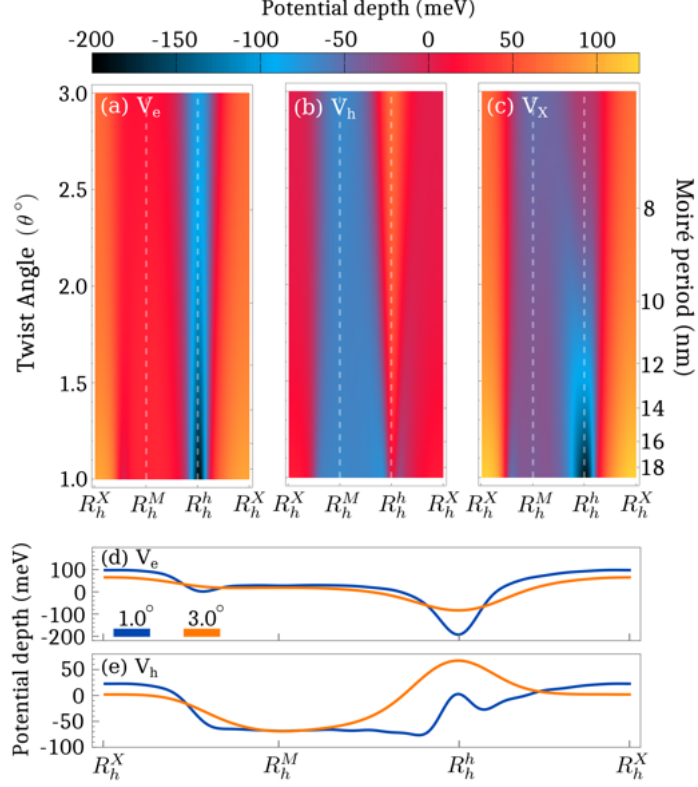
Figure 8.1: Moiré potential as a function of the twist angle and moiré period for the **(a)** electron, **(b)** hole, and **(c)** exciton potential in the R-type stacked MoSe$_2$-WSe$_2$ heterostructure. Cut of the **(d)** electron and **(e)** hole potential at $\theta = 1°$, and $\theta = 3°$.

Here, E is the exciton energy.

We now introduce the center-of-mass momentum $\boldsymbol{Q} = \boldsymbol{k}_c - \boldsymbol{k}_v = \boldsymbol{k}_e + \boldsymbol{k}_h$ such that we can map the momentum-dependence from $\boldsymbol{k}/\boldsymbol{k}'$ to $\boldsymbol{k}/\boldsymbol{Q}$. Moreover, we have now introduced the notation $\tilde{\Psi}_{\boldsymbol{k}\boldsymbol{Q}} = \Psi_{\boldsymbol{k},\boldsymbol{k}-\boldsymbol{Q}} \leftrightarrow \Psi_{\boldsymbol{k}\boldsymbol{k}'} = \tilde{\Psi}_{\boldsymbol{k},\boldsymbol{k}-\boldsymbol{k}'}$, which translates between the pictures. Applying the same zone-folding scheme as in previous chapter, but now to both $\boldsymbol{k}$ and $\boldsymbol{Q}$ with the mBZ lattice vectors $\boldsymbol{g}(\tilde{\boldsymbol{g}})$ we get zone-folded wave functions $\tilde{\Psi}_{\boldsymbol{k}+\boldsymbol{g},\boldsymbol{Q}+\tilde{g}} = \Phi_{\boldsymbol{k}\boldsymbol{Q}}(\boldsymbol{g},\tilde{\boldsymbol{g}})$. Furthermore, the moiré potential can be expressed as $M_{\boldsymbol{q}}^{\lambda} = \sum_{\boldsymbol{g}} m_{\boldsymbol{g}}^{\lambda}\delta_{\boldsymbol{q},\boldsymbol{g}}$, where $m_{\boldsymbol{g}}^{\lambda}$ are the Fourier coefficients obtained in chapter 7. The zone-folded eigenvalue problem in center-of-mass and relative momentum coordinates

then reads

$$\Delta\varepsilon_{kQ}^{cv}(\boldsymbol{g},\tilde{\boldsymbol{g}})\Phi_{k}^{Q}(\boldsymbol{g},\tilde{\boldsymbol{g}}) + \sum_{\boldsymbol{g}'\tilde{\boldsymbol{g}}'}\left(m_{\tilde{\boldsymbol{g}}-\tilde{\boldsymbol{g}}'}^{c}\delta_{\boldsymbol{g}-\boldsymbol{g}',\tilde{\boldsymbol{g}}-\tilde{\boldsymbol{g}}'}\right.$$
$$\left. - m_{\tilde{\boldsymbol{g}}-\tilde{\boldsymbol{g}}'}^{v}\delta_{\boldsymbol{g}-\boldsymbol{g}',\tilde{\boldsymbol{g}}-\tilde{\boldsymbol{g}}'}\right)\Phi_{k}^{Q}(\boldsymbol{g}',\tilde{\boldsymbol{g}}') \tag{8.4}$$
$$- \sum_{\boldsymbol{p}\boldsymbol{g}'}V_{\boldsymbol{k}-\boldsymbol{p}+\boldsymbol{g}-\boldsymbol{g}'}^{cv}\Phi_{k}^{Q}(\boldsymbol{g}',\tilde{\boldsymbol{g}}) = E_{Q}\Phi_{k}^{Q}(\boldsymbol{g},\tilde{\boldsymbol{g}}),$$

where $\Phi_{k}^{Q}(\boldsymbol{g},\tilde{\boldsymbol{g}})$ is the zone-folded two-particle wave function and E_{Q} are the exciton energies as a function of center-of-mass momentum. Here, $\Delta\varepsilon_{kQ}^{cv}(\boldsymbol{g},\tilde{\boldsymbol{g}}) = \varepsilon_{\boldsymbol{k}+\boldsymbol{g}}^{c} - \varepsilon_{\boldsymbol{k}+\boldsymbol{g}-\boldsymbol{Q}-\tilde{\boldsymbol{g}}}^{v}$ is the difference between the zone-folded conduction/valence band dispersion. By treating the eigenvalue problem as a sparse matrix to be diagonalized we can solve for the energies. This was done using the C++ library Armadillo [122, 123].

8.1.1 Charge densities

With access to the exciton energies and the two-particle wave function we can now calculate the densities for electron, hole and center-of-mass, which in turn allows us to visualize the charge separation. Starting with the electron density in real space $\rho^{e}(\boldsymbol{r}) = \langle X_{Q}|\Psi_{e}^{\dagger}(\boldsymbol{r})\Psi_{e}(\boldsymbol{r})|X_{Q}\rangle$, we expand it via the exciton state (now written in zone-folded coordinates)

$$|X_{Q}\rangle = \sum_{kg\tilde{g}}\Phi_{k}^{Q}(\boldsymbol{g},\tilde{\boldsymbol{g}})c_{\boldsymbol{k}+\boldsymbol{g}}^{\dagger}v_{\boldsymbol{k}+\boldsymbol{g}-\boldsymbol{Q}-\tilde{\boldsymbol{g}}}|0\rangle, \tag{8.5}$$

where $\Psi_{\lambda}^{\dagger}(\boldsymbol{r}) = \sum_{p}e^{i\boldsymbol{p}\cdot\boldsymbol{r}}\lambda^{\dagger}$. The derived expression for the electron density then reads

$$\rho^{e}(\boldsymbol{r}) = \sum_{\Delta}e^{i\Delta\cdot\boldsymbol{r}}\sum_{kg\tilde{g}}\Phi_{k}^{Q*}(\boldsymbol{g}+\Delta,\tilde{\boldsymbol{g}}+\Delta)\Phi_{k}^{Q}(\boldsymbol{g},\tilde{\boldsymbol{g}}), \tag{8.6}$$

where $\Delta = \boldsymbol{g}-\boldsymbol{g}'$. Doing the same to the hole density $\rho^{h}(\boldsymbol{r}) = \langle 0|\Psi_{v}^{\dagger}(\boldsymbol{r})\Psi_{v}(\boldsymbol{r})|0\rangle - \langle 0|X_{Q}\Psi_{v}^{\dagger}(\boldsymbol{r})\Psi_{v}(\boldsymbol{r})X_{Q}^{\dagger}|0\rangle$ gives us

$$\rho^{h}(\boldsymbol{r}) = \sum_{\Delta}e^{i\Delta\cdot\boldsymbol{r}}\sum_{kg\tilde{g}}\Phi_{k}^{Q*}(\boldsymbol{g},\tilde{\boldsymbol{g}}+\Delta)\Phi_{k}^{Q}(\boldsymbol{g},\tilde{\boldsymbol{g}}). \tag{8.7}$$

The center-of-mass density is derived by first introducing the relative $\boldsymbol{r} = \boldsymbol{r}_e - \boldsymbol{r}_h$ and center-of-mass coordinates $\boldsymbol{R} = \frac{1}{\mu}(m_e\boldsymbol{r}_e + m_h\boldsymbol{r}_h)$, where μ is the reduced mass, we can set up an expression for the conditional electron-hole densities

$$
\begin{aligned}
P_{eh}(\boldsymbol{r},\boldsymbol{R}) &= \langle\boldsymbol{Q}|\Psi_e^\dagger(\boldsymbol{R}+\boldsymbol{\beta r})\Psi_e(\boldsymbol{R}+\boldsymbol{\beta r})\\
&\times\Psi_h^\dagger(\boldsymbol{R}-\alpha\boldsymbol{r})\Psi_h(\boldsymbol{R}-\alpha\boldsymbol{r})|\boldsymbol{Q}\rangle\\
&= \langle 0|X_{\boldsymbol{Q}}\Psi_e^\dagger(\boldsymbol{R}+\boldsymbol{\beta r})\Psi_e(\boldsymbol{R}+\boldsymbol{\beta r})\\
&\times\Psi_h^\dagger(\boldsymbol{R}-\alpha\boldsymbol{r})\Psi_h(\boldsymbol{R}-\alpha\boldsymbol{r})X_{\boldsymbol{Q}}^\dagger|0\rangle,
\end{aligned}
\tag{8.8}
$$

where $P_{eh}(\boldsymbol{r},\boldsymbol{R}) = |\bar{\Psi}_{\boldsymbol{Q}}(\boldsymbol{r},\boldsymbol{R})|^2$ is the probability. After simplifying the expression we obtain

$$
P_{eh}(\boldsymbol{r},\boldsymbol{R}) = \sum_{\substack{k g \tilde{g} \\ k' g' \tilde{g}'}} e^{i(\tilde{\boldsymbol{g}}-\tilde{\boldsymbol{g}}')\cdot\boldsymbol{R}}e^{-i(\tilde{\boldsymbol{g}}-\tilde{\boldsymbol{g}}')\cdot\alpha\boldsymbol{r}} \times \Phi_k^{\boldsymbol{Q}*}(\boldsymbol{g},\tilde{\boldsymbol{g}})\Phi_k^{\boldsymbol{Q}*}(\boldsymbol{g}',\tilde{\boldsymbol{g}}').
\tag{8.9}
$$

Introducing the unfolded two-particle wave function $\tilde{\Phi}_{\boldsymbol{Q}}(\boldsymbol{k}+\boldsymbol{g},\tilde{\boldsymbol{g}}) = \Phi_k^{\boldsymbol{Q}}(\boldsymbol{g},\tilde{\boldsymbol{g}})$ and taking the trace of the relative electron-hole coordinates, i.e integrating over $\boldsymbol{r}$ $P_{eh}(\boldsymbol{R}) = \frac{1}{A}\int d^2r P_{eh}(\boldsymbol{r},\boldsymbol{R})$, the following expression for the COM density is obtained

$$
P_{eh}(\boldsymbol{R}) = \sum_{\Delta'} e^{i\Delta'\cdot\boldsymbol{R}}\sum_{k\tilde{g}}\tilde{\Phi}_{\boldsymbol{Q}}^*(\boldsymbol{k}+\alpha\Delta,\tilde{\boldsymbol{g}}+\Delta)\tilde{\Phi}_{\boldsymbol{Q}}(\boldsymbol{k},\tilde{\boldsymbol{g}}).
\tag{8.10}
$$

Here, $\Delta' = \tilde{\boldsymbol{g}} - \tilde{\boldsymbol{g}}'$. The resulting electron, hole and COM densities can now be written as a function of the same form factor

$$
\begin{aligned}
\rho_e(\boldsymbol{r}) &= \sum_\Delta e^{i\Delta\cdot\boldsymbol{r}}\Gamma_{\boldsymbol{Q}}(\Delta,\Delta)\\
\rho_h(\boldsymbol{r}) &= \sum_\Delta e^{i\Delta\cdot\boldsymbol{r}}\Gamma_{\boldsymbol{Q}}(0,\Delta)\\
\rho_X(\boldsymbol{R}) &= \sum_{\Delta'} e^{i\Delta'\cdot\boldsymbol{R}}\Gamma_{\boldsymbol{Q}}(\alpha\Delta',\Delta'),
\end{aligned}
\tag{8.11}
$$

where $\rho_X(\boldsymbol{R}) = P_{eh}(\boldsymbol{R})$ and the form factor is given by

$$
\Gamma_{\boldsymbol{Q}}(\boldsymbol{q},\Delta) = \sum_{kG}\tilde{\Phi}_{\boldsymbol{Q}}^*(\boldsymbol{k}+\boldsymbol{q},\boldsymbol{G}+\Delta)\tilde{\Phi}_{\boldsymbol{Q}}(\boldsymbol{k},\boldsymbol{G}).
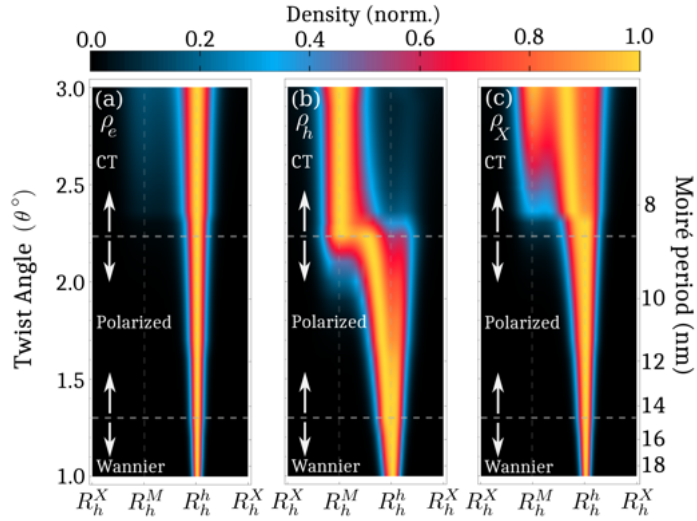\tag{8.12}
$$

Figure 8.2:   Densities $\rho_i(\boldsymbol{r})$ as a function of the twist angle and moiré period for **(a)** electrons, **(b)** holes, and **(c)** excitons (at $\boldsymbol{Q} = \boldsymbol{0}$) in an R-type stacked MoSe$_2$-WSe$_2$ heterostructure.

8.2   Twist angle-dependent charge separation

With the carrier density calculated from the two-particle wave function obtained by diagonalizing Eq. 8.4 we can study its evolution with twist angle. The results are shown in Fig 8.2.a for the electron density. Here, we can observe that the electron is very efficiently trapped at R_h^h. This mainly stems from the pronounced scalar strain potential that has accumulated at the R_h^h site (see Fig 8.1 for a plot of the potential landscape), which consequently leads to the very deep potential pockets. At larger angles, the electron instead becomes more delocalized and at $\theta > 2.2°$ the electron is now also overlapping with the hole trapping site (see faint overlap with R_h^M). The hole density is qualitatively different. Here, it is energetically unfavorable for the hole to be at R_h^h (cf. Fig 8.1.b). At small twist angles, the minimum of the hole potential instead sits very close to the electron minimum due to the large reconstructed R_h^M domains and the accumulation of strain around the domain walls (compare blue lines in Fig 8.1.d/e). This short distance between the electron and hole minima nearly puts the hole entirely on top of the electron, thus consituting a Wannier-like exciton.

When the twist angle is increased, the length scale between the electron and hole minimum change. Here, the moiré potential wants to drag the hole away from the electron, whereas the Coulomb interaction wants to pull it closer, resulting in two competing processes. In this intermediate twist-angle-range part of the hole becomes separated from the electron and one part is still overlapping with it. This separation is however still small and occurs within the expected Bohr radius ($\sim 2 - 3$ nm). We therefore denote this regime as a polarized exciton. Increasing the twist angle even further separates the charges even more. Here, the atomic reconstruction has diminished sufficiently to put the hole minimum directly at R_h^M (see Fig 8.1.b/e), which further separates the hole from the electron. In this regime, there is little overlap between the electron and hole. Furthermore, the electron and hole are separated outside the expected Bohr radius. We therefore denote this regime as intralayer charge-transfer (CT) exciton. At a supercell size about 8 nm (corresponding to $\theta \approx 2.4°$) the charges are separated about ~ 4.6 nm - in a very good agreement with previous studies on intralayer CT excitons [87, 120]. In Fig 8.2.c, the exciton center-of-mass density is shown. Here, we can observe that the exciton is indeed very localized at small twist angles. Increasing the twist angle first slowly delocalizes it due to the decrease in confinement length. When we enter the intralayer CT regime, the exciton first become more localized, but then quickly more delocalized. Here, part of the center-of-mass exciton density is over the hole trapping site and part is over the electron trapping site. However, the peak of the density is in the middle of the electron and hole, in turn reflecting the center-of-mass nature of the exciton.

8.3 Dielectric tuning of hopping parameter

With access to the exciton landscape with charge-separation taken into account, we can now calculate the inter-site hopping within the Bose-Hubbard framework. Following the approach laid out in Ref. [121], an expression for the hopping parameter t can be derived by transforming to Wannier basis [94, 121]

$$t_{ij} = \frac{1}{N} \sum_{\boldsymbol{Q}} e^{i(\boldsymbol{R}_i - \boldsymbol{R}_j) \cdot \boldsymbol{Q}} E_{\boldsymbol{Q}}, \qquad (8.13)$$
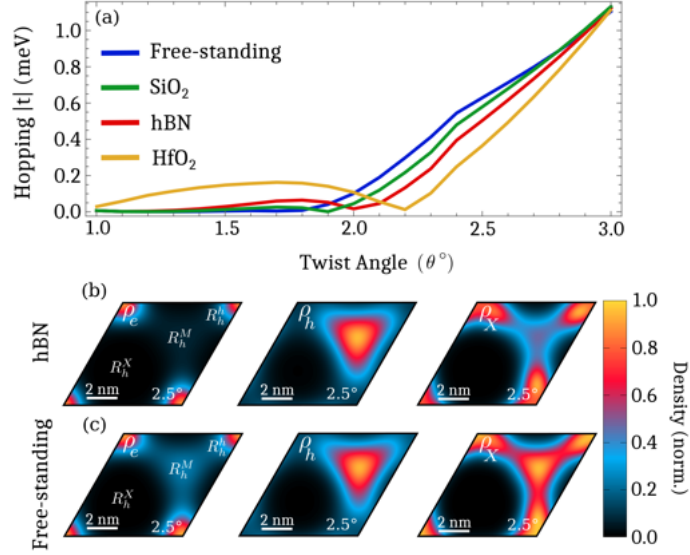
Figure 8.3: **(a)** Exciton hopping strength as a function of the twist angle for different substrates including the free-standing case (blue), SiO_2 (green), hBN (red) and HfO_2 (yellow), ranging from vanishing screening (with the dielectric constant $\varepsilon = 1$) to large screening ($\varepsilon = 16.1$) [124] in R-type stacked $MoSe_2$-WSe_2 heterostructure. The density for electrons, holes and excitons are shown in **(b)** for the case of hBN-encapsulation and in **(c)** for the free-standing case for a fixed twist angle of $\theta = 2.5°$.

where $i(j)$ is the site index, $\boldsymbol{R}_i$ is the vector translating between moiré sites, and $E_{\boldsymbol{Q}}$ is the exciton dispersion as obtained through solving the generalized moiré exciton eigenvalue equation in Eq. 8.4.

In Fig 8.3.a we show the calculated hopping for different substrates. Here, we can see that for both the hBN-encapsulated case and the proposed screening consisting of HfO_2, there is a pronounced peak emerging in the intermediate twist-angle-range. This stems from the suppression of the Coulomb interaction with stronger screening, thus enhancing the formation of polarized excitons. Here, the Bohr radius has increased due to the weaker Coulomb interaction, which allows for the electron and hole to separate more within the Bohr radius, thus delocalizing the exciton more. In contrast, the weaker screening such as SiO_2 or a freestanding sample has no peak at all. Here, the Coulomb interaction is strong enough to nearly completely suppress the formation of polarized excitons, and in turn the observed increase of the

80

hopping.

When increasing the twist angle further, the hopping decreases again for the larger screenings. This unexpected efficient trapping of excitons at larger twist angles is occurring when the the electron and holes has been individually efficiently trapped, i.e the formation of intralayer charge-transfer excitons. Interestingly, in this regime a stronger screening of the Coulomb potential results in less efficient hopping than in the intermediate twist-angle-range (compare ordering of colors for $\theta \gtrsim 2.2°$ and $\theta \approx 1.8°$). This can be understood from the difference in the overlap between electrons and holes. In the regime of intralayer CT excitons, electron and holes are clearly separated outside of the exciton Bohr radius. Decreasing the screening leads to a stronger Coulomb interaction and thus a stronger drive for electrons and holes to be on top of each other, cf. Figure 8.3b/c. This translates into a more delocalized excitons (cf. Figure 8.3.b/c) for a free-standing sample and a larger hopping strength. As a result, we have a qualitatively different behavior in the two different regimes. In the intermediate twist-angle range, excitons are more efficiently trapped by a stronger Coulomb interaction due to the suppression of polarized excitons. In contrast, in the intralayer CT exciton regime, excitons are more efficiently trapped by a weaker Coulomb interaction due to the reduced overlap between electrons and holes. Consequently, we predict that the dielectric engineering of the Coulomb potential can act as an additional external tuning knob to either enhance or suppress exciton trapping.

Key message: The charge-separated exciton energies can be calculated by considering a two-particle Hamiltonian with a total reconstructed potential acting upon a general exciton state. In twisted $MoSe_2$-WSe_2 we predict three different exciton regimes: (i) localized Wannier-like excitons, (ii) polarized excitons and (iii) intralayer charge-transfer excitons. Calculating the hopping parameter reveals an unexpected trapping at larger twist angles due the efficient localization of both electrons and holes. Both the charge-separation and the hopping can be externally tuned via substrate-controlled dielectric engineering, either enhancing or suppressing the effects of charge-separation.

CHAPTER 9

Conclusion and outlook

In this work we have presented a microscopic quantum mechanical model for the moiré exciton landscape in vertically stacked transition metal dichalcogenides, with a special emphasis on the different interlayer couplings and their dependence on the relative twist angle. In combination with input from density functional theory we have calculated the exciton energy landscape for different homo- and heterobilayers, taking into account the different components of the moiré potential. We reveal a strong impact from the interlayer tunneling, which hybridize the excitons and consequently often make them the dominating exciton species in bilayer structures. Furthermore, we have investigated the excitons optical response to both electric field tuning and twist-angle-engineering, predicting that these two external tuning knobs can control which exciton state is the lowest, in turn determining if the material is a direct or indirect semiconductor. Moreover, in a theory-experiment collaboration we demonstrate the significant impact the twist angle has on the tunneling strength at larger angles, leading to significant blue shifts and a dehybridization of the low lying hybrid excitons.

Taking into account the effects of atomic reconstruction at small twist angles, we show that the atomic relaxation induces two new components to the moiré potential in the form of scalar strain and piezo potential. By calculating the optical absorption in naturally stacked homobilayers we predict that the introduction of these new potentials drastically changes the optical response. Here, multiple new peaks emerge - in stark contrast to the rigid lattice where only one peak dominates the spectrum. In turn, this can be exploited as an unambiguous optical signature of atomic reconstruction. Furthermore, we generalize our theoretical model by solving a general two-particle problem, in turn allowing for charge separation within the 2D plane. Here, we find three different exction regimes with varying levels of charge-separation when increasing the twist angle. Finally, we calculate the inter-site hopping for these charge-separated excitons and predict an unexpected efficient trapping at larger angles, which can be externally tuned via substrate-controlled dielectric engineering. Overall, the work provides microscopic insights into the twist-angle dependent exciton landscape that governs the optical response in this technologically promising class of nanomaterials.

The advances made have opened up new questions and challenges within the field. In particular, recent studies have shown that the effective screening can be continuously and dynamically tuned by electrically doping an additional layer that is separated with hBN from the moiré structure [125]. As indicated by our results in chapter 8 this would allow for continuous control of the charge-separation. Furthermore, the charge-separation directly translates into to the effective interaction strength, where the excitons now would exhibit much larger dipoles. Consequently, there is a potential to continuously control the interaction strength, which would carry significant interest for studies on excitons at higher densities [15, 74, 75, 110, 126, 127], and for exotic phases such as Mott insulating phases and superfluidity [121]. Moreover, the increase in charge-separation would also translate into an increase in exciton lifetime, making it a suitable candidate to realize exciton condensates [128] and potentially counter-flow superconductivity [129].

The induced piezo potential in the atomically reconstructed lattice discussed in section 3.4 stems from a vector gauge potential. Analogous to a magnetic field, these vector gauge potentials can be transformed into pseudomagnetic fields [101]. In twisted bilayer TMDs the resulting pseudomagnetic fields has been predicted to reach field strengths up 50 Tesla [84]. It would therefore be

of interest to study the interplay between spin and the pseudomagnetic field, which could maybe give rise to interesting phenomena such as the quantum Hall effect [130, 131].

Furthermore, in the atomic reconstruction regime we have shown that the emergence of large domains and thin domain walls can fundamentally impact the exciton energies. This large scale reconstruction also influences the phonons of the system, leading to a phonon renormalization [132]. In this regime, the domain walls can be viewed as a soliton network [114], which in turn fluctuates themselves, leading to the formation of long range acoustic moiré phonons [132], which in another viewpoint can be seen as phonons for the superlattice itself, known as phasons [133]. It has been observed that in the small twist-angle-regime and at low temperatures, the diffusion coefficient is surprisingly converging towards a finite value, which has been attributed to the excitons surfing along the phason mediated wave [134, 135]. This phason-exciton interaction in the atomically reconstructed lattice would then not only be of interest for transport, but also for relaxation dynamics [136–139]

Finally, experimental studies have reported the observation of correlated insulating states at fractional fillings when the twist angle is sufficiently small to create flat bands [140]. A microscopic study of these so-called Wigner crystals [141], taking into account the moiré excitons in twisted bilayers could potentially reveal interesting insights into the intriguing topic of correlated states in moiré structures.

Acknowledgments

First of all, I would like to thank my supervisor, Ermin Malic for his constant support. Your guidance has motivated me to always strive for improvement and a better understanding of our research. The importance of your supervision cannot be understated, and I am grateful to have done this PhD journey with you as my supervisor. Secondly, I would like to thank my colleague Samuel Brem for your essential part in all of my research. Your questions and deep insights into the field have not only been invaluable to this work, but also helped me develop as a researcher.

I would also like to extend my gratitude to my examiner, Andreas Isacsson, for carefully reading the thesis and providing valuable feedback which helped improve the quality of this work. In this context, I would also like to thank my opponent (Thomas Heine) and the grading committee (Habib Rostami, Battulga Munkhbat, Elsebeth Schröder and Johannes Hoffman) for taking the time to read the thesis.

My thanks also goes out to the several different collaborators I had the pleasure of working with during my PhD, with a special thanks to the group of Paulina Plochocka at LNCMI in Toulouse for our collaboration regarding exciton dehybridization and quadropole excitons.

Bibliography

[1] Samer Bayda, Muhammad Adeel, Tiziano Tuccinardi, Marco Cordani, and Flavio Rizzolio. The history of nanoscience and nanotechnology: from chemical–physical applications to nanomedicine. *Molecules*, 25(1):112, 2019.

[2] Kostya S Novoselov, Andre K Geim, Sergei V Morozov, De-eng Jiang, Yanshui Zhang, Sergey V Dubonos, Irina V Grigorieva, and Alexandr A Firsov. Electric field effect in atomically thin carbon films. *science*, 306(5696):666–669, 2004.

[3] KS Novoselov. Nobel lecture: Graphene: Materials in the flatland. *Reviews of Modern Physics*, 83(3):837, 2011.

[4] AH Castro Neto, Francisco Guinea, Nuno MR Peres, Kostya S Novoselov, and Andre K Geim. The electronic properties of graphene. *Reviews of modern physics*, 81(1):109, 2009.

[5] Pablo Ares and Kostya S Novoselov. Recent advances in graphene and other 2d materials. *Nano Materials Science*, 2021.

[6] Kin Fai Mak, Changgu Lee, James Hone, Jie Shan, and Tony F. Heinz. Atomically thin MoS_2: A new direct-gap semiconductor. *Physical Review Letters*, 105:136805, 2010.

[7] Thomas Mueller and Ermin Malic. Exciton physics and device application of two-dimensional transition metal dichalcogenide semiconductors. *npj 2D Materials and Applications*, 2(1):1–12, 2018.

[8] Oriol Lopez-Sanchez, Dominik Lembke, Metin Kayci, Aleksandra Radenovic, and Andras Kis. Ultrasensitive photodetectors based on monolayer mos2. *Nature nanotechnology*, 8(7):497–501, 2013.

[9] Gang Wang, Alexey Chernikov, Mikhail M Glazov, Tony F Heinz, Xavier Marie, Thierry Amand, and Bernhard Urbaszek. Colloquium: Excitons in atomically thin transition metal dichalcogenides. *Reviews of Modern Physics*, 90(2):021001, 2018.

[10] Dmitry K Efimkin and Allan H MacDonald. Many-body theory of trion absorption features in two-dimensional semiconductors. *Physical Review B*, 95(3):035417, 2017.

[11] Raul Perea-Causin, Samuel Brem, and Ermin Malic. Trion-phonon interaction in atomically thin semiconductors. *Physical Review B*, 106(11):115407, 2022.

[12] Raul Perea-Causin, Samuel Brem, Fabian Buchner, Kenji Watanabe, Takashi Taniguchi, John M Lupton, Kai-Qiang Lin, and Ermin Malic. Electrically tunable layer-hybridized trions in doped wse $\underline{2}$ bilayers. *arXiv preprint arXiv:2404.18716*, 2024.

[13] Raul Perea-Causin, Samuel Brem, Ole Schmidt, and Ermin Malic. Trion photoluminescence and trion stability in atomically thin semiconductors. *Physical Review Letters*, 132(3):036903, 2024.

[14] Edbert J. Sie, Alex J. Frenzel, Yi-Hsien Lee, Jing Kong, and Nuh Gedik. Intervalley biexcitons and many-body effects in monolayer mos$_2$. *Phys. Rev. B*, 92:125417, Sep 2015.

[15] Samuel Brem and Ermin Malic. Optical signatures of moiré trapped biexcitons. *2D Materials*, 11(2):025030, 2024.

[16] Andre K Geim and Irina V Grigorieva. Van der Waals heterostructures. *Nature*, 499(7459):419–425, 2013.

[17] Pasqual Rivera, John R Schaibley, Aaron M Jones, Jason S Ross, Sanfeng Wu, Grant Aivazian, Philip Klement, Kyle Seyler, Genevieve Clark, Nirmal J Ghimire, et al. Observation of long-lived interlayer excitons in monolayer $MoSe_2$-WSe_2 heterostructures. *Nature Communications*, 6(1):1–6, 2015.

[18] Wugang Liao, Yanting Huang, Huide Wang, and Han Zhang. Van der waals heterostructures for optoelectronics: Progress and prospects. *Applied Materials Today*, 16:435–455, 2019.

[19] Jens Kunstmann, Fabian Mooshammer, Philipp Nagler, Andrey Chaves, Frederick Stein, Nicola Paradiso, Gerd Plechinger, Christoph Strunk, Christian Schüller, Gotthard Seifert, et al. Momentum-space indirect interlayer excitons in transition-metal dichalcogenide van der waals heterostructures. *Nature Physics*, 14(8):801–805, 2018.

[20] Chenhao Jin, Eric Yue Ma, Ouri Karni, Emma C Regan, Feng Wang, and Tony F Heinz. Ultrafast dynamics in van der waals heterostructures. *Nature nanotechnology*, 13(11):994–1003, 2018.

[21] Roland Gillen and Janina Maultzsch. Interlayer excitons in mose 2/wse 2 heterostructures from first principles. *Physical Review B*, 97(16):165306, 2018.

[22] Philipp Merkl, Fabian Mooshammer, Philipp Steinleitner, Anna Girnghuber, K-Q Lin, Philipp Nagler, Johannes Holler, Christian Schüller, John M Lupton, Tobias Korn, et al. Ultrafast transition between exciton phases in van der waals heterostructures. *Nature materials*, 18(7):691–696, 2019.

[23] Pasqual Rivera, Hongyi Yu, Kyle L Seyler, Nathan P Wilson, Wang Yao, and Xiaodong Xu. Interlayer valley excitons in heterobilayers of transition metal dichalcogenides. *Nature nanotechnology*, 13(11):1004–1015, 2018.

[24] Zefang Wang, Yi-Hsin Chiu, Kevin Honz, Kin Fai Mak, and Jie Shan. Electrical tuning of interlayer exciton gases in wse2 bilayers. *Nano letters*, 18(1):137–143, 2018.

[25] Namphung Peimyoo, Thorsten Deilmann, Freddie Withers, Janire Escolar, Darren Nutting, Takashi Taniguchi, Kenji Watanabe, Alireza

Taghizadeh, Monica Felicia Craciun, Kristian Sommer Thygesen, et al. Electrical tuning of optically active interlayer excitons in bilayer mos2. *Nature Nanotechnology*, 16(8):888–893, 2021.

[26] Evgeny M Alexeev, David A Ruiz-Tijerina, Mark Danovich, Matthew J Hamer, Daniel J Terry, Pramoda K Nayak, Seongjoon Ahn, Sangyeon Pak, Juwon Lee, Jung Inn Sohn, et al. Resonantly hybridized excitons in moiré superlattices in van der waals heterostructures. *Nature*, 567(7746):81–86, 2019.

[27] David A Ruiz-Tijerina and Vladimir I Fal'ko. Interlayer hybridization and moiré superlattice minibands for electrons and excitons in heterobilayers of transition-metal dichalcogenides. *Physical Review B*, 99(12):125424, 2019.

[28] Yong Wang, Zhan Wang, Wang Yao, Gui-Bin Liu, and Hongyi Yu. Interlayer coupling in commensurate and incommensurate bilayer structures of transition-metal dichalcogenides. *Physical Review B*, 95(11):115429, 2017.

[29] Yongji Gong, Junhao Lin, Xingli Wang, Gang Shi, Sidong Lei, Zhong Lin, Xiaolong Zou, Gonglan Ye, Robert Vajtai, Boris I Yakobson, et al. Vertical and in-plane heterostructures from ws 2/mos 2 monolayers. *Nature materials*, 13(12):1135–1142, 2014.

[30] Xidong Duan, Chen Wang, Jonathan C Shaw, Rui Cheng, Yu Chen, Honglai Li, Xueping Wu, Ying Tang, Qinling Zhang, Anlian Pan, et al. Lateral epitaxial growth of two-dimensional layered semiconductor heterojunctions. *Nature nanotechnology*, 9(12):1024–1030, 2014.

[31] Chunming Huang, Sanfeng Wu, Ana M Sanchez, Jonathan JP Peters, Richard Beanland, Jason S Ross, Pasqual Rivera, Wang Yao, David H Cobden, and Xiaodong Xu. Lateral heterojunctions within monolayer mose 2–wse 2 semiconductors. *Nature materials*, 13(12):1096–1101, 2014.

[32] Roberto Rosati, Ioannis Paradisanos, Libai Huang, Ziyang Gan, Antony George, Kenji Watanabe, Takashi Taniguchi, Laurent Lombez, Pierre Renucci, Andrey Turchanin, et al. Interface engineering of

charge-transfer excitons in 2d lateral heterostructures. *Nature communications*, 14(1):2438, 2023.

[33] Dipesh B Trivedi, Guven Turgut, Ying Qin, Mohammed Y Sayyad, Debarati Hajra, Madeleine Howell, Lei Liu, Sijie Yang, Naim Hossain Patoary, Han Li, et al. Room-temperature synthesis of 2d janus crystals and their heterostructures. *Advanced materials*, 32(50):2006320, 2020.

[34] Yuan Cao, Valla Fatemi, Shiang Fang, Kenji Watanabe, Takashi Taniguchi, Efthimios Kaxiras, and Pablo Jarillo-Herrero. Unconventional superconductivity in magic-angle graphene superlattices. *Nature*, 556(7699):43–50, 2018.

[35] Kyle L Seyler, Pasqual Rivera, Hongyi Yu, Nathan P Wilson, Essance L Ray, David G Mandrus, Jiaqiang Yan, Wang Yao, and Xiaodong Xu. Signatures of moiré-trapped valley excitons in mose2/wse2 heterobilayers. *Nature*, 567(7746):66–70, 2019.

[36] Kha Tran, Galan Moody, Fengcheng Wu, Xiaobo Lu, Junho Choi, Kyounghwan Kim, Amritesh Rai, Daniel A Sanchez, Jiamin Quan, Akshay Singh, et al. Evidence for moiré excitons in van der waals heterostructures. *Nature*, 567(7746):71–75, 2019.

[37] Hongyi Yu, Gui-Bin Liu, Jianju Tang, Xiaodong Xu, and Wang Yao. Moiré excitons: From programmable quantum emitter arrays to spin-orbit–coupled artificial lattices. *Science advances*, 3(11):e1701696, 2017.

[38] Junho Choi, Matthias Florian, Alexander Steinhoff, Daniel Erben, Kha Tran, Dong Seob Kim, Liuyang Sun, Jiamin Quan, Robert Claassen, Somak Majumder, et al. Twist angle-dependent interlayer exciton lifetimes in van der waals heterostructures. *Physical Review Letters*, 126(4):047401, 2021.

[39] Philipp Merkl, Fabian Mooshammer, Samuel Brem, Anna Girnghuber, Kai-Qiang Lin, Leonard Weigl, Marlene Liebich, Chaw-Keong Yong, Roland Gillen, Janina Maultzsch, et al. Twist-tailoring coulomb correlations in van der waals homobilayers. *Nature communications*, 11(1):1–7, 2020.

[40] David Schmitt, Jan Philipp Bange, Wiebke Bennecke, AbdulAziz Al-Mutairi, Giuseppe Meneghini, Kenji Watanabe, Takashi Taniguchi, Daniel Steil, D Russell Luke, R Thomas Weitz, et al. Formation of moiré interlayer excitons in space and time. *Nature*, 608(7923):499–503, 2022.

[41] Di Huang, Junho Choi, Chih-Kang Shih, and Xiaoqin Li. Excitons in semiconductor moiré superlattices. *Nature Nanotechnology*, 17(3):227–238, 2022.

[42] Samuel Brem, Christopher Linderälv, Paul Erhart, and Ermin Malic. Tunable phases of moiré excitons in van der waals heterostructures. *Nano Letters*, 20(12):8534–8540, 2020. PMID: 32970445.

[43] Samuel Brem, Kai-Qiang Lin, Roland Gillen, Jonas M. Bauer, Janina Maultzsch, John M. Lupton, and Ermin Malic. Hybridized intervalley moiré excitons and flat bands in twisted wse2 bilayers. *Nanoscale*, 12:11088–11094, 2020.

[44] Joakim Hagel. *Moiré Exciton Landscape and its Optical Properties in Two-Dimensional Semiconductors*. Chalmers Tekniska Hogskola (Sweden), 2022.

[45] Wolfgang Nolting and William D. Brewer. *Fundamentals of Many-body Physics*. Springer Berlin, Heidelberg, 2009.

[46] M Lindberg and Stephan W Koch. Effective bloch equations for semiconductors. *Physical Review B*, 38(5):3342, 1988.

[47] Phaedon Avouris, Tony F. Heinz, and Tony Low, editors. *2D Materials: Properties and Devices*. Cambridge University Press, 2017.

[48] Andor Kormányos, Guido Burkard, Martin Gmitra, Jaroslav Fabian, Viktor Zólyomi, Neil D Drummond, and Vladimir Fal'ko. k· p theory for two-dimensional transition metal dichalcogenide semiconductors. *2D Materials*, 2(2):022001, 2015.

[49] Xiaodong Li, Jeffrey T Mullen, Zhenghe Jin, Kostyantyn M Borysenko, M Buongiorno Nardelli, and Ki Wook Kim. Intrinsic electrical transport properties of monolayer silicene and mos 2 from first principles. *Physical Review B*, 87(11):115418, 2013.

[50] Mackillo Kira and Stephan W. Koch. *Semiconductor Quantum Optics.* Cambridge University Press, 2011.

[51] Natalia S Rytova. Screened potential of a point charge in a thin film. *Moscow University Physics Bulletin*, 3(30), 1967.

[52] LV Keldysh. Coulomb interaction in thin semiconductor and semimetal films. *Soviet Journal of Experimental and Theoretical Physics Letters*, 29:658, 1979.

[53] Samuel Brem, Jonas Zipfel, Malte Selig, Archana Raja, Lutz Waldecker, Jonas D Ziegler, Takashi Taniguchi, Kenji Watanabe, Alexey Chernikov, and Ermin Malic. Intrinsic lifetime of higher excitonic states in tungsten diselenide monolayers. *Nanoscale*, 11(25):12381–12387, 2019.

[54] Zhenghe Jin, Xiaodong Li, Jeffrey T Mullen, and Ki Wook Kim. Intrinsic transport properties of electrons and holes in monolayer transition-metal dichalcogenides. *Physical Review B*, 90(4):045422, 2014.

[55] Jamie M Fitzgerald, Joshua JP Thompson, and Ermin Malic. Twist angle tuning of moiré exciton polaritons in van der waals heterostructures. *Nano Letters*, 2022.

[56] Beatriz Ferreira, Roberto Rosati, and Ermin Malic. Microscopic modeling of exciton-polariton diffusion coefficients in atomically thin semiconductors. *Physical Review Materials*, 6(3):034008, 2022.

[57] Jonas K König, Jamie M Fitzgerald, Joakim Hagel, Daniel Erkensten, and Ermin Malic. Interlayer exciton polaritons in homobilayers of transition metal dichalcogenides. *2D Materials*, 10(2):025019, 2023.

[58] Raul Perea-Causin, Samuel Brem, Roberto Rosati, Roland Jago, Marvin Kulig, Jonas D Ziegler, Jonas Zipfel, Alexey Chernikov, and Ermin Malic. Exciton propagation and halo formation in two-dimensional materials. *Nano letters*, 19(10):7317–7323, 2019.

[59] Roberto Rosati, Robert Schmidt, Samuel Brem, Raül Perea-Causín, Iris Niehues, Johannes Kern, Johann A Preuß, Robert Schneider, Steffen Michaelis de Vasconcellos, Rudolf Bratschitsch, et al. Dark exciton

anti-funneling in atomically thin semiconductors. *Nature Communications*, 12(1):1–7, 2021.

[60] Koloman Wagner, Jonas Zipfel, Roberto Rosati, Edith Wietek, Jonas D. Ziegler, Samuel Brem, Raül Perea-Causín, Takashi Taniguchi, Kenji Watanabe, Mikhail M. Glazov, Ermin Malic, and Alexey Chernikov. Nonclassical exciton diffusion in monolayer wse$_2$. *Phys. Rev. Lett.*, 127:076801, Aug 2021.

[61] Guang Yi Jia, Yue Liu, Jing Yu Gong, Dang Yuan Lei, Dan Li Wang, and Zhen Xian Huang. Excitonic quantum confinement modified optical conductivity of monolayer and few-layered mos 2. *Journal of Materials Chemistry C*, 4(37):8822–8828, 2016.

[62] Ermin Malic, Malte Selig, Maja Feierabend, Samuel Brem, Dominik Christiansen, Florian Wendler, Andreas Knorr, and Gunnar Berghäuser. Dark excitons in transition metal dichalcogenides. *Physical Review Materials*, 2(1):014002, 2018.

[63] Gunnar Berghäuser, Philipp Steinleitner, Philipp Merkl, Rupert Huber, Andreas Knorr, and Ermin Malic. Mapping of the dark exciton landscape in transition metal dichalcogenides. *Physical Review B*, 98(2):020301, 2018.

[64] Robert Wallauer, Raul Perea-Causin, Lasse Münster, Sarah Zajusch, Samuel Brem, Jens Güdde, Katsumi Tanimura, Kai-Qiang Lin, Rubert Huber, Ermin Malic, et al. Momentum-resolved observation of exciton formation dynamics in monolayer ws2. *Nano Letters*, 21(13):5867–5873, 2021.

[65] Florian Katsch, Malte Selig, Alexander Carmele, and Andreas Knorr. Theory of exciton–exciton interactions in monolayer transition metal dichalcogenides. *physica status solidi (b)*, 255(12):1800185, 2018.

[66] M Kira and SW Koch. Many-body correlations and excitonic effects in semiconductor spectroscopy. *Progress in Quantum Electronics*, 30(5):155–296, 2006.

[67] Gunnar Berghäuser, Philipp Steinleitner, Philipp Merkl, Rupert Huber, Andreas Knorr, and Ermin Malic. Mapping of the dark exciton

landscape in transition metal dichalcogenides. *Phys. Rev. B*, 98:020301, Jul 2018.

[68] Samuel Brem, August Ekman, Dominik Christiansen, Florian Katsch, Malte Selig, Cedric Robert, Xavier Marie, Bernhard Urbaszek, Andreas Knorr, and Ermin Malic. Phonon-assisted photoluminescence from indirect excitons in monolayers of transition-metal dichalcogenides. *Nano Letters*, 20(4):2849–2856, 2020. PMID: 32084315.

[69] Malte Selig, Gunnar Berghäuser, Archana Raja, Philipp Nagler, Christian Schüller, Tony F Heinz, Tobias Korn, Alexey Chernikov, Ermin Malic, and Andreas Knorr. Excitonic linewidth and coherence lifetime in monolayer transition metal dichalcogenides. *Nature communications*, 7(1):1–6, 2016.

[70] Mashael M Altaiary, Erfu Liu, Ching-Tarng Liang, Fu-Chen Hsiao, Jeremiah van Baren, Takashi Taniguchi, Kenji Watanabe, Nathaniel M Gabor, Yia-Chung Chang, and Chun Hung Lui. Electrically switchable intervalley excitons with strong two-phonon scattering in bilayer wse2. *Nano Letters*, 22(5):1829–1835, 2022.

[71] Zhiheng Huang, Yanchong Zhao, Tao Bo, Yanbang Chu, Jinpeng Tian, Le Liu, Yalong Yuan, Fanfan Wu, Jiaojiao Zhao, Lede Xian, et al. Spatially indirect intervalley excitons in bilayer w se 2. *Physical Review B*, 105(4):L041409, 2022.

[72] Bastian Miller, Alexander Steinhoff, Borja Pano, Julian Klein, Frank Jahnke, Alexander Holleitner, and Ursula Wurstbauer. Long-lived direct and indirect interlayer excitons in van der waals heterostructures. *Nano letters*, 17(9):5229–5237, 2017.

[73] Joakim Hagel, Samuel Brem, Christopher Linderälv, Paul Erhart, and Ermin Malic. Exciton landscape in van der waals heterostructures. *Phys. Rev. Research*, 3:043217, Dec 2021.

[74] Fedele Tagarelli, Edoardo Lopriore, Daniel Erkensten, Raül Perea-Causín, Samuel Brem, Joakim Hagel, Zhe Sun, Gabriele Pasquale, Kenji Watanabe, Takashi Taniguchi, Ermin Malic, and Andras Kis. Electrical control of hybrid exciton transport in a van der waals heterostructure. *Nature Photonics*, 17(7):615–621, Jul 2023.

[75] Daniel Erkensten, Samuel Brem, Raül Perea-Causín, and Ermin Malic. Microscopic origin of anomalous interlayer exciton transport in van der waals heterostructures. *Physical Review Materials*, 6(9):094006, 2022.

[76] Simon Ovesen, Samuel Brem, Christopher Linderälv, Mikael Kuisma, Tobias Korn, Paul Erhart, Malte Selig, and Ermin Malic. Interlayer exciton dynamics in van der waals heterostructures. *Communications Physics*, 2(1):1–8, 2019.

[77] Akash Laturia, Maarten L Van de Put, and William G Vandenberghe. Dielectric properties of hexagonal boron nitride and transition metal dichalcogenides: from monolayer to bulk. *npj 2D Materials and Applications*, 2(1):1–7, 2018.

[78] R. Geick, C. H. Perry, and G. Rupprecht. Normal modes in hexagonal boron nitride. *Phys. Rev.*, 146:543–547, Jun 1966.

[79] Qingjun Tong, Mingxing Chen, Feiping Xiao, Hongyi Yu, and Wang Yao. Interferences of electrostatic moiré potentials and bichromatic superlattices of electrons and excitons in transition metal dichalcogenides. *2D Materials*, 8(2):025007, 2020.

[80] VV Enaldiev, Viktor Zólyomi, CELAL Yelgel, SJ Magorrian, and VI Fal'ko. Stacking domains and dislocation networks in marginally twisted bilayers of transition metal dichalcogenides. *Physical Review Letters*, 124(20):206101, 2020.

[81] Iann C Gerber, Emmanuel Courtade, Shivangi Shree, Cedric Robert, Takashi Taniguchi, Kenji Watanabe, Andrea Balocchi, Pierre Renucci, Delphine Lagarde, Xavier Marie, et al. Interlayer excitons in bilayer mos 2 with strong oscillator strength up to room temperature. *Physical Review B*, 99(3):035443, 2019.

[82] David A. Ruiz-Tijerina and Vladimir I. Fal'ko. Interlayer hybridization and moiré superlattice minibands for electrons and excitons in hetero-bilayers of transition-metal dichalcogenides. *Phys. Rev. B*, 99:125424, Mar 2019.

[83] E Cappelluti, Rafael Roldán, JA Silva-Guillén, Pablo Ordejón, and F Guinea. Tight-binding model and direct-gap/indirect-gap transition

in single-layer and multilayer mos 2. *Physical Review B*, 88(7):075409, 2013.

[84] Astrid Weston, Yichao Zou, Vladimir Enaldiev, Alex Summerfield, Nicholas Clark, Viktor Zólyomi, Abigail Graham, Celal Yelgel, Samuel Magorrian, Mingwei Zhou, et al. Atomic reconstruction in twisted bilayers of transition metal dichalcogenides. *Nature Nanotechnology*, 15(7):592–597, 2020.

[85] Matthew R Rosenberger, Hsun-Jen Chuang, Madeleine Phillips, Vladimir P Oleshko, Kathleen M McCreary, Saujan V Sivaram, C Stephen Hellberg, and Berend T Jonker. Twist angle-dependent atomic reconstruction and moiré patterns in transition metal dichalcogenide heterostructures. *ACS nano*, 14(4):4550–4558, 2020.

[86] Madeline Van Winkle, Isaac M Craig, Stephen Carr, Medha Dandu, Karen C Bustillo, Jim Ciston, Colin Ophus, Takashi Taniguchi, Kenji Watanabe, Archana Raja, et al. Rotational and dilational reconstruction in transition metal dichalcogenide moiré bilayers. *Nature Communications*, 14(1):2989, 2023.

[87] Mit H Naik, Emma C Regan, Zuocheng Zhang, Yang-Hao Chan, Zhenglu Li, Danqing Wang, Yoseob Yoon, Chin Shen Ong, Wenyu Zhao, Sihan Zhao, et al. Intralayer charge-transfer moiré excitons in van der waals superlattices. *Nature*, 609(7925):52–57, 2022.

[88] Hongyuan Li, Shaowei Li, Mit H Naik, Jingxu Xie, Xinyu Li, Jiayin Wang, Emma Regan, Danqing Wang, Wenyu Zhao, Sihan Zhao, et al. Imaging moiré flat bands in three-dimensional reconstructed wse2/ws2 superlattices. *Nature materials*, 20(7):945–950, 2021.

[89] Chendong Zhang, Chih-Piao Chuu, Xibiao Ren, Ming-Yang Li, Lain-Jong Li, Chuanhong Jin, Mei-Yin Chou, and Chih-Kang Shih. Interlayer couplings, moiré patterns, and 2d electronic superlattices in mos2/wse2 hetero-bilayers. *Science advances*, 3(1):e1601459, 2017.

[90] Shen Zhao, Zhijie Li, Xin Huang, Anna Rupp, Jonas Göser, Ilia A. Vovk, Stanislav Yu. Kruchinin, Kenji Watanabe, Takashi Taniguchi, Ismail Bilgin, Anvar S. Baimuratov, and Alexander Högele. Excitons

in mesoscopically reconstructed moiré heterostructures. *Nature Nanotechnology*, 18(6):572–579, Jun 2023.

[91] Zhijie Li, Farsane Tabataba-Vakili, Shen Zhao, Anna Rupp, Ismail Bilgin, Ziria Herdegen, Benjamin März, Kenji Watanabe, Takashi Taniguchi, Gabriel Ravanhani Schleder, Anvar S. Baimuratov, Efthimios Kaxiras, Knut Müller-Caspary, and Alexander Högele. Lattice reconstruction in mose2–wse2 heterobilayers synthesized by chemical vapor deposition. *Nano Letters*, 23(10):4160–4166, May 2023.

[92] Jiho Sung, You Zhou, Giovanni Scuri, Viktor Zólyomi, Trond I Andersen, Hyobin Yoo, Dominik S Wild, Andrew Y Joe, Ryan J Gelly, Hoseok Heo, et al. Broken mirror symmetry in excitonic response of reconstructed domains in twisted mose 2/mose 2 bilayers. *Nature Nanotechnology*, 15(9):750–754, 2020.

[93] Stephen Carr, Daniel Massatt, Steven B Torrisi, Paul Cazeaux, Mitchell Luskin, and Efthimios Kaxiras. Relaxation and domain formation in incommensurate two-dimensional heterostructures. *Physical Review B*, 98(22):224102, 2018.

[94] Willy Knorr, Samuel Brem, Giuseppe Meneghini, and Ermin Malic. Exciton transport in a moiré potential: From hopping to dispersive regime. *Phys. Rev. Mater.*, 6:124002, Dec 2022.

[95] Lev Davidovich Landau, Evgenii Mikhailovich Lifshitz, Arnoĺd Markovich Kosevich, and Lev Petrovich Pitaevskii. *Theory of elasticity: volume 7*, volume 7. Elsevier, 1986.

[96] Fábio Ferreira, SJ Magorrian, VV Enaldiev, DA Ruiz-Tijerina, and VI Fal'ko. Band energy landscapes in twisted homobilayers of transition metal dichalcogenides. *Applied Physics Letters*, 118(24):241602, 2021.

[97] Logan D. R. Beal, Daniel C. Hill, R. Abraham Martin, and John D. Hedengren. Gekko optimization suite. *Processes*, 6(8), 2018.

[98] Bruno Amorim, Alberto Cortijo, F De Juan, Adolfo G Grushin, Francisco Guinea, A Gutiérrez-Rubio, Hector Ochoa, Vincenzo Parente, Rafael Roldán, Pablo San-Jose, et al. Novel effects of strains in graphene and other two dimensional materials. *Physics Reports*, 617:1–54, 2016.

[99] MA Cazalilla, Héctor Ochoa, and F Guinea. Quantum spin hall effect in two-dimensional crystals of transition-metal dichalcogenides. *Physical review letters*, 113(7):077201, 2014.

[100] Shiang Fang, Stephen Carr, Miguel A Cazalilla, and Efthimios Kaxiras. Electronic structure theory of strained two-dimensional materials with hexagonal symmetry. *Physical Review B*, 98(7):075106, 2018.

[101] Habib Rostami, Rafael Roldán, Emmanuele Cappelluti, Reza Asgari, and Francisco Guinea. Theory of strain in single-layer transition metal dichalcogenides. *Physical Review B*, 92(19):195402, 2015.

[102] V V Enaldiev, F Ferreira, S J Magorrian, and Vladimir I Fal'ko. Piezoelectric networks and ferroelectric domains in twistronic superlattices in ws2/mos2 and wse2/mose2 bilayers. *2D Materials*, 8(2):025030, feb 2021.

[103] Zahra Khatibi, Maja Feierabend, Malte Selig, Samuel Brem, Christopher Linderälv, Paul Erhart, and Ermin Malic. Impact of strain on the excitonic linewidth in transition metal dichalcogenides. *2D Materials*, 6(1):015015, 2018.

[104] Fabio Bernardini, Vincenzo Fiorentini, and David Vanderbilt. Spontaneous polarization and piezoelectric constants of iii-v nitrides. *Physical Review B*, 56(16):R10024, 1997.

[105] Karel-Alexander N Duerloo, Mitchell T Ong, and Evan J Reed. Intrinsic piezoelectricity in two-dimensional materials. *The Journal of Physical Chemistry Letters*, 3(19):2871–2876, 2012.

[106] Habib Rostami, Francisco Guinea, Marco Polini, and Rafael Roldán. Piezoelectricity and valley chern number in inhomogeneous hexagonal 2d crystals. *npj 2D Materials and Applications*, 2(1):15, 2018.

[107] Hongyi Yu, Gui-Bin Liu, Pu Gong, Xiaodong Xu, and Wang Yao. Dirac cones and dirac saddle points of bright excitons in monolayer transition metal dichalcogenides. *Nature communications*, 5(1):3876, 2014.

[108] Daniel Erkensten, Samuel Brem, and Ermin Malic. Exciton-exciton interaction in transition metal dichalcogenide monolayers and van der waals heterostructures. *Physical Review B*, 103(4):045426, 2021.

[109] Daniel Erkensten, Samuel Brem, Koloman Wagner, Roland Gillen, Raül Perea-Causín, Jonas D Ziegler, Takashi Taniguchi, Kenji Watanabe, Janina Maultzsch, Alexey Chernikov, et al. Dark exciton-exciton annihilation in monolayer wse 2. *Physical Review B*, 104(24):L241406, 2021.

[110] Daniel Erkensten, Samuel Brem, Raül Perea-Causín, Joakim Hagel, Fedele Tagarelli, Edoardo Lopriore, Andras Kis, and Ermin Malic. Electrically tunable dipolar interactions between layer-hybridized excitons. *Nanoscale*, 15(26):11064–11071, 2023.

[111] Hong EnáLim et al. Restoring the intrinsic optical properties of cvd-grown mos 2 monolayers and their heterostructures. *Nanoscale*, 11(27):12798–12803, 2019.

[112] Nadine Leisgang, Shivangi Shree, Ioannis Paradisanos, Lukas Sponfeldner, Cedric Robert, Delphine Lagarde, Andrea Balocchi, Kenji Watanabe, Takashi Taniguchi, Xavier Marie, et al. Giant stark splitting of an exciton in bilayer mos2. *Nature Nanotechnology*, 15(11):901–907, 2020.

[113] Yuanda Liu, Kévin Dini, Qinghai Tan, Timothy Liew, Kostya S Novoselov, and Weibo Gao. Electrically controllable router of interlayer excitons. *Science advances*, 6(41):eaba1830, 2020.

[114] Florian M Arnold, Alireza Ghasemifard, Agnieszka Kuc, Jens Kunstmann, and Thomas Heine. Relaxation effects in twisted bilayer molybdenum disulfide: structure, stability, and electronic properties. *2D Materials*, 10(4):045010, 2023.

[115] Christopher Linderälv, Joakim Hagel, Samuel Brem, Ermin Malic, and Paul Erhart. The moiré potential in twisted transition metal dichalcogenide bilayers. *arXiv preprint arXiv:2205.15616*, 2022.

[116] Nikodem Sokolowski, Swaroop Palai, Mateusz Dyksik, Katarzyna Posmyk, Michał Baranowski, Alessandro Surrente, Duncan Maude, Felix Carrascoso, Onur Cakiroglu, Estrella Sanchez, et al. Twist-angle dependent dehybridization of momentum-indirect excitons in mose2/mos2 heterostructures. *2D Materials*, 10(3):034003, 2023.

[117] Xiangying Su, Weiwei Ju, Ruizhi Zhang, Chongfeng Guo, Jiming Zheng, Yongliang Yong, and Xiaohong Li. Bandgap engineering of

mos$_2$/mx$_2$ (mx$_2$= ws$_2$, mose$_2$ and wse$_2$) heterobilayers subjected to biaxial strain and normal compressive strain. *Rsc Advances*, 6(22):18319–18325, 2016.

[118] Joakim Hagel, Samuel Brem, Johannes Abelardo Pineiro, and Ermin Malic. Impact of atomic reconstruction on optical spectra of twisted tmd homobilayers. *Phys. Rev. Mater.*, 8:034001, Mar 2024.

[119] Maja Feierabend, Alexandre Morlet, Gunnar Berghäuser, and Ermin Malic. Impact of strain on the optical fingerprint of monolayer transition-metal dichalcogenides. *Phys. Rev. B*, 96:045425, Jul 2017.

[120] Hongyuan Li, Ziyu Xiang, Mit H Naik, Woochang Kim, Zhenglu Li, Renee Sailus, Rounak Banerjee, Takashi Taniguchi, Kenji Watanabe, Sefaattin Tongay, et al. Imaging moiré excited states with photocurrent tunnelling microscopy. *Nature materials*, pages 1–6, 2024.

[121] Niclas Götting, Frederik Lohof, and Christopher Gies. Moiré-bose-hubbard model for interlayer excitons in twisted transition metal dichalcogenide heterostructures. *Phys. Rev. B*, 105:165419, Apr 2022.

[122] Conrad Sanderson and Ryan Curtin. Practical sparse matrices in c++ with hybrid storage and template-based expression optimisation. *Mathematical and Computational Applications*, 24(3):70, 2019.

[123] Conrad Sanderson and Ryan Curtin. Armadillo: a template-based c++ library for linear algebra. *Journal of Open Source Software*, 1(2):26, 2016.

[124] Junhui Weng and Shang-Peng Gao. A honeycomb-like monolayer of hfo 2 and the calculation of static dielectric constant eliminating the effect of vacuum spacing. *Physical Chemistry Chemical Physics*, 20(41):26453–26462, 2018.

[125] Yanhao Tang, Jie Gu, Song Liu, Kenji Watanabe, Takashi Taniguchi, James C Hone, Kin Fai Mak, and Jie Shan. Dielectric catastrophe at the wigner-mott transition in a moiré superlattice. *Nature communications*, 13(1):4271, 2022.

[126] Samuel Brem and Ermin Malic. Bosonic delocalization of dipolar moiré excitons. *Nano Letters*, 23(10):4627–4633, 2023.

[127] Long Yuan, Biyuan Zheng, Jens Kunstmann, Thomas Brumme, Agnieszka Beata Kuc, Chao Ma, Shibin Deng, Daria Blach, Anlian Pan, and Libai Huang. Twist-angle-dependent interlayer exciton diffusion in ws2–wse2 heterobilayers. *Nature materials*, 19(6):617–623, 2020.

[128] Qianhui Shi, En-Min Shih, Daniel Rhodes, Bumho Kim, Katayun Barmak, Kenji Watanabe, Takashi Taniguchi, Zlatko Papić, Dmitry A Abanin, James Hone, et al. Bilayer wse2 as a natural platform for interlayer exciton condensates in the strong coupling limit. *Nature nanotechnology*, 17(6):577–582, 2022.

[129] Jung-Jung Su and AH MacDonald. How to make a bilayer exciton condensate flow. *Nature Physics*, 4(10):799–802, 2008.

[130] A Shubnic, V Shahnazaryan, IA Shelykh, and H Rostami. Exciton spin hall effect in arc-shaped strained wse 2. *Physical Review B*, 109(20):L201409, 2024.

[131] AK Geim. Energy gaps and a zero-field quantum hall effect in graphene by strain engineering. *Nature Physics*, 6(1):30–33, 2010.

[132] Jiamin Quan, Lukas Linhart, Miao-Ling Lin, Daehun Lee, Jihang Zhu, Chun-Yuan Wang, Wei-Ting Hsu, Junho Choi, Jacob Embley, Carter Young, et al. Phonon renormalization in reconstructed mos2 moiré superlattices. *Nature materials*, 20(8):1100–1105, 2021.

[133] Héctor Ochoa. Moiré-pattern fluctuations and electron-phason coupling in twisted bilayer graphene. *Physical Review B*, 100(15):155426, 2019.

[134] Antonio Rossi, Jonas Zipfel, Indrajit Maity, Monica Lorenzon, Luca Francaviglia, Emma C Regan, Zuocheng Zhang, Jacob H Nie, Edward Barnard, Kenji Watanabe, et al. Phason-mediated interlayer exciton diffusion in ws2/wse2 moir\'e heterostructure. *arXiv preprint arXiv:2301.07750*, 2023.

[135] Indrajit Maity, Arash A Mostofi, and Johannes Lischner. Electrons surf phason waves in moiré bilayers. *Nano Letters*, 23(11):4870–4875, 2023.

[136] Giuseppe Meneghini, Samuel Brem, and Ermin Malic. Ultrafast phonon-driven charge transfer in van der waals heterostructures. *Natural Sciences*, page e20220014, 2022.

[137] Giuseppe Meneghini, Samuel Brem, and Ermin Malic. Excitonic thermalization bottleneck in twisted tmd heterostructures. *Nano Letters*, 24(15):4505–4511, 2024.

[138] Giuseppe Meneghini, Marcel Reutzel, Stefan Mathias, Samuel Brem, and Ermin Malic. Hybrid exciton signatures in arpes spectra of van der waals materials. *ACS Photonics*, 10(10):3570–3575, 2023.

[139] Samuel Brem, Malte Selig, Gunnar Berghaeuser, and Ermin Malic. Exciton relaxation cascade in two-dimensional transition metal dichalcogenides. *Scientific reports*, 8(1):1–8, 2018.

[140] Yang Xu, Song Liu, Daniel A Rhodes, Kenji Watanabe, Takashi Taniguchi, James Hone, Veit Elser, Kin Fai Mak, and Jie Shan. Correlated insulating states at fractional fillings of moiré superlattices. *Nature*, 587(7833):214–218, 2020.

[141] Samuel Brem and Ermin Malic. Terahertz fingerprint of monolayer wigner crystals. *Nano letters*, 22(3):1311–1315, 2022.